Check for updates

Comprehensive Understandings into Complete Reconstruction of Precatalysts: Synthesis, Applications, and Characterizations

Xiong Liu, Jiashen Meng, Jiexin Zhu, Meng Huang, Bo Wen, Ruiting Guo, and Liqiang Mai*

Reconstruction induced by external environment (such as applied voltage bias and test electrolytes) changes catalyst component and catalytic behaviors. Investigations of complete reconstruction in energy conversion recently receive intensive attention, which promote the targeted design of top-performance materials with maximum component utilization and good stability. However, the advantages of complete reconstruction, its design strategies, and extensive applications have not achieved the profound understandings and summaries it deserves. Here, this review systematically summarizes several important advances in complete reconstruction for the first time, which includes 1) fundamental understandings of complete reconstruction, the characteristics and advantages of completely reconstructed catalysts, and their design principles, 2) types of reconstruction-involved precatalysts for oxygen evolution reaction catalysis in wide pH solution, and origins of limited reconstruction degree as well as design strategies/principles toward complete reconstruction, 3) complete reconstruction for novel material synthesis and other electrocatalysis fields, and 4) advanced in situ/operando or multiangle/level characterization techniques to capture the dynamic reconstruction processes and real catalytic contributors. Finally, the existing major challenges and unexplored/unsolved issues on studying the reconstruction chemistry are summarized, and an outlook for the further development of complete reconstruction is briefly proposed. This review will arouse the attention on complete reconstruction materials and their applications in diverse fields.

1. Introduction

Oxygen evolution reaction (OER) is a fundamental and important rate determining half-reaction in photo-/electrocatalytic water splitting, metal air batteries and other new types of prospective energy storage and conversion devices.[1,2] Traditional OER electrocatalysts are mainly granular catalysts such as

X. Liu, Dr. J. Meng, J. Zhu, M. Huang, B. Wen, R. Guo, Prof. L. Mai
State Key Laboratory of Advanced Technology for Materials Synthesis and Processing
Wuhan University of Technology
Wuhan 430070, China
E-mail: mlq518@whut.edu.cn
Prof. L. Mai
Foshan Xianhu Laboratory of the Advanced Energy Science and Technology Guangdong Laboratory
Xianhu Hydrogen Valley
Foshan 528200, China

The ORCID identification number(s) for the author(s) of this article can be found under https://doi.org/10.1002/adma.202007344.

precious metal Ru/Ir supported on carbon materials. Its poor stability in anodic reaction and high cost greatly limit their large-scale applications.[3] Therefore, developing low-cost OER catalyst with high-activity and superior durability properties is a key factor to achieve top-performance energy storage and conversion devices. In practical industrial application, the electric energy produced by solar, tidal and wind energy can be converted to hydrogen and oxygen by relatively mature alkaline water electrolysis (AWE) technology.[4] The produced hydrogen has the characteristics of high purity and no pollution of combustion products, and its high calorific value is 3 times that of gasoline.[2,5] Therefore, it is alternative to fossil fuels and can be used in fuel cell transportation system, high precision instrument welding, etc. Nevertheless, the current practical AWE system mainly focuses on using expensive and high-activity but poor-stability Ir/Ru/Pt catalysts, or the economic practical but low-activity nickel/stainless steel mesh.[6] The coupled systems display the energy conversion efficiency of electrolytic water to hydrogen within 50–70% for a long time, which is one of the key factors to cause high cost of water electrolysis technology. Based on extensive empirical researches, the nonprecious metal (Fe/Co/Ni)-based anode//NiMo-based hydrogen evolution reaction (HER) cathode are expected to become important new-type electrode components in future AWE system. Currently, NiMo-based catalysts can achieve Pt-like catalytic activity (10–30 mV overpotential at 10 mA cm^{-2}) and better stability (at least 100 h) than that of commercial Pt/C catalyst.[7,8] Due to the complicated catalyst reactions, Fe/Co/Ni-based OER catalysts generally display high overpotentials (at least 250 mV at 10 mA cm^{-2}),[9,10] restricting the development of the whole AWE system. Hence, how to achieve low-overpotential and high-stability OER anode is a significant scientific problem to promote the overall efficiency of water electrolysis system.

Recently, Fe/Co/Ni-based materials (such as chalcogenides, pnictides, perovskites, bimetallic hydroxides) are considered to have the greatest potential to match or even surpass the OER catalytic performance of benchmark Ru/Ir-based catalysts.[11] Understanding intrinsic catalytic mechanism and revealing real active sites are beneficial to the targeted design and application of high-efficiency nonprecious metal-based catalysts.

In the past, due to the limited development of in situ or operando characterization techniques, real-time monitoring of dynamic reconstruction and the capture of intermediates could not be effectively carried out. For example, CoO_2 can reverse to Co_3O_4 without applied high potentials, thus it is difficult to capture this high-valence Co species by ex situ characterization.[12] At this stage, with the great advances in characterization techniques,[13,14] such as in situ Raman, in situ X-ray absorption spectroscopy (XAS), in situ electron microscopy, and in situ ultraviolet visible (UV-vis), researchers have gained new insights into the intrinsic catalytic mechanisms. These catalysts generally undergo surface reconstruction under electro-oxidation conditions, in situ forming amorphous or low crystalline active catalytic species on the surface of the original catalyst. These species are usually the corresponding oxides or (oxy) hydroxides serving as real catalytic species, and the original catalysts should be called precatalysts.[15,16] Due to limited electrolyte diffusion and surface-catalyzed property, the evolved catalysts commonly show the core–shell structure with near surface reconstruction. Take a typical example, the core–shell $Ni_2P@NiO_x$ heterostructure formed after alkaline OER based on Ni_2P particle precatalyst.[17] For this kind of catalyst with partial phase reconstruction, it raises several challenges/issues. 1) It contains numerous inert internal components, resulting in low component utilization because the catalysis is a surface reaction process. 2) Its complex components would affect the recognition of real catalytic sites and the exploration of their catalytic mechanisms. 3) There are differences in reconstruction degree in reported catalysts, and the reason why some catalysts only have limited reconstruction degree is not clear. 4) Its reconstruction degree may be changed when the testing parameters change from conventional mild conditions to industrial extreme conditions, which means the variation of catalyst properties, such as structure, activity, stability, catalytic site, and selectivity. For these regards, the complete reconstruction of precatalysts is supposed to effectively avoid the above problems. On one hand, the complete reconstruction can realize the complete evolution of precatalyst components to catalytic species and thus maximize utilization with recognizable components and microstructures. On the other hand, it can also realize high catalysis durability even under extreme conditions such as high-temperature or high-concentrated solution in industrial AWE, because all instable components have been transformed into thermodynamically stable species during the complete reconstruction process. Therefore, engineering on complete reconstruction and its comprehensive understandings will direct purposeful design of high-performance catalysts and promote their industrialization. It should be noteworthy that a few reviews have been reported but mainly focus on surface reconstruction.[18–21] To the best of our knowledge, the summaries on complete reconstruction, especially its fundamental understandings, advantages and features of completely reconstructed catalysts, design principles/strategies, extensive electrocatalysis applications and establishment of reconstruction–performance correlation, as well as advanced characterizations, have not yet been reviewed comprehensively.

This review will spotlight the recent research progress on complete reconstruction (**Figure 1**), which is expected to become a new research point in the field of catalysis. First, fundamental
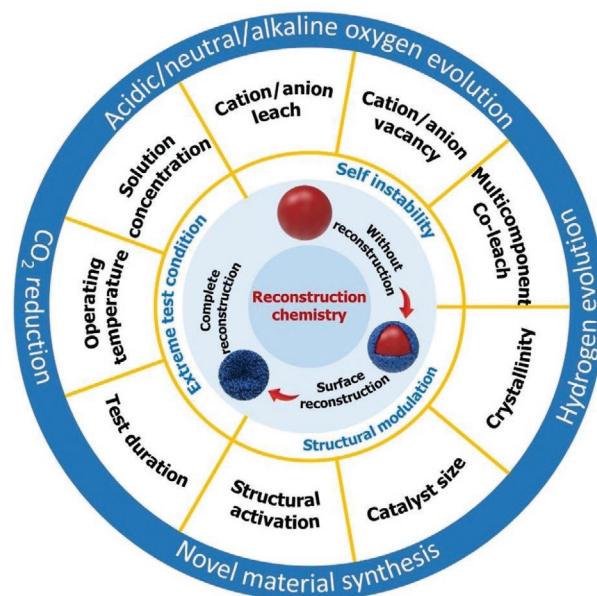

Figure 1. A summary of catalyst evolution results with different reconstruction degree, reconstruction engineering (i.e., self-instability, structural modulation, and extreme test conditions), and reconstruction-involved applications (i.e., OER, HER, CO_2 reduction, and novel material synthesis).

understandings of complete reconstruction, including reasons of reconstruction and classifications of reconstruction results, are discussed. The advantages and design principles of complete reconstruction are highlighted. Next, we detailedly outline the types of reconstruction-involved precatalysts in OER catalysis, summarize the origins of limited reconstruction and emphatically propose the strategies for complete reconstruction accordingly. Then, we introduce the relevant progress of complete reconstruction studies for novel material synthesis and applications in other catalytic reactions (e.g., hydrogen evolution reaction, CO_2 reduction). Besides, we summarize the employed in situ/operando or multiangle/level characterizations to achieve real-time detection of dynamic reconstruction and real catalytic species of reconstructed catalysts. Finally, opportunities and challenges for the future researches on reconstruction engineering and complete reconstruction catalysts are discussed and anticipated.

2. Complete reconstruction: Fundamental Understandings, Advantages, and Design Principles

2.1. Fundamental Understandings

2.1.1. Reasons of Reconstruction

Reconstruction of precatalysts will inevitably lead to changes in the intrinsic properties of materials (such as microstructures and electrical conductivity), and thus the changes in the energy barrier and kinetics of catalytic reactions. Therefore,

the study of the origin of reconstruction is crucial to the understanding of reconstruction chemistry. Researchers have discovered the reconstruction phenomena of catalysts extensively exist in OER, HER, CO_2 reduction, etc., promoting the scientific cognition of catalytic reconstruction. There are two main factors that induce the reconstruction of precatalysts, the applied voltage bias during catalysis and variable testing conditions. The former includes electrically driven surface oxidation/reduction of precatalysts caused by oxidized/reduced potentials.[19] During this molecular conversion catalysis, the required potentials for experimental operation on catalyst materials are generally more positive or negative than the equilibrium potentials. If the applied potential exceeds the redox potential of the element contained in materials, this will likely lead to the instability of precatalysts and the change of the valence state of surface atoms.[22] If such a process is irreversible when the potential comes back, this evolution would continue and finally a reconstruction layer composed of new species generates. For OER, the inevitable formation of oxygenic intermediates occurs on catalyst surface for most nonprecious metal materials. The surface sites operating catalysis reaction generally contain structural evolution towards reaction-preferred states. After reconstruction, the catalytic properties for the obtained catalysts have been changed, such as reaction sites, activity, selectivity, types of products, and amounts of catalytic sites. Actually, the stability property of reconstructed species will also drive the occurrence of reconstruction and affect the reconstruction results. From the view of thermodynamic stability, the corresponding oxides, hydroxides or (oxy)hydroxides are the most stable state under oxidation condition. For example, Guo et al. found the in situ self-reconstruction from Ag nanoparticles anchored on cobalt-iron hydr(oxy)oxide to Ag-intercalated cobalt-iron (oxy)hydroxide.[23] Such a reconstruction mechanism was theoretically uncovered that the aggregated Ag cluster on the cobalt-iron (oxy)hydroxide layer is less stable than the dispersed one, which might be the driving force for the homogenization of Ag. The latter mainly includes the temperature, pH, concentration of solution, pressure, etc. These parameters mainly modulate specific redox potentials and determine the component stability of precatalysts, as well as affect their reconstruction degree. The amount of newly generated species depends on the degree of reconstruction. Some reports have confirmed that the high concentration or temperature of solution could promote the reconstruction.[24,25] Therefore, the material properties and test conditions have a great influence on the reconstruction process and results.

2.1.2. Classifications of Reconstruction Results

According to the reconstruction degree of precatalysts, the reconstruction results are defined and divided into three categories including no reconstruction, surface reconstruction, and complete reconstruction (**Figure 2**a). Taking standard spherical particle precatalysts with a diameter of D as an example, its reconstruction degree is closely related to the thickness of reconstruction layer. If the thickness of reconstruction layer (T_{sr}) is less than D, the reconstruction process is called surface

reconstruction (SR), and the obtained catalysts are called surface reconstruction catalysts. If the body phase of precatalysts fully evolved into other species ($T_{cr} = D$), it is called complete reconstruction (CR). It is easy to distinguish between the surface reconstruction and complete reconstruction based on the presence or absence of original precatalyst. Besides, as summarized in our previous work,[25] many surface reconstruction catalysts show the limited reconstruction degree with the thickness of below 10 nm. Compared to the bulk materials with a few hundred nanometers in size, this reconstruction degree is very low. In this case, the reconstructed catalysts display a low degree of surface reconstruction, and the reconstruction thickness is denoted as T_{lsr} ($0 < T_{lsr} < 10$ nm). Recently, various strategies have been proposed and adopted to facilitate the reconstruction process; meanwhile, the catalysts with deepened reconstruction degree generally exhibit enhanced catalytic performance due to the more generation of active species, which is detailedly discussed in Section 3.4. There is a case that the reconstruction is deepened with high degree of surface reconstruction, but the original precatalysts still exist. For example, Hu et al. demonstrated that the introduction of fluoride (F^-) promoted the reconstruction of hydroxide, and observed a very high reconstruction layer (≈ 35 nm).[26] In this case, such a unique process is singled out for attention and we call deep reconstruction. The deep reconstruction still belongs to surface reconstruction, but displays high reconstruction degree ($T_{lsr} < T_{hsr} < D$). It should be noted that considering the complexity of the actual catalyst and its reconstruction degree, the proposed models only serve as a basic cognition to promote understanding of reconstruction.

Generally, cyclic voltammetry (CV) measurements are applied to achieve electrochemical activation and reconstruction.[25,27–30] Therefore, reconstruction-involved phenomenon in catalysis might be preliminarily evaluated and recognized by CV electrochemical measurements in advance. Three possible CV curves of nickel-based OER precatalysts are schematically displayed, containing observed redox peaks representing Ni^{3+}/Ni^{2+}. As shown in Figure 2b, the redox peak current gradually increased with the ongoing cyclic voltammetry test, meaning that more and more high-valence nickel species are produced via reconstruction. This phenomenon is similar to the other two cases in Figure 2c,d. Differently, in the first case, the current at high potentials where O_2 evolution is precipitated remains almost constant. However, it increases and decreases in the second and third cases, which are marked by the dotted yellow arrows in Figure 2c,d, respectively. The CV curves gradually overlap and achieve a stable level, suggesting the accomplished pretreatments which are generally called activation. There are some typical examples which support the above-mentioned phenomena. The first CV phenomenon is ideal, and generally the current at high potentials is variable. The typical example has been reported to exist in γ-NiOOH, and during 500-cycle CV, the redox peak current obviously increased but the current at high potentials almost not changed.[28] However, this result has not been explained. The CV activation curves for most catalysts are similar to the second case. For example, we recently discovered the complete reconstruction phenomenon of $NiMoO_4 \cdot xH_2O$ under alkaline OER condition, which could be achieved via initial 20-cycle CV measurement.[25] Both the intensity of the

**ADVANCED
SCIENCE NEWS**

www.advancedsciencenews.com
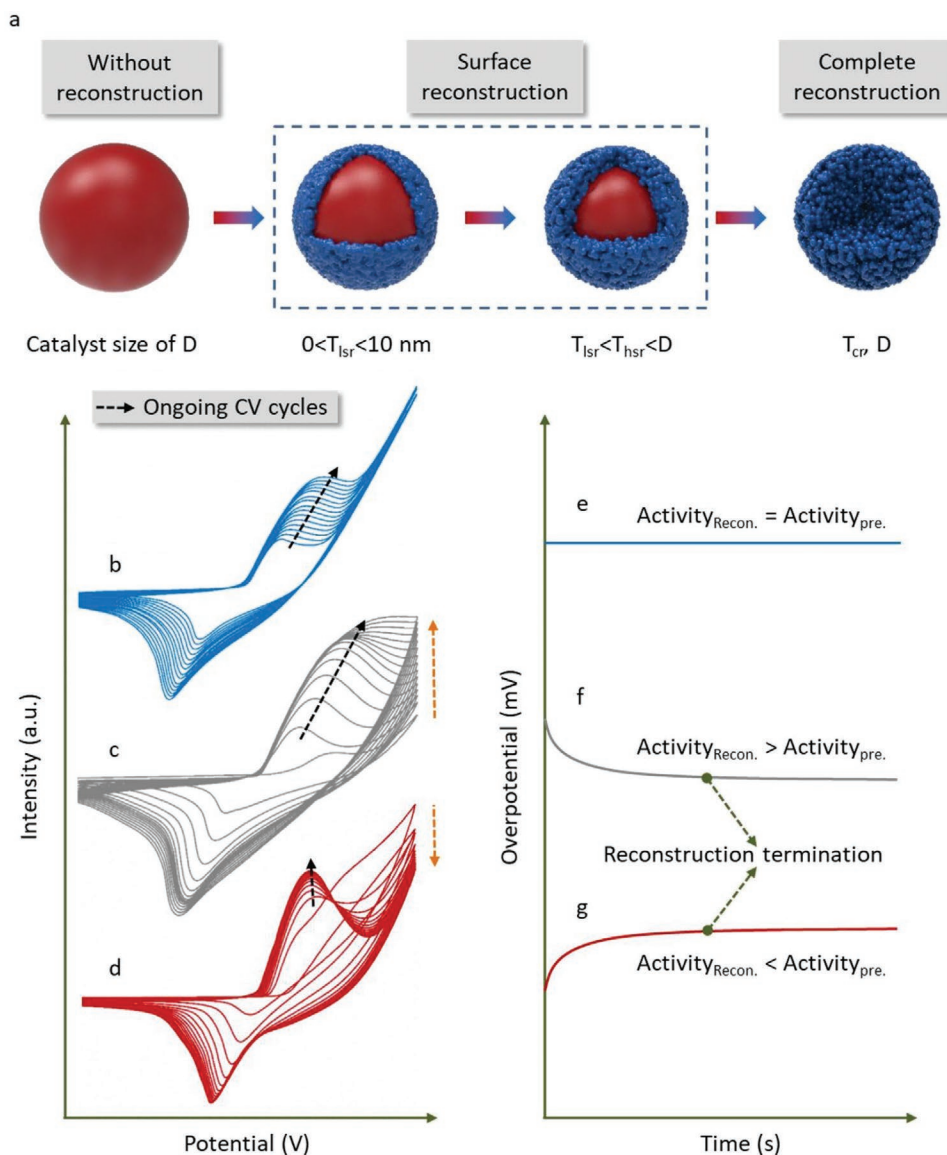
**ADVANCED
MATERIALS**

www.advmat.de

Figure 2. a) Schematic diagram for the microstructure and reconstruction degree among standard spherical particle precatalyst and its reconstructed catalysts. D represents the diameter of precatalyst. T_{lsr}, T_{hsr}, and T_{cr} represent the thicknesses for low degree of surface reconstruction, high degree of surface reconstruction, and complete reconstruction catalysts, respectively. Schematic diagrams for three representative b–d) CV and e–g) chronopotentiometry curves of nickel-based OER precatalysts during initial reconstruction activation processes.

Ni(II)/Ni(III) oxidation peak and the current at oxygen release potential greatly increased. Similar phenomena also appear in other precatalysts, such as NiFeO$_x$F$_y$,[27] fluoride-incorporating NiFe hydroxide,[26] multimetal-site alloy,[31] Ni$_x$B,[32] Co$_2$(OH)$_3$Cl,[33] and so on. For the third case, it is also rarely reported so far and has been observed in our recent work.[29] We firstly fabricated bulk Ni particles on the nickel foam, which were then carried out under alkaline OER condition. During its initial 30-cycle CV measurement, the redox peak current gradually increased but the current at high potentials decreased. Since most precatalysts show increased activity after reconstruction and the reconstructed species provide real catalytic sites and high catalytic activities, it is valuable to deepen the reconstruction degree and develop completely reconstructed catalysts.

The above-mentioned cases can also be reflected from chronopotentiometry or chronoamperometry tests. Taking chronopotentiometry test as an example, the curves corresponding to the three cases are shown (Figure 2e–g). The overpotential almost remains unchanged for the first case. The OER activity of precatalyst (denoted as activity$_{pre.}$) is close to that of reconstruction one (activity$_{recon.}$). Therefore, though more reconstructed species are generated during the reconstruction process, the oxidation current at high potentials changes little. For the second case, as the activity$_{recon.}$ is higher than activity$_{pre.}$, there should be that more reconstructed species produce higher OER current/activity. After achieving reconstruction as much as possible and the reconstruction terminates, the chronopotentiometry response shows the unchanged overpotential as shown in Figure 2f. This

phenomenon was observed when we studied the reconstruction of $NiMoO_4 \cdot xH_2O$ OER precatalyst.[25] Similarly, if activity$_{recon.}$ is lower than activity$_{pre.}$, the overpotential increases till reconstruction terminates (Figure 2g). In this case, the reconstruction has a negative effect on the performance of catalyst. For example, during the stability test of Ni–Fe selenide OER catalyst, its activity decayed gradually.[34] This phenomenon could be attributed to the lower intrinsic activity of reconstructed (oxy)hydroxide than that of the original selenide. Therefore, how to inhibit the reconstruction and remain the original high-activity of precatalysts in this case is a challenge. In fact, it is difficult to assess the true activity of precatalysts because the conversion of precatalysts to reconstructed species occurs while the electrochemistry is in progress. Theoretical calculations based on precatalysts for activity analysis are not meaningless, and these theoretical results might explain why the CV curve or chronopotentiometry response shows like this. Taking $Co_2(OH)_3Cl$ precatalyst as an example,[33] its initial CV cycles during alkaline OER were similar to the case in Figure 2c. More and more generation of CoOOH was responsible for the displayed CV curves and the much enhanced OER activity. Such a phase reconstruction activated the original precatalyst. Besides, the 1st-cycle CV could approximately reflect the activity of $Co_2(OH)_3Cl$, and the ever-increasing faradaic pseudocapacitance in the following CV curves could confirm that the activity of CoOOH is higher than that of $Co_2(OH)_3Cl$. Nevertheless, the intrinsic activity of $Co_2(OH)_3Cl$ is hard to obtain because of the rapid reconstruction process. The authors have also calculated the theoretical overpotential based on CoOOH model, demonstrating its high OER activity. Therefore, if the theoretical overpotential based on $Co_2(OH)_3Cl$ is analyzed, it can not only reflect its intrinsic activity, but can also explain why the CV curves show like this. However, comparing the activity between precatalysts and the reconstructed species based on theoretical calculations is poorly studied. Hence, it is recommended to uncover the relationship between CV curve/chronopotentiometry response and reconstruction phenomenon. Furthermore, it is hard to avoid the reconstruction phenomenon of some instable precatalysts, especially under industrial harsh conditions. Compared to surface reconstruction, the complete reconstruction which can produce more quantity of active species would be the better choice. Therefore, the complete reconstruction is highlighted in this review.

In addition, according to the types of transformations, the reconstruction results could also involve the following aspects, which contain topology reconstruction (e.g., changes in roughness, porosity, microstructures),[24–26,35,36] chemical reconstruction (i.e., changes in composition, phase),[25,26,30,31,37–39] and crystallographic reconstruction (e.g., preferential crystal planes, changes in crystallinity),[24,25,30,33] and so on. This is also clearly presented in **Figure 3**, which will make it easier for researchers to understand the specific reconstruction characteristics discussed later. Besides, the reconstruction results of actual catalysts are generally complex with the changes of multiple parameters. For example, in the complete reconstruction from $NiMoO_4 \cdot xH_2O$ to NiOOH, the reconstruction results contained the topology reconstruction (from solid nanowire to ultrasmall nanoparticle-interconnected nanowire structure), chemical reconstruction (the loss of Mo species and H_2O and the change of phase), and crystallographic reconstruction (from high crystallinity to low crystallinity).[25]
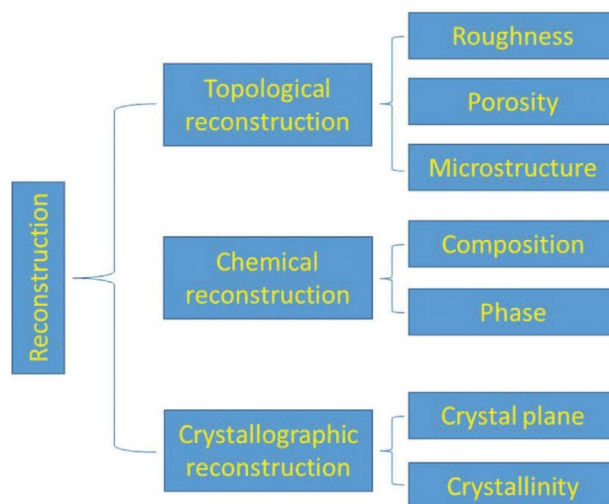

Figure 3. The reconstruction results according to the types of transformations.

2.1.3. Characterizations on the Thickness of Reconstruction Layer

Obviously, the most intuitive and visible evidence on the thickness of reconstruction layer is characterized by transmission electron microscopy (TEM). Especially, for precatalysts with bulk morphology, or if specific elements exist only in the reconstructed layer or in the precatalyst, it is easy to determine the thickness of the reconstruction layer via high-resolution TEM (HRTEM) combined with element mapping.[17,24] The contrast of reconstructed catalyst under scanning TEM (STEM) mode may also provide preliminary judgment.

2.2. Advantages of Completely Reconstructed Catalysts

In terms of structure characterizations, the completely reconstructed catalysts have reported to have the following features and also summarized in **Figure 4**. It should be noted that although some of the examples given are about partial reconstruction, if complete reconstruction can be achieved, the reconstructed species can inherit and exhibit properties which are similar to those in the surface reconstruction.

1) Low-/polycrystalline or amorphous structure, which is accompanied by abundant vacancies/defects, active sites, or unsaturated metal atom coordination.[17,25,26,40–42] For example, our group identified the thermal induced complete reconstruction (TICR) mechanism on $NiMoO_4$ precatalyst.[24] The completely reconstructed (oxy)hydroxide showed polycrystalline characteristics, accompanied by numerous grain boundaries and vacancies, which were beneficial for high-efficiency OER catalysis. Geyer et al. confirmed that the reconstructed species for FeB_2 OER precatalyst were amorphous FeOOH.[43] Xu et al. studied a pseudocubic $SrCo_{0.9}Ir_{0.1}O_{3-\delta}$ perovskite for OER catalysis.[44] The Sr and Co leached from $SrCo_{0.9}Ir_{0.1}O_{3-\delta}$ surface during electrochemical tests in acid, resulting in 10 nm thick amorphous IrO_xH_y layer with no long-range order. Zeng et al. developed a lithium-intercalated

**ADVANCED
SCIENCE NEWS**

www.advancedsciencenews.com
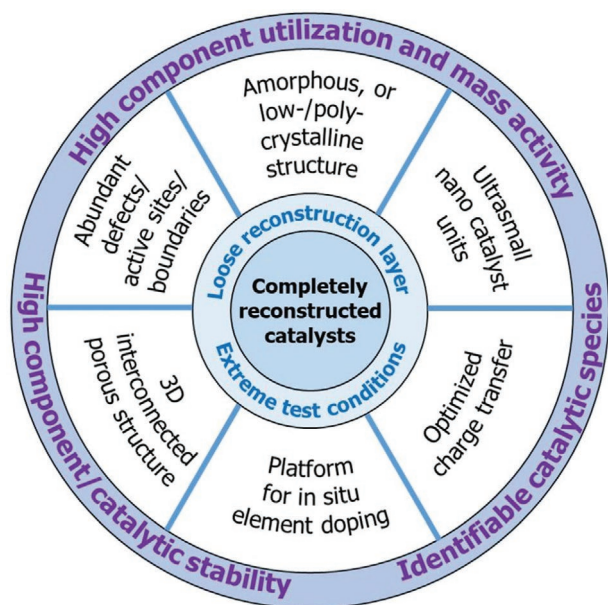
**ADVANCED
MATERIALS**

www.advmat.de

Figure 4. Prerequisites for complete reconstruction and a summary for the functions/advantages of the completely reconstructed catalysts.

iridium diselenide (Li–IrSe₂) for high-performance OER and overall water splitting applications in both acidic and neutral conditions.[45] After lithiation and electrooxidation treatment, the surface of Li–IrSe₂ generated 7 nm thick Ir oxide particle layer with defects and poor crystallinity.

2) Ultrasmall nanocatalysis unit interconnected porous structure, which is generally attributed to the leaching of component.[33,38] This structure is featured by rich grain boundaries, and the pores between nanoparticles can promote the effective solution permeability and gas diffusion. Meanwhile, the interconnected structure can avoid agglomeration during catalysis process. For example, our group found that the hydrated molybdate precatalysts could completely reconstruct to (oxy)hydroxides under electrochemical oxidation and normal conditions.[25] The reconstructed products were featured by ≈5 nm nanoparticle-interconnected structure.

3) Identifiable catalytic species, high stability, and component utilization maximization. Compared with the surface reconstructed catalysts, the completely reconstructed one displays a clearer component for catalytic mechanism analyses.[33] As the reconstructed species are thermodynamically stable after reconstruction, the completely reconstructed catalyst is expected to display high catalytic/component stability.[24] Meanwhile, complete reconstruction will make each component of catalyst be used for catalysis reactions as much as possible, and thus maximize the component utilization. For example, our group confirmed that the completely reconstructed NiOOH could provide stable OER catalysis for 1350 h to meet industrial requirements.[25] It displayed much enhanced mass activity than that of incompletely reconstructed $NiMoO_4$@NiOOH.

4) Uniform and tunable element doping. Some literatures have reported the presence of residual elements from precatalysts in reconstructed species. Cho et al. confirmed the residual S in the developed NiFe (oxy)hydroxide catalyst, and it could

significantly reduce the adsorption free energy difference between O* and OH* intermediates on the Fe sites and thus promoted the high OER catalysis.[46] Wang et al. revealed the existence of residual P was responsible for the structural distortion in activated phosphides.[37] Since the reconstructed species provide the real catalytic sites, these phenomena may explain why the catalytic activity of directly synthesized hydroxides is not as high as that of reconstructed ones.

5) Optimized charge transfer. The conductivity change of electrode before and after reconstruction could be reflected using electrochemical impedance spectra (EIS) measurements.[23] For example, during the complete reconstruction from $NiMoO_4 \cdot xH_2O$ to NiOOH, the charge transfer resistance (R_{ct}) values decreased significantly from 34 to 6.5 Ω.[25] Meanwhile, the R_{ct} values gradually decreased with the deepening of reconstruction. Therefore, the reduced R_{ct}, which is related to better charge transfer and improved catalytic kinetics, could be one of the reasons for the enhanced catalytic activity of the completely reconstructed catalyst.

Though the better mechanical stability of surface reconstruction catalyst than that of completely reconstructed one has been reported, detailed evidences and explanations were not provided.[26] Therefore, the mechanical stability among catalysts with different reconstruction results still requires further experimental analyses and theoretical understandings. Summarily, according to the current reports, the completely reconstructed catalysts have the characteristics of amorphous or low-/poly-crystalline structure, dense reconstruction layer or lose one with interconnected nanoparticles, abundant grain boundaries, numerous defects, and possible residues, etc. Engineering on complete reconstruction could provide a new strategy for novel material synthesis, which will be described in Section 4.1.

2.3. Design Principles

Considering the reconstructed species provide the real catalytic sites, the catalysts with deeper reconstruction thus possess more catalytic species and allow for better catalysis. To achieve complete reconstruction of precatalysts, the following strategies/ways could be considered. 1) Building nanostructured precatalysts with at least one dimension of below 10 nm, because many precatalysts show the thickness of reconstruction layer of below 10 nm,[25] and the catalytic sites are generally limited to a near-surface region.[47] Despite the limited mass transfer process, the reconstruction with several nanometer level can be realized in this dimension. For bulk precatalysts, the battery lithiation method could be adopted for downsizing materials,[29] though the pulverization of materials is harmful to the battery electrode. 2) Designing precatalysts with multicomponent coleaching during the reconstruction process. Leaching of these species will probably form the loose reconstruction layer, and thus promote the effective diffusion of electrolyte and further electro-oxidation.[25,42] 3) Operation under extreme test conditions, here mainly includes the operation temperature, solution concentration, higher oxidation potentials, and operation time, which enables deeper reconstruction as much as possible.[24,48] To sum up, realizing effective mass transport
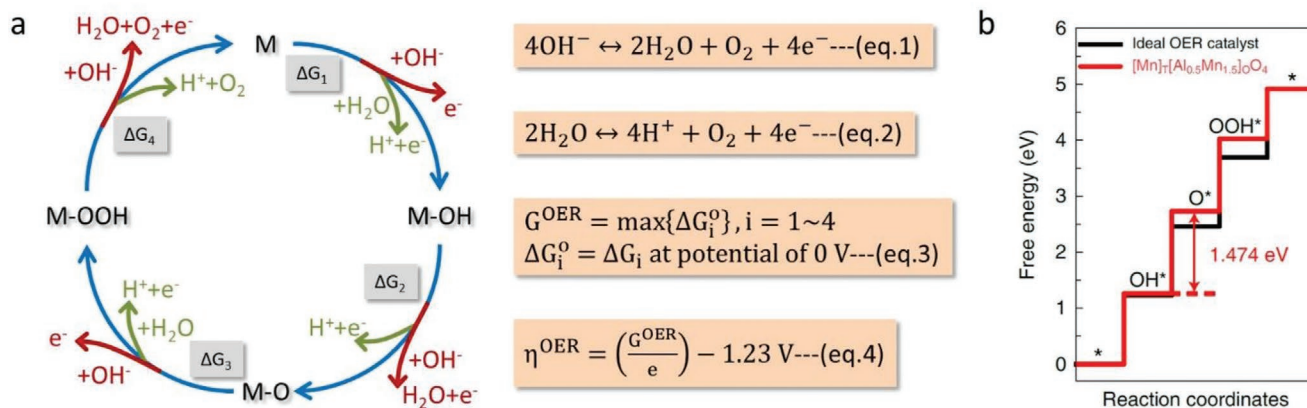
Figure 5. a) OER mechanisms in acidic/neutral (green marks) and alkaline (red marks) electrolytes. b) Free energy diagrams on the most close-packed surface of $[Mn]_T[Al_{0.5}Mn_{1.5}]_OO_4$ oxide and for the ideal OER catalyst. Reproduced with permission.[49] Copyright 2019, Springer Nature.

or developing strategies to trigger chain reconstruction are supposed to achieve complete reconstruction, and the strategies are summarized in Section 3.4.

3. Complete Reconstruction for OER

3.1. OER Fundamental Mechanism

Figure 5a shows the acidic/neutral (green marks) and alkaline (red marks) OER mechanisms, and Equations (1) and (2) are the total equations of OER in alkaline and acidic electrolytes, respectively. OER involves complex four-electron transfer processes, in which the formed intermediates include HO*, O*, and HOO* adsorption species whether in acidic or alkaline electrolytes. Thermodynamically, the equilibrium potential of OER is 1.23 V versus reversible hydrogen electrode (RHE). However, the potential of actual catalysts will be higher than 1.23 V due to the nonideal test conditions (solution resistance, contact resistance between catalyst and collector, etc.) and the reaction barrier brought by nonideal catalytic active sites.[50] Its slow reaction kinetic results in high overpotentials of oxygen evolution catalysts, which greatly reduces the energy conversion efficiency of the systems (such as water splitting and fuel cells) and restricts their industrial-scale applications. Theoretical calculation plays an important role in evaluating and predicting the activity, explaining the possible catalytic process and performance improvement mechanism of the catalyst. Based on theoretical calculation and combination of Equations (3) and (4), the theoretical overpotentials of catalysts can be given. The free energy diagram of the ideal catalyst is shown in Figure 5b (black line), which means that all the reaction free energies are zero at the equilibrium potential of 1.23 V.[51] However, the catalyst that meets this principle is thermochemically ideal, and the practical catalyst does not exhibit this characteristic. Taking the reported spinel $[Mn]_T[Al_{0.5}Mn_{1.5}]_OO_4$ catalyst as an example, the density functional theory (DFT)-calculated OER free energy diagram on its most close-packed surface is displayed (red line in Figure 5b).[49] It was found that there was insufficient adsorption ability in the formation of O* and HOO*. The formation of O* adsorption species (ΔG_2: OH* + OH$^-$ → O* + H$_2$O) was

the rate-determining step, and its theoretical potential was 1.474 V. This work predicted that $[Mn]_T[Al_{0.5}Mn_{1.5}]_OO_4$ was a highly active OER catalyst, and the experimental results also confirmed its excellent catalytic activity. Therefore, employing theoretical calculations to find materials with suitable adsorption energy for intermediates will be an effective way to develop top-performance oxygen evolution catalysts.

3.2. Types of Reconstruction-Involved Precatalysts

The reconstruction phenomena of transition metal and noble metal-based catalysts in OER have been reported. Among them, most of the researches focus on transition metal-based catalysts in alkaline OER, which will be the main content of this section. The types of reconstruction-involved precatalysts include inorganic compounds (metals/alloys, oxides/hydroxides, phosphorus/boron-containing compounds, dichalcogenides, carbides/nitrides, etc.), metal organic frameworks (MOFs), Prussian blue analogues (PBAs), and hydrates. Because most of the transition metal-based materials are highly soluble under strongly acidic conditions, the reported reconstruction phenomena under acidic conditions mainly focus on noble metal-based catalysts. Besides, due to the inherently low ion concentration and large ohmic loss in neutral solution, the catalysts under this condition exhibit lower catalytic kinetics than those under acidic or alkaline conditions. Currently, only a few literatures reported reconstruction phenomena in neutral OER. Therefore, this section will regard the pH of test solution (i.e., alkaline, acidic, and neutral one) as a classification standard, and introduce the reconstruction-involved OER precatalysts under these conditions. This section is intended to present the reconstruction-involved precatalysts, and their catalytic performances are expected to be further improved via the strategies summarized in Section 3.4.

3.2.1. Precatalysts for Alkaline OER

In recent years, nonprecious metal-based catalysts have been widely studied due to their low cost and simple synthesis
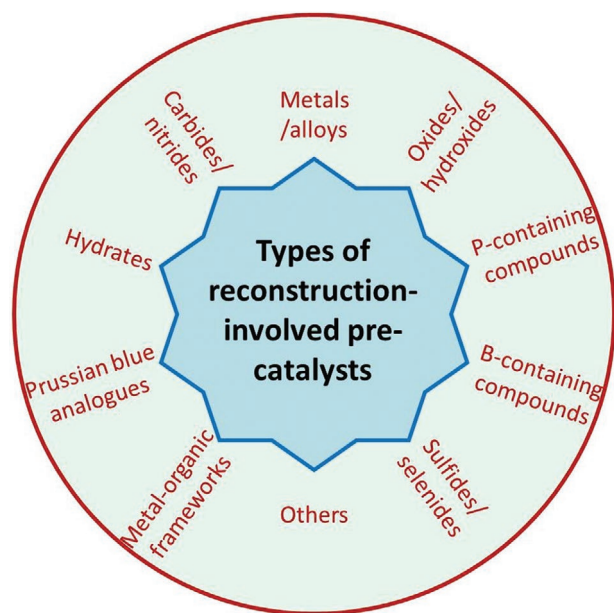
Figure 6. Types of reconstruction-involved nonprecious metal-based alkaline oxygen-evolving precatalysts.

technology. Among them, Fe/Co/Ni metal-based compounds containing B, N, S, Se, or/and P have been proven to possess superior activity than those of commercial RuO_2 and IrO_2. With the in-depth study of oxygen evolution mechanism of these catalysts, especially considering the in situ catalysis under operation conditions, it has been discovered that the microstructure/phase evolution exists on the surface of most catalysts. This section will briefly introduce these reconstruction-involved precatalysts according to the following categories shown in **Figure 6**. Typical examples for each type, and their reconstructed species as well as the applied characterizations are provided and displayed in **Table 1**.

Metals/Alloys: Metal or alloy materials as one family of OER catalysts have high conductivity and potential applications in electrocatalysis. However, surface oxidation of these materials occurs when exposed to the air. For example, Li et al. found that there was an oxide layer on the surface of Ni–Mo alloy catalysts.[86] When they are unstable in strong alkali and at high oxidation potential, the obvious phase reconstruction from alloy phase to (oxy)hydroxide phase will easily occur.[31] Metal/alloy materials with carbon coating are also widely applied in catalysis due to their strong acid/alkali resistance.[87,88] The active sites of these catalysts generally exist on the surface of carbon layer, and the catalytic performance is optimized due to its modulated electronic structure by internal components. Because of the tight coating of outer carbon, the internal metal species can be protected from oxidation. For example, Wang et al. reported the carbon-coated NiFe alloy catalyst with ≈4 nm thick carbon layer, and no oxidation of alloy was found after 35 h of stability testing in alkaline OER.[89] The nitrogen-doped carbon-coated FeNi oxygen evolution catalyst reported by Bao group was also not directly observed about the existence of surface reconstruction layer.[90] However, the oxidation peak of $Ni^{2+} \rightarrow Ni^{3+}$ was found in the linear sweep voltammetry (LSV) curve after 10 000 cycles of CV test. The author attributed it to the occurrence of carbon layer cracking caused by strong

oxidation condition in alkali. There have also been some reports on the phase evolution phenomenon for carbon-coated OER catalysts.[54,55,91] Therefore, it is not clear currently whether the carbon-coated OER catalysts will definitely undergo reconstruction, but the reconstruction occurrence is closely related to the material structure and test conditions (such as solution concentration, testing time). The analysis of the intrinsic catalytic mechanism for these catalysts should be associated with whether the reconstruction exists during catalysis.

Oxides/Hydroxides: Metal oxides possess flexibility and diversity in component and structure, and thus their catalytic activity can be improved by adjusting the charge, orbital and ligand of metal ions. The main synthetic methods include high-temperature sintering,[40,92] flame spraying,[93] and electrochemical methods.[29] Oxide-based materials in OER catalysis mainly contain single metal oxides,[30] multimetal oxides,[40] Li (or Na, K)-containing layered oxides,[39,94] perovskites,[56,93] etc. For single metal oxides (AO_x), such as NiO, CoO, or Co_3O_4, the surface is often reconstructed to form oxyhydroxide.[29,95,96] Strategies such as morphology design and vacancy engineering can promote the occurrence of this reconstruction process and further realize the improvement of OER activity. For example, Wang et al. studied the performance improvement mechanism of Co_3O_4 with rich oxygen vacancies compared to pure spinel Co_3O_4 in alkaline OER.[97] They found that oxygen vacancies promoted the preoxidation of low-valence state Co and deprotonation of the intermediate Co—OOH*. Multimetal oxides (ABO_x) have also been investigated as OER precatalysts, but their catalytic activity is not necessarily higher than that of the corresponding single metal oxide.[98,99] Due to diverse components and structures, the reconstruction of multimetal oxides can be motivated through strategies such as crystallinity control and element doping,[40,100] resulting in improved catalytic performance. Yu et al. compared the catalytic activity and reconstruction results of crystalline and amorphous NiFeMo oxide in alkaline OER.[100] Amorphous NiFeMo oxide was confirmed to achieve surface phase change in a shorter time and could form the oxyhydroxide active layer with abundant oxygen vacancies. This realized high mass activity which was 8 times that in crystalline one. Xu et al. developed a method to promote the surface phase reconstruction of inert $CoAl_2O_4$ via replacing Al with a small amount of Fe, which facilitated the preoxidation of Co and the formation of active CoOOH.[40] Li (or Na, K)-containing layered oxides used in battery energy storage also receive attentions for applying in OER catalysis. These catalysts can be divided into two types according to whether the reconstruction exists[39,101] or not.[94,102] Most works have uncovered that the surface chemical reconstruction would occur. For example, Li et al. found that $Li_2Co_2O_4$ underwent a spontaneous delithiation reaction under an applied voltage, which promoted the formation of surface-active species.[39] Perovskite oxides are featured by the diversity of structures and components, high degree of freedom for cation arrangement, and could provide efficient OER activity in alkaline medium. Shao et al. systematically summarized the nanosynthesis strategy of perovskite electrocatalysts and their application in OER.[103] For perovskite oxides in the form of ABO_3, they can exhibit the optimal OER activity when the B-site metal has an electron filling state close to e_g. However, double perovskite oxides

Table 1. Summary for the types of reconstruction-involved nonprecious metal-based precatalysts in alkaline OER, reconstructed species and their applied characterizations. * means that the testing temperatures have not been mentioned or ambiguous. RT means room temperature.

Types	Precatalysts	Electrolytes (temperatures)	Reconstructed species	Applied characterizations	Ref.
Metals/alloys	$FeNi_3$, NiCu	1 M KOH*	Low-crystalline Fe/Cu doped NiOOH	Ex situ XPS, TEM	[31]
	MnFeCoNi high entropy alloy	1 M KOH*	Polycrystalline oxides	Ex situ TEM, XPS	[52]
	Core–shell Cu@NiFe LDH	O_2-saturated 1 M KOH*	CuO	Ex situ XPS	[53]
	Graphite-encapsulated metals and alloys	Ar purged 1 M KOH*	Oxide layers	Ex situ XPS	[54]
	Nickel/carbon composites	1 M KOH bubbled with O_2 (RT)	Low-crystalline NiOOH	Ex situ XRD, SEM, HRTEM, XPS	[55]
Oxides/hydroxides	Co_3O_4 nanoparticles	0.1 M KOH*	Amorphous CoO_xH_y, crystalline CoO, CoOOH, $Co(OH)_2$	In situ EC-TEM	[30]
	$CoFe_{0.25}Al_{1.75}O_4$	1 M KOH (25 °C)	Amorphous Co oxyhydroxide	In situ XANES; Ex situ HRTEM	[40]
	$Li_2Co_2O_4$ particles	O_2-saturated 1 M KOH*	Amorphous $Li_xCo_2O_{4-\delta}(OH)_\delta$ (Co^{3+}/Co^{4+})	Operando XAS; Ex situ XPS, XRD, HAADF-STEM	[39]
	La_2NiMnO_6	1 M KOH bubbled with O_2*	Amorphous nickel (manganese) oxide/hydroxide	Ex situ HRTEM	[56]
	Single-atom Au/NiFe LDH	Ar-saturated 1 M KOH*	Oxyhydroxide	In situ Raman; Ex situ XANES	[57]
P-containing compounds	Ni_2P hollow microspheres	1 M KOH (pH ≈ 13.75, RT)	Low-crystalline NiOOH	In situ Raman; Ex situ HRTEM, XPS	[58]
	Co_xN and Co_xP	1 M KOH*	Low-crystalline Co_xO	Ex situ HRTEM, AR-XPS, NEXAFS	[37]
	$Co_{1.6}Ni_{0.4}P_4O_{12}$-C	1 M KOH*	Low-crystalline oxyhydroxide	Ex situ XRD, SEM, HRTEM	[59]
	Iron-doped nickel phosphate	1 M KOH*	NiOOH	Ex situ XPS	[60]
	$Ni_2P_4O_{12}$	O_2-saturated 1 M KOH (RT)	Amorphous oxyhydroxide	Ex situ XRD, XPS	[61]
B-containing compounds	FeB_2 nanoparticles	1 M KOH*	Amorphous FeOOH	Ex situ XRD, SEM, HRTEM	[43]
	Boronized Ni sheets	1 M KOH*	Amorphous metaborate-containing oxyhydroxide	Ex situ XPS, AFM, HRTEM	[62]
	Ni_xB nanosheets	O_2-saturated 1 M KOH*	Nickel oxyhydroxide	Operando XANES	[32]
	Co_2B	O_2-saturated 1 M KOH*	Cobalt oxide/hydroxide	Ex situ XPS	[63]
	Fe–Ni–P–B–O	O_2-saturated 1 M KOH (RT)	Oxide/(oxy)hydroxide	Ex situ XPS FT-EXAFS	[64]
Dichalcogenides	Ni_3Se_2, NiSe nanoparticles	O_2 purged 0.1 M KOH (RT)	Amorphous oxide layer	Ex situ XPS HRTEM	[65]
	Ni–Fe disulfide	1 M KOH (23 ± 1 °C)	Polycrystalline γ-Ni(Fe)OOH	Ex situ HRTEM	[66]
	Amorphous CoS_x	1 M KOH*	Crystalline CoOOH	In situ HRTEM; Ex situ XPS, SEM, TEM	[67]
	FeS nanosheets	1 M KOH*	Amorphous FeO_x	Ex situ SEM, HRTEM, XPS	[68]
	Cobalt covalent doping in MoS_2	1 M KOH (RT)	High valence state Co species	Operando EXAFS	[69]
Carbides/nitrides	Co_3C particles	N_2 purged 1 M NaOH (RT)	Amorphous CoO_x	Ex situ XPS, HRTEM	[38]
	Ni_3C nanoparticles	O_2 purged 1 M KOH*	Low-crystalline NiO_x	Ex situ XANES, EELS, HRTEM	[70]
	Co_4N porous nanowires	1 M KOH bubbled with O_2*	Low-crystalline CoO_x	Ex situ XRD, XPS, XANES, HRTEM	[41]
	NiMoN@NiFeN nanowires	1 M KOH+seawater (pH ≈ 14, RT)	Amorphous NiFe oxides/(oxy)hydroxides, $Ni(OH)_2$	In situ Raman; Ex situ HRTEM, XPS	[71]
	CoN	O_2 purged 1 M KOH (25 °C)	Low-crystalline Co_3O_4	Ex situ XPS, HRTEM	[72]
MOFs	$(Ni_2Co_1)_{0.925}Fe_{0.075}$-MOF	O_2-saturated 1 M KOH (pH = 14, RT)	Low-crystalline hydroxides/oxyhydroxides	Ex situ XRD, Raman, XANES, FTIR	[73]
	CoBDC-Fc	1 M KOH*	Amorphous CoOOH	Ex situ XPS	[74]
	ZIF-67	1 M KOH*	Low-crystalline $CoOOH/Co(OH)_2$	In situ UV–vis, Raman; Ex situ XRD, XPS, SEM, HRTEM	[36]
	Ni-MOF@Fe-MOF	O_2-saturated 1 M KOH*	Low-crystalline $NiO/NiOOH$, Fe_2O_3	Ex situ (HR)TEM, XPS, Raman	[75]
	N,S codoped MOF	1 M KOH (RT)	Hydroxide/oxyhydroxide	Ex situ SEM, XRD, FTIR, XPS	[76]

Table 1. Continued.

Types	Precatalysts	Electrolytes (temperatures)	Reconstructed species	Applied characterizations	Ref.
Prussian blue analogues	$K_2NiFe(CN)_6$-V_{CN}	O_2-saturated 1 м KOH (RT)	NiFeOOH	Ex situ FTIR, Raman, XAS	[77]
	NiFe Prussian blue analog	O_2-saturated 1 м KOH*	Amorphous $Ni(OH)_2$/$NiOOH_{2-x}$	Operando XAS; Ex situ TEM, XRD	[78]
	Ni–Co–Fe Prussian blue analogue	N_2 purged 0.1 м KOH*	Hydroxides	Ex situ TEM	[79]
	$Na_xCoFe(CN)_6$ nanosheets	O_2-saturated 1 м KOH*	CoOOH	Ex situ XRD, TEM, XAS	[80]
	Fe–Co PBAs	1 м KOH*	Hydroxides	Ex situ XPS	[81]
Hydrates	$LiCo(H_2O)_2[BP_2O_8]\cdot H_2O$	1 м KOH (RT)	Amorphous $Co(OH)_2$/CoOOH	In situ XAS; Ex situ TEM, XPS, XRD, FT-IR	[82]
	$NiMoO_4\cdot xH_2O$ nanowires	1 м KOH (RT)	Low-crystalline NiOOH	In situ Raman; Ex situ HRTEM	[25]
	$Co(CO_3)_{0.5}(OH)\cdot0.11H_2O$ nanowires	1 м KOH (RT)	Low-crystalline CoOOH	Ex situ HRTEM	
	$CoMoO_4\cdot0.75H_2O$ nanowires	1 м KOH (RT)	Low-crystalline CoOOH	Ex situ HRTEM	
	$NiMoO_4\cdot xH_2O$ nanosheets	1 м KOH (RT)	Low-crystalline NiOOH	Ex situ HRTEM	
Others	$K_{0.8}Na_{0.2}(MgMnFeCoNi)F_3$	1 м KOH (RT)	Low-crystalline oxides or hydroxides	Ex situ XRD, HRTEM	[83]
	$Co_2(OH)_3Cl$ nanoparticles	1 м KOH*	Crystalline β-CoOOH	In situ XAFS; Ex situ XRD, HRTEM	[33]
	$Ni_{0.9}Fe_{0.1}PS_3$ nanosheets	1 м KOH*	Crystalline Ni(Fe)OOH and Ni(Fe)$(OH)_2$	Ex situ HRTEM, XPS, Raman	[84]
	NiFe–OH–F nanosheets	Ar-saturated 1 м NaOH*	Amorphous NiFe oxide	Ex situ XRD, XPS, HRTEM	[26]
	Tannin–NiFe complex	1 м KOH*	Amorphous $Ni_xFe_{1-x}O_yH_z$	In situ Raman; Ex situ XPS, FTIR, XAS, HRTEM	[85]

in the form of $A_2BB'O_6$ can realize modulation of electronic structure and optimization of performance when the B site is alternately occupied by different metal cations B and B'.[56] Most perovskite materials would occur surface phase reconstruction during OER processes.[93,104,105] For example, Xie et al. revealed that the Jahn–Teller effect promoted the formation of an amorphous Mn/Ni hydroxide/oxide layer on La_2NiMnO_6 during OER.[56] Nevertheless, a few papers have reported that no chemical reconstruction phenomenon exists in perovskite materials during OER catalysis, such as $Ba_4Sr_4(Co_{0.8}Fe_{0.2})_4O_{15}$.[106]

Layered hydroxides (AO_xH_y), including single metal hydroxides and double-metal hydroxides (typically layered double hydroxides, LDHs), usually have a brucite-type structure in which the metal atom layer and proton alternately stack.[26,57,107–109] Among them, LDHs have been widely studied due to their flexible and adjustable structures and components as well as simple synthesis methods. They are expected to become high-performance OER electrocatalysts for large-scale industrial applications. Xiong et al. systematically summarized the latest advances of LDH-based OER catalysts in terms of synthesis strategy, structure regulation, and factors that affect catalytic activity.[110] Among these hydroxides, $NiFeO_xH_y$[47] has been considered as the best catalyst for OER and the first choice for water electrolysis in industry. Some reported experiments have found that the reconstructed active species are hydroxides. For example, Paik et al. confirmed that the surface of Ni–P catalyst was reconstructed to oxide/hydroxide after OER catalysis.[111] However, the hydroxides have also been discovered the existence of chemical reconstruction during electro-oxidation processes. For example, Zhang et al. revealed the transforma-

tion of LDH to oxyhydroxide under oxidized potentials by using in situ Raman technique.[57]

P-Containing Compounds: These compounds include phosphides and phosphates. Compared to semiconducting or insulating oxides, metallic-like phosphides have attracted much attention in OER catalysis due to their optimized electrons transfer, abundant active sites, good acid/alkali resistance and stability.[112,113] Recently, Jiao et al. summarized the application of multifunctional transition metal phosphides in energy electrocatalysis, including the synthesis strategies, modification methods, and multifunctional applications in detail.[114] The current phosphide-based oxygen evolution catalysts are mainly focused on Fe/Co/Ni-based materials, in which surface reconstruction phenomenon basically occurs in OER catalysis.[37,111,115,116] Chen et al. reported that the core–shell Ni_2P/NiOOH structure formed after surface phase reconstruction of Ni_2P precatalyst.[58] In this reconstructed structure, the high-valent Ni species on the surface promoted the electrostatic adsorption of OH^-, and the preserved Ni_2P core enhanced the electron transfer in catalysis. Their synergistic effect guaranteed the reconstructed catalyst with excellent OER catalytic activity. For other phosphides such as MoP, a typical HER catalytic material, there is also a phase reconstruction phenomenon and the formation of oxide layer.[117]

Due to low price, environmental friendliness and high stability, phosphates have promising application prospect in energy conversion and storage. Yuan et al. systematically summarized the synthesis strategies of phosphates and their applications in OER and zinc–air batteries.[118] The phosphate group in metal phosphates has flexible coordination, and thus they have significant advantages in designing high-activity

**ADVANCED
SCIENCE NEWS**

www.advancedsciencenews.com

**ADVANCED
MATERIALS**

www.advmat.de

electrocatalysts. For example, Cao et al. realized the transformation of cobalt phosphate from octahedron to tetrahedron by dehydration at high-temperature treatment.[119] The electrocatalytic results showed that $Co_3(PO_4)_2$ with cobalt tetrahedron had higher activity than that of $Co_3(PO_4)_2 \cdot 8H_2O$ with cobalt octahedron, which was attributed to that Co tetrahedral site could promote the formation of high-valent cobalt active species in OER. Besides, the phosphate group has also been confirmed to be proton acceptors and can induce distorted local structure, and thus is conducive to water adsorption and catalytic oxidation.[59,120] In spite of this, the low electrical conductivity limits the charge transport of phosphates during catalysis. Strategies such as carbon compounding[59] or elemental doping[61] are widely used to improve conductivity and further accelerate catalytic kinetics. Although the phosphates have excellent structural stability, the existence of reconstruction for these OER catalysts has been reported.[60,121,122] For example, Xu et al. confirmed that the Co–Ni cyclotetraphosphate nanoarrays derived from MOFs had obvious formation of oxyhydroxide reconstruction layer after stability test.[59] A handful of studies have not found the oxidation reconstruction phenomenon in some phosphates like $Li_{0.7}Co_{0.75}Fe_{0.25}PO_4$.[123]

B-Containing Compounds: Boron compounds mainly include borides and borates. Metal borides have the characteristics of strong acid/alkali resistance, good mechanical strength and conductivity, and variable structure composition. Early studies of borides have mainly focused on HER, such as Co_2B and $Ni–B_x$[63,124] which have been confirmed with excellent HER activity in a wide pH range. Their synthesis mainly includes reduction by reducing agents (such as borohydride and amorphous boron),[43,62] magnesium thermal reduction,[125] and chemical plating.[124] For metal borides, B atoms with higher electronegativity can obtain electrons from metal atoms. This enables the metal atom with more positive charges, which thus enhances its OH^- adsorption ability and acquires fast OER dynamics. Therefore, increasing the boron content is another effective way to improve the OER catalytic activity of borides in addition to the regulation of microstructure and morphology. Geyer et al. prepared a FeB_2 catalyst with high boron content.[43] Its OER overpotential $\eta@10$ mA cm^{-2} was only 296 mV, which displayed higher catalytic activity than those of borides with low boron content. Due to their self-instability, these borides usually undergo OER-induced reconstruction and form species such as oxides or oxyhydroxides.

Borates have good stability at room temperature, and their synthesis is mainly based on borohydride reduction,[64,126,127] solvothermal[128] and other methods. Borate catalysts also undergo surface reconstruction in alkaline OER. For example, Yan et al. reported an amorphous Fe–Ni–P–B–O nanocage oxygen evolution catalyst.[64] After the stability test, ex situ X-ray photoelectron spectroscopy (XPS) revealed that low-valent Ni, P, and B species were oxidized to the species with higher valence after OER. Ex situ XAS analysis further proved that the catalyst was partially reconstructed into metal oxide or oxyhydroxide.

Dichalcogenides: Similar to phosphides, dichalcogenides, which include sulfides, selenides, and tellurides, have strong corrosion resistance and high stability, and are mainly synthesized by hydrothermal or high-temperature solid-phase

strategies. Among them, the Fe/Co/Ni-based materials are usually applied in OER, in which there is also an obvious reconstruction phenomenon.[65,68,129–134] Cui et al. found that the highly crystalline CoS_2 would be completely reconstructed during alkaline OER catalysis, thus obtaining a nanoporous metal oxide as stable OER catalyst.[135] Yu et al. directly proved the amorphous $CoS_x–Co(OH)_2–CoOOH$ phase reconstruction processes by in situ HRTEM characterization.[67] More systematically, Cui et al. investigated a family of metal dichalcogenides (denoted as A–B, A = Fe, Co, Ni; B = S, Se, Te) OER precatalysts.[136] In the initial CV scan, the pronounced oxidation peaks appeared which presented the transformation from chalcogenides to oxides. These peaks completely disappeared in the following scans, suggesting their complete reconstruction. The reconstructed catalysts possessed a significant amount of defects, and thereby showed better OER activity than that of the pristine metal dichalcogenides. It has also been reported that the reconstruction of sulfides/selenides is incomplete. For example, Golberg et al. discovered that the $Ni(Fe)S_2$ catalyst formed 2–10 nm thick $Ni(Fe)OOH$ layer on the surface after reconstruction.[66] The obtained core–shell $Ni(Fe)S_2@Ni(Fe)OOH$ catalyst can simultaneously realize fast electron transport and rapid catalytic reaction. Layered MoS_2 is a typical active electrocatalyst in HER but has a poor activity in OER. However, phase reconstruction also exists when MoS_2 is used as an OER catalyst. For example, Zhao et al. captured the formation of Co–O and Mo–O in Co-doped MoS_2 catalyst after OER via in situ extended X-ray absorption fine structure (EXAFS) technique.[69] In particular, for selenides, selenium oxide (SeO_x) may also form and remain in the reconstructed catalyst.[137]

Carbides/Nitrides: Metal carbides have the characteristics of low cost and high conductivity, and are mainly synthesized by heat treatment[138] and colloidal liquid phase synthesis.[38,70] Carbides serve as potential high-efficiency OER catalysts.[112] For example, Xie et al. reported Ni_3C/C composite catalyst applied to alkaline OER, in which the intrinsic metallic character of Ni_3C realized rapid electronic conduction inside the catalyst and the conductive carbon layer promoted the charge transfer on the surface.[70] Therefore, Ni_3C/C catalyst showed better catalytic activity than pure Ni_3C, NiO, and NiO/C due to the "dual electron behavior control" engineering. After OER, the NiO_x layer was in situ generated on the surface of Ni_3C. The NiO_x layer not only provided OER active catalytic sites, but also prevented further oxidation of internal Ni_3C. This structure could achieve electrochemical stability in catalytic testing. The formation of core–shell carbide@reconstructed layer structure also existed in the reported Mo_2C precatalyst.[138]

Metal nitrides are mainly synthesized by ammonia-assisted heat treatment and solid-state calcination.[41,71,139] Metal nitrides generally have metallic character, such as Co_4N,[41] the temperature-dependent resistance test and DFT analysis have proved that it has typical metallic characteristics. This is beneficial to the effective electron transport between the catalyst surface and the current collector during the catalytic reaction process. Therefore, nitrides generally have better catalytic kinetics for oxygen evolution compared to semiconductive or insulative metal oxides. They also have the advantages of good catalytic performance, strong corrosion resistance, and high mechanical strength, and thus metal nitrides are considered as candidates

for water electrolysis applications. For example, NiMoN, Ni/Ni$_3$N, and Ni–Fe–Mo metal nitrides have been studied in alkaline water electrolysis,[139–142] and NiMoN@NiFeN has been used in alkaline seawater electrolysis.[71] Similar to carbides, nitrides undergo the reconstruction during OER operation. It has been confirmed a reconstructed layer of oxide/oxyhydroxide formed on the surface of Co$_4$N during alkaline OER.[41] Ex situ XAS analysis found that the Co–Co spacing in Co$_4$N catalyst was larger than that in metallic Co but smaller than that in Co$_3$O$_4$, which suggested that the Co atom on the surface of Co$_4$N catalyst was partially oxidized. Besides, the surface-sensitive XPS characterization revealed the decrease of zero-valent Co after the catalytic reaction. More directly, ex situ HRTEM proved the existence of surface reconstruction layer. It was worth noting that the thickness of reconstruction layer deepens as CV cycles increase, and finally a stable reconstruction layer with a thickness of 5–8 nm was formed. It suggested that the termination of reconstruction resulted in the core–shell structure of the Co$_4$N@reconstruction layer. Similar to Co$_4$N, the Ni$_3$N precatalyst also formed a NiOOH reconstruction layer during alkaline OER, which could be further oxidized into NiOO$_2$ at higher potentials.[143] Due to its excellent conductivity, the Ni$_3$N could provide more efficient electron transportation and thus resulted in high OER activity. Currently, the nitrides precatalysts with similar reconstruction phenomena have been reported, including CoN, Mn$_3$N$_2$, and so on.[72,139,144]

To sum up, the reconstruction of nitride and carbide precatalysts occurs owing to their intrinsic instability under oxidation conditions. Due to the limited reconstruction degree, nitrides(or carbides)@reconstructed layer is usually formed. In this core–shell structure, the reconstructed layer acts as an active catalytic component, and pristine nitrides/carbides realize the effective electron transport of the bulk catalyst. Therefore, such catalysts usually have both high catalytic activity and excellent stability. However, Mullins et al. reported that the Co$_3$C nanoparticle catalyst with size of 20–30 nm could be completely reconstructed to amorphous CoO$_x$ under long-term oxidation conditions.[38] The authors attributed it to the formed porous nanostructure when the crystalline carbide evolved into amorphous oxide, which promoted the complete oxidation of Co$_3$C. The activity of this completely reconstructed catalyst was higher than that of the intermediate state (partially reconstructed one, i.e., Co$_3$C@CoO$_x$). Nevertheless, the relationship between the reconstruction degree of precatalysts and OER activity is still unclear, and further research is needed to determine whether surface or complete reconstruction is better.

MOFs: MOF materials are the crystalline network compound with metal center as junction, and organic bridging ligands self-assembling through coordination bond. It has gradually attracted attention in OER catalysis due to large surface area, adjustable pore size, and diverse metal junctions. Mai and others summarized the synthesis and application of MOF materials.[145,146] MOFs are usually calcined to the corresponding derivatives in electrocatalytic applications.[147] When MOFs are directly applied for OER, the oxidative reconstruction phenomenon caused by ligand missing will occur.[73–76] For example, Lee et al. detailedly analyzed microstructure/phase evolution in strong alkaline OER based on Co ZIF-67 precatalyst, which finally evolved into CoOOH/Co(OH)$_2$ catalytic

active species.[36] Some MOF materials are very stable, such as [Co$_2$(μ-OH)$_2$(bbta)][148] and Fe$_2$Ni-BPTC,[149] in which no obvious reconstruction phenomenon has been found in OER. The metal sites in these catalysts are regarded as active sites.

PBAs: PBAs have the characteristics of simple synthesis, low cost, and adjustable molecular framework structure, and their molecular formula is A$_x$B[M(CN)$_6$]·nH$_2$O (A: alkali metal ion; B: Fe, Co, Ni, Zn, Mn, etc.; M: Fe, Mn, Co). Recently, Dou et al. detailedly introduced the chemical structure properties, synthesis methods and applications of PBAs in the fields of batteries and catalysis.[150] These materials will be reconstructed in OER, and the reconstructed species are commonly the corresponding hydroxides and oxyhydroxides.[77–79,81] For example, Zhang et al. achieved a complete reconstruction of Na$_x$CoFe(CN)$_6$ to CoOOH using an electrochemical oxidation strategy.[80] Yu et al. found that CN$^-$ vacancies could inhibit iron immersion in PBAs to obtain highly active NiFeOOH reconstruction layer.[77] Similar to MOF materials, due to the poor conductivity of Prussian blue materials, carbon-based derivatives are also usually obtained and applied in energy storage and conversion.[151]

Hydrates: Obviously, PBAs and some MOF materials contain crystal water. Currently, there are few reports on other types of materials containing crystal water that have been directly used in OER catalysis. Driess et al. studied the alkaline OER application of ACo(H$_2$O)$_2$[BP$_2$O$_8$]·H$_2$O (A is Li or Na) and found that an amorphous Co(OH)$_2$/CoOOH was formed on the surface.[82] The authors considered that the crystal water in this material played a role in promoting the diffusion of solution and ions. However, it was not discussed in depth whether the crystal water had an effect on reconstruction of catalyst or not. Our group recently reported the complete reconstruction phenomenon of hydrated nickel molybdate in alkaline OER, in which the (oxy)hydroxide with ultrasmall nanoparticle-interconnected structure was finally formed.[25] It was found that the leaching of crystal water made the reconstruction layer loose and porous, which accelerated the topological/chemical reconstruction process and deepened the reconstruction degree. For other crystal water containing compounds, such as CoMoO$_4$·0.75H$_2$O and Co(CO$_3$)$_{0.5}$(OH)·0.11H$_2$O, the complete reconstruction phenomenon also occurs in alkaline OER. Nevertheless, the influence of crystal water on the occurrence of reconstruction process and OER activity needs to be further explored.

Others: Besides the materials mentioned above, there are other types of oxygen evolution catalysts that also involve reconstruction phenomenon, including fluorides,[83] hydroxyfluorides/chlorides,[26,33] phosphosulfides,[84] and other coordination compounds.[85] For example, Dai et al. used high-entropy perovskite fluoride for efficient oxygen evolution catalysis and found that oxides or hydroxides were formed after OER.[83] Hu et al. found that F in the hydroxyfluoride leached out and induced the surface reconstruction of catalyst when OER occurred, forming a highly active mesoporous amorphous NiFe oxyhydroxide layer.[26]

3.2.2. Precatalysts for Acidic OER

At present, alkaline water electrolysis has been implemented for small and medium-sized industrial applications. Compared

**ADVANCED
SCIENCE NEWS**

www.advancedsciencenews.com

**ADVANCED
MATERIALS**

www.advmat.de

Table 2. Summary for reconstruction-involved precious metal-based precatalysts in OER, reconstructed species and their applied characterizations. * means that the testing temperatures have not been mentioned. RT means the room temperature.

Precatalysts	Electrolytes (temperatures)	Reconstructed species	Applied characterizations	Ref
Lithium-intercalated $IrSe_2$	0.5 M H_2SO_4*	Ir oxides with poor crystallinity ($\approx$7 nm)	Ex situ HRTEM, HAADF-STEM/EELS, XPS	[45]
$IrSe_2$		Amorphous Ir oxides ($\approx$1 nm)	Ex situ HRTEM, XPS	
$SrCo_{0.9}Ir_{0.1}O_{3-\delta}$	0.1 M $HClO_4$ (RT)	Amorphous IrO_xH_y ($\approx$10 nm)	Ex situ HRTEM, XPS	[44]
$RuIrZnO_x$	O_2 saturated 1 M KOH* (RT)	Low-crystalline $RuIrO_x$	Operando XAS; Ex situ HRTEM, XPS	[152]
Lithium-intercalated IrO_2	0.5 M H_2SO_4*	Amorphous oxidized iridium	Operando XAS; Ex situ XPS, HAADF-STEM	[153]
$IrNi_{3.2}$	N_2-saturated 0.05 M H_2SO_4	IrO_x (forming $IrNi@IrO_x$ core–shell structure)	Operando XAS; Ex situ resonant high-energy XRD	[154]
$Sr_2MIr^{(V)}O_6$ (M = Fe, Co) and $Sr_2Fe_{0.5}Ir_{0.5}^{(V)}O_4$	0.1 M $HClO_4$	IrO_x	Ex situ XAS	[155]

with the alkaline electrolyzer, the acid electrolyzer based on proton exchange membrane (PEM) receives much attention due to the advantages of higher ionic conductivity of electrolyte, low cost, effective control of gas penetration, and large output current. Currently, the acid electrolyzer has not realized industrialization application, and the main bottleneck for its development lies in the shortage of highly active, stable and corrosion-resistant catalysts during long-term OER operation. The researches on acidic OER catalysts mainly concentrate on the precious metal catalysts (**Table 2**),[156–158] and a few other works are based on nonprecious metal catalysts such as MnO_x, lead oxides, strontium titanate, and polyoxometalates.[159–162] It raises an issue whether the reconstruction exists or not for catalysts under acidic conditions, and this will promote the rational design of high-efficiency and acid-stable OER catalysts. In fact, the surface oxidation of iridium oxide films during oxygen evolution has been confirmed by ex situ XPS study as early as 1990.[163] Recently, Jaramillo et al. discovered the Sr-leaching of IrO_x/$SrIrO_3$ catalyst after OER, and the IrO_3 or IrO_2 formed on the surface.[164] A similar phenomenon also exists in $SrCo_{0.9}Ir_{0.1}O_{3-\delta}$ catalyst, with leaching of Sr–Co species and formation of Ir oxides.[44] The authors thought that the Sr–Co leaching was attributed to their thermodynamic instability under strongly acidic condition. Lithiation engineering is an effective strategy to improve the catalytic activity,[165] and has been applied in reconstruction-involved precious metal-based OER catalysts. Zeng et al. confirmed the formation of 7 nm thick amorphous oxide layer on the lithiated $IrSe_2$ after acidic OER catalysis.[45] This thickness value was much higher than that of $IrSe_2$ without lithiation treatment ($\approx$1 nm). In terms of reconstruction-involved nonprecious metal-based OER catalysts, such as $CoFePbO_x$, was demonstrated the leaching of Co, Pb, and Fe species and the formation of highly disordered mixed metal oxides by Simonov group.[161] The formed species guaranteed its stable OER catalysis at industrially relevant temperatures under strongly acidic conditions. Some works reported the acid-stable nonprecious metal-based OER catalysis without reconstruction phenomenon, such as amorphous noble metal nanosheets,[158] cobalt-containing polyoxometalates[160] and strontium titanates.[159] Taking amorphous Ir nanosheets applied in O_2-saturated 0.1 M $HClO_4$ solution as an example, the decreased bond length of Ir–C/O while the applied potential increased from 1.16 to 1.48 V versus RHE was confirmed by in situ EXAFS measurements.[158] This was due to the formation

of intermediate species or O_2 molecule on catalyst surface. In spite of this, the distance of Ir–C/O and the valence state of Ir could be restored to its pristine state when back to the initial potential. These results suggest the high component stability of amorphous Ir catalysts.

3.2.3. Precatalysts for Neutral OER

Neutral electrolyte generally adopts buffer or salt solution,[166] exhibiting the nature of environmental friendliness. A main challenge is that rare catalysts can perform excellent OER performance in a neutral medium at room temperature. It is required to consider whether the catalyst reconstruction occurs and to study real catalytic species, which is the same as those in alkaline/acidic OER catalysis. Researches on neutral OER catalyst mainly concentrate on the borates/phosphates,[119,167,168] and a small amount in phosphides,[169] coordination compounds,[170] and precious metal-based materials.[45] Some studies have reported the reconstruction phenomenon, for example, Cao et al. studied the evolution of $Co_3(PO_4)_2 \cdot 8H_2O$ and $Co_3(PO_4)_2$ under neutral OER conditions.[119] Based on in situ Raman and in situ XAS characterizations, both catalysts occurred surface reconstruction and formed high-valence cobalt (oxy)hydroxides, which were considered as real catalytic species. Compared with electrochemical treatment in neutral media, it is easier to achieve the breakage of Co—Co bond and promote active species generation of phosphides in harsh alkaline media. Using this feature, Xie and co-workers firstly carried out electrochemical activation via alkaline OER treatments, and such an operation achieved larger thickness of reconstruction layer of Co_2P after neutral OER than that without activation in alkaline OER. This activation treatment endowed the reconstructed catalysts with more active species and thus enhanced neutral OER performance. This work reflects that the researches on real active species have enlightenment role for the rational design of high-efficiency OER catalysts. There are also some literature reports that the catalysts can achieve stable catalysis for neutral OER and the material itself does not change, such as $Mn_3(PO_4)_2 \cdot 3H_2O$.[120]

In summary, the reconstruction phenomenon of nonprecious metal-based catalysts in OER and their intrinsic catalytic mechanism have attracted wide attention; particularly, it is found that the leaching of certain species in the bulk phase happens in majority precatalysts. Therefore, such precatalysts and those

**ADVANCED
SCIENCE NEWS**
www.advancedsciencenews.com

**ADVANCED
MATERIALS**
www.advmat.de

contain elements that are thermodynamically unstable in electrolyte should be paid special attention to whether there exists reconstruction phenomenon during their catalytic process.

3.3. Origins of Limited Reconstruction

Most of the currently reported OER precatalysts are featured by limited reconstruction degree and remain some original components. Limited reconstruction mechanism is rarely involved in previous works and deserves further research. The reasons for the limited reconstruction are summarily attributed to in situ formation of dense reconstruction layer, limited electron/ion transport, or ion leaching induced electronic structure modulation. For example, our group confirmed the in situ formed dense (oxy)hydroxide layer on the $NiMoO_4$ surface.[24,25] It suppressed the solution penetration and resulted in limited mass transport, which made the reconstruction process terminated soon and prevented inner parts against further oxidation. Hu et al. thought that the electrical and diffusional limitations were responsible for limited reconstruction of fluoride-incorporating NiFe hydroxide.[26] Xu et al. unraveled the self-termination behavior on $CoFe_{0.25}Al_{1.75}O_4$, which was caused by Al^{3+} leaching induced lattice oxygen oxidation and prevented further reconstruction.[40] In fact, from a thermodynamic point of view, the precatalysts could eventually convert unless there exist structural or kinetic barriers, which are the main factors for the blocked reconstruction processes. Therefore, the test condition and properties of reconstruction layer can greatly affect the reconstruction degree, and the origin of limited reconstruction for a precatalyst should depend on specific circumstances.

3.4. Strategies for Complete Reconstruction

Due to the surface-catalysis property, deepened reconstruction of precatalysts would promote the formation of active species and improve the component utilization. In this section, we will disclose and expound the effect factors on the reconstruction degree and promotion mechanism from three critical aspects of material self-instability, structural modulation, and extreme test condition.

3.4.1. Self-Instability of Precatalysts

Cation/Anion Leaching: The cation-leaching involved OER precatalysts mainly include Li/Na/K-containing layered battery materials. The gradual dissolution of alkali metal ions within these materials into solution generally occurs with oxidation reactions. Li et al. uncovered the spontaneous Li-extraction of spinel $Li_2Co_2O_4$ upon the electrochemical condition (**Figure 7**a), generating amorphous reconstruction layer of $Li_{2-x}Co_2O_{4-\delta}(OH)_\delta$ (Co^{3+}/Co^{4+}).[39] After CV activation, the Li/Co ratio gradually decreased with increasing cycle numbers. Beyond $Li_2Co_2O_4$, $LiCoO_2$ and $LiCoPO_4$ have also been confirmed with chemical reconstruction phenomenon during OER,[101] and we guess that the leaching of Li results in the reconstruction and forming a low-crystalline layer. This

spontaneous Li-extraction behavior could greatly enhance OER activity. Similarly, Cui et al. ingeniously adopted an electrochemical control method to achieve preextraction of lithium before OER testing.[172] This pretreatment resulted in a more desirable electronic structure to trigger the catalytic reaction. The above-mentioned results show that the cation leaching can promote reconstruction occurrence and performance improvement for Li/Na/K layered material catalysts.

Anion leaching can also promote the reconstruction process. For example, Hu et al. demonstrated the F^- leaching of fluoride-incorporating NiFe hydroxide during OER. The original surface layer was transformed into amorphous NiFe oxide layer, and the thickness of this layer reached 35 nm.[26] This value is much larger than those of many reported catalysts of below 10 nm, which may be attributed to the sponge-like structure formed by the leaching of fluoride ions. Therefore, the anion leaching and reconstruction would probably exist in these F, Cl, P, and S-containing precatalysts, such as $Co_2(OH)_3Cl$[33] and $Ni_{0.9}Fe_{0.1}PS_3$.[84] In particular, in terms of phosphides, nitrides, and carbides, they can also reconstruct and form the corresponding (hydr)oxides or (oxy)hydroxides. For example, Co_3C precatalysts could reconstruct into CoO_x due to its self-instability,[38] but the forms of P, N, and C in the solution are not clear enough, and we suspect that these species exist in the forms of nitrate, phosphate, and carbonate ions. Guo et al. recently confirmed the potential-driven self-reconstruction phenomenon of Ag/CoFe amorphous nanosheets (Ag/CoFe-AN).[23] During its evolution, the cations dissolution triggered by the oxidation of lattice oxygen promoted the subsequent redeposition of leaching cations, which was beneficial to the formation of dispersed Ag atoms on the cobalt-iron (oxy)hydroxide layer. Very recently, Li et al. reported the fluorination method to achieve the obviously deepened reconstruction degree of NiFe based OER precatalyst (Figure 7b).[27] The leaching of F species played an important role in such promoted reconstruction process, which guaranteed the formation of desired defective Ni(Fe)O_xH_y shell and thus resulted in much enhanced OER activity.

In addition, the coleaching of cation and anion will further deepen the reconstruction degree, and the related catalysts mainly focus on coordination compounds, such as Prussian blue[78] and MOF materials.[36,173] For example, Yu et al. found the $[Fe(CN)_6]^{4-}$ leaching of $K_2NiFe(CN)_6$ during OER, which made the surface self-reconstruction of NiO(OH) layer.[77] This leaching may be attributed to that the PBA is unstable and can decompose in this strong alkaline solution.[78,174] Zhang et al. found that the $Na_xCoFe(CN)_6$ precursor transformed into ultrathin CoOOH nanosheets realized by electric-field driven decomposition and self-assembly (Figure 7c), during which the leaching of iron ions and CN^- played a key role in this process.[80] Hence, in order to get a catalyst with high reconstruction degree, designing a precatalyst which can operate the multicomponent leaching during electrochemical oxidation will be an effective strategy.

Cation/Anion Vacancy: Song et al. demonstrated that the nickel vacancy in $Ni(OH)_2$ could generate more true active components, which was due to the decreased formation energies of active species via theoretical analyses (Figure 7d).[171] In terms of anion vacancy, such as CN^- vacancy in $K_2NiFe(CN)_6$, its promoted reconstruction phenomenon has not been
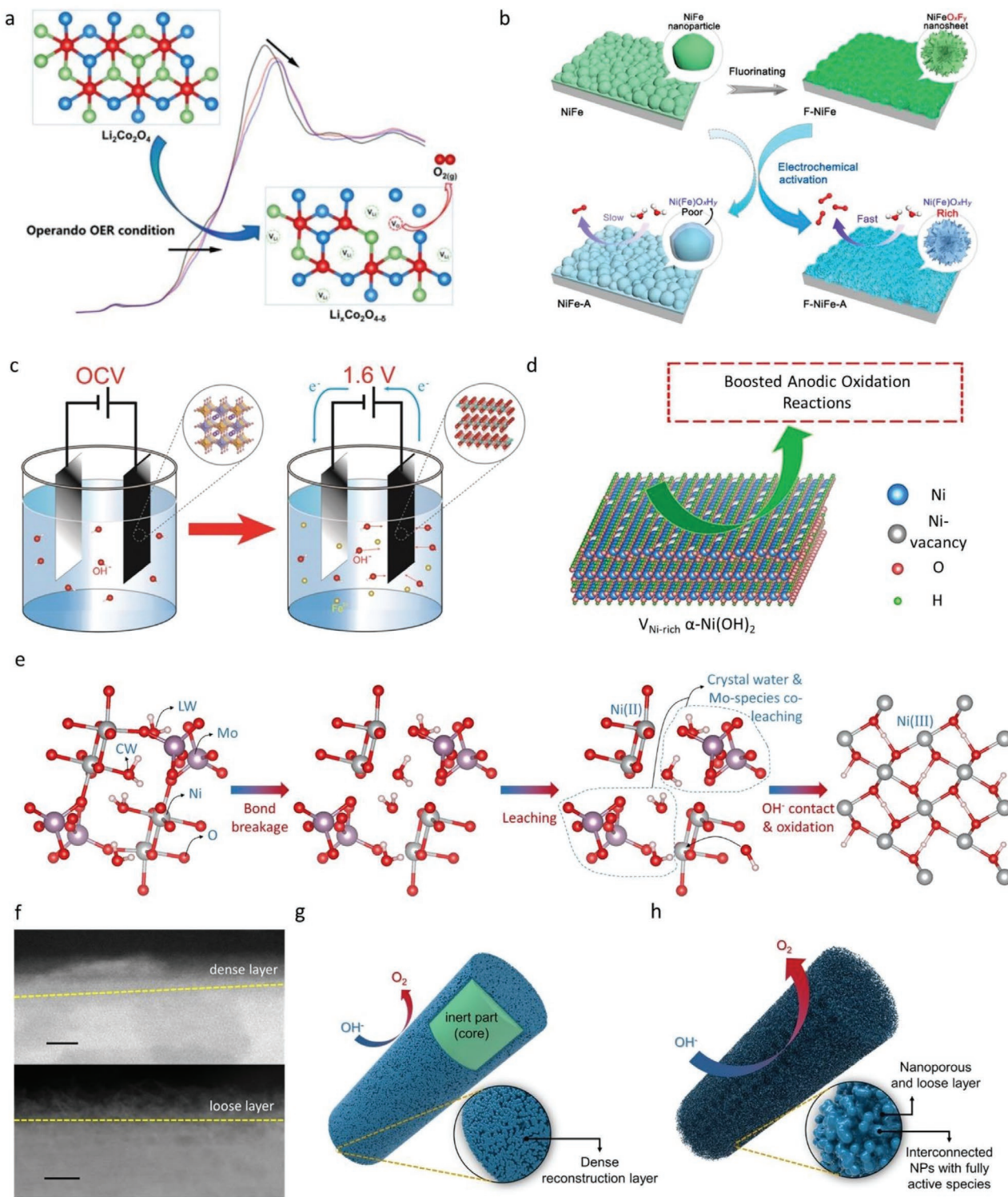
Figure 7. a) Co K-edge X-ray absorption near edge structure (XANES) of $Li_2Co_2O_4$ with open circuit voltage (OCV) and at 1.60 V versus RHE after 20 and 60 min in 1 M KOH. The inset shows the corresponding structural evolution during OER. Reproduced with permission.[39] Copyright 2019, American Chemical Society. b) Illustration of fluorination-deepened reconstruction degree of Ni–Fe based OER precatalyst. Reproduced with permission.[27] Copyright 2020, American Chemical Society. c) In situ electrochemical fabrication of CoOOH nanosheets from $Na_xCoFe(CN)_6$. Reproduced with permission.[80] Copyright 2019, Royal Society of Chemistry. d) Schematic diagram of nickel vacancy in α-Ni(OH)$_2$ for enhanced OER catalysis. Reproduced with permission.[17] Copyright 2018, American Chemical Society. e) Dynamic reconstruction processes from $NiMoO_4 \cdot xH_2O$ to NiOOH. f) HAADF STEM images of $NiMoO_4$ (upper) and $NiMoO_4 \cdot xH_2O$ (lower) after soaking in KOH solution, scale bars: 2 and 10 nm. g,h) Schematic diagram for the two reconstruction results of $NiMoO_4$ and $NiMoO_4 \cdot xH_2O$, respectively. e–h) Reproduced with permission.[25] Copyright 2020, Elsevier.

**ADVANCED
SCIENCE NEWS**

www.advancedsciencenews.com

**ADVANCED
MATERIALS**

www.advmat.de

mentioned.[77] However, such a vacancy has been reported to suppress the release of Fe species and thus favor the formation of active (oxy)hydroxide species. Vacancy engineering is also a kind of defect engineering, which should have positive effects on the reconstruction processes and formation of active species. Nevertheless, the relationship between vacancy and reconstruction degree remains to be further explored.

Multicomponent Coleaching: This phenomenon frequently occurs in crystal water containing materials, which mainly focus on some hydrated molybdates, PBAs or MOF materials. During OER, the crystal water molecules and molybdate ions or ligands generally co-leach, causing irreversible phase transition and thus reconstruction. For example, we systematically investigated the electro-oxidation mechanism of hydrated nickel molybdenum precatalysts recently (Figure 7e).[25] The existence of crystal water within precatalysts and co-leaching of molybdate ion and crystal water was the key points for the rapid occurrence of reconstruction. In more detail, due to the coleaching of molybdate ion and crystal water of $NiMoO_4 \cdot xH_2O$ during alkali etching, its surface became loose and porous, but the dense reconstruction layer formed on the surface of $NiMoO_4$ (Figure 7f). The porous layer is conducive to the deep penetration of electrolyte, which can then initiate the chain reconstruction process under electrochemical conditions until the complete reconstruction occurs. Finally, two different reconstruction results occurred as schematically displayed (Figure 7g,h). In addition, from structural features, it is easy to conclude that the porosity and specific surface area of completely reconstructed catalysts is usually higher than that of surface reconstructed catalysts. However, it is difficult to obtain Brunauer–Emmett–Teller (BET) data of catalysts before and after reconstruction, because it is not easy to obtain a large amount powders by electrochemical reconstruction method to meet BET test requirement. Therefore, it is worthwhile and challenging to study the change of porosity before and after reconstruction and its effect on the catalytic performance.

3.4.2. Structural Modulation

Crystallinity: The phase reconstruction is generally accompanied by the breaking and formation of bonds, thus the precatalysts with less crystallinity would be more prone to electro-oxidation and evolution. Yu et al. reported a facile supersaturated coprecipitation method for the scalable synthesis of amorphous NiFeMo oxide, which undergone a rapid self-reconstruction process at applied oxidized potentials and the oxy(hydroxide) surface layer formed with rich O-vacancies.[100] However, the high diffusion barrier of Mo cations in crystalline NiFeMo material limited the penetration of solution, which caused the suppressed reconstruction. This work gave insights into why amorphous materials outperform crystalline ones in OER catalysis. Liu et al. also confirmed that the higher OER activity of crystalline NiFe alloy.[175] Combined with in situ XAS and isotope labeling analyses, the enhanced OER catalysis was attributed to the amorphous structure which could be electrochemically activated to catalytic active sites in the bulk materials (**Figure 8**a). In this work, we think that the easier

reconstruction process of amorphous structure is also one of the reasons for its improved performance.

Catalyst Size: The thicknesses of reconstruction layer for many surface reconstruction catalysts are within 10 nm,[17,24,40,41,43,56,58,62] and some typical examples have also been summarized in our recent work.[25] Therefore, reducing one dimension of precatalysts to less than 10 nm may realize the deep reconstruction till complete, such as ultrasmall nanoparticles, ultrathin nanosheets and ultrafine nanowires. Our recent work supported this notion, and the lithiation strategy was introduced to reduce the size of NiO to less than 10 nm (Figure 8b).[29] After removing the soluble Li_2O species, the ultrasmall particle-interconnected structure was formed, and finally the deep reconstruction was achieved during OER to acquire high-mass-activity catalysis. The obtained catalysts with deep reconstruction possess the identified active species and are featured by unique structure, such as small particle-interconnected structure, low crystallinity, and abundant defects. These characteristics endow the catalysts with high mass activity and durability. In terms of its inverse process, i.e., delithiation reaction, the current research has yet to study whether it can reduce the size of catalyst, but the surface of delithiated one can effectively form (oxy)hydroxides and improve the oxygen evolution activity of reconstructed catalysts (Figure 8c,d).[28] Under the oxidized potentials, the ultrathin cobalt hydroxide nanosheets would be completely reconstructed to the corresponding (oxy)hydroxide (Figure 8e).[176] In this ultrathin structure, the material crystallinity is commonly poor with many disordered regions, which may also cause the rapid reconstruction. Here is another typical example that small size facilitates complete reconstruction of precatalyst. Zou et al. fabricated 20 nm thick Ni_3S_2 nanosheets anchored with many monodispersed $Ni_xCo_{3-x}S_4$ nanoparticles with 3–5 nm in size.[177] After OER testing, these ultrasmall nanoparticles totally transformed into hydroxides but the underlying crystalline nanosheets kept unchanged.

Structural Activation: Activating reconstruction via ion substitution serves as an effective method. Xu et al. fabricated iron-substituted $CoAl_2O_4$ precatalyst, which promoted its reconstruction during alkali OER (Figure 8f).[40] This substitution strategy optimizes the electronic structure of inert spinel oxides and realizes the surface-controlled electrochemical reconstruction. In the La_2NiMnO_6 perovskite material, the superexchange interaction induced strong Jahn–Teller distortion, which could also promote the formation of active species.[56]

3.4.3. Extreme Test Condition

Test Duration: The durability of catalysts is one of the most important parameters in performance evaluation, and is directly related to the testing time. As for the reconstruction-involved precatalysts, the research on the composite evolution after a long-duration test is of great importance to the analyses on the catalytic structure and intrinsic catalytic mechanisms at stable stage. Qiu et al. found the gradually increased electrochemical activity of the $Co_{0.8}Fe_{0.2}P@C$ as the electrochemical oxidation goes on (**Figure 9**a).[178] During such a process, the $Co_{0.8}Fe_{0.2}P$ was completely reconstructed to $Co_{0.8}Fe_{0.2}OOH$ when the electrochemical oxidation time reached 90 min. As
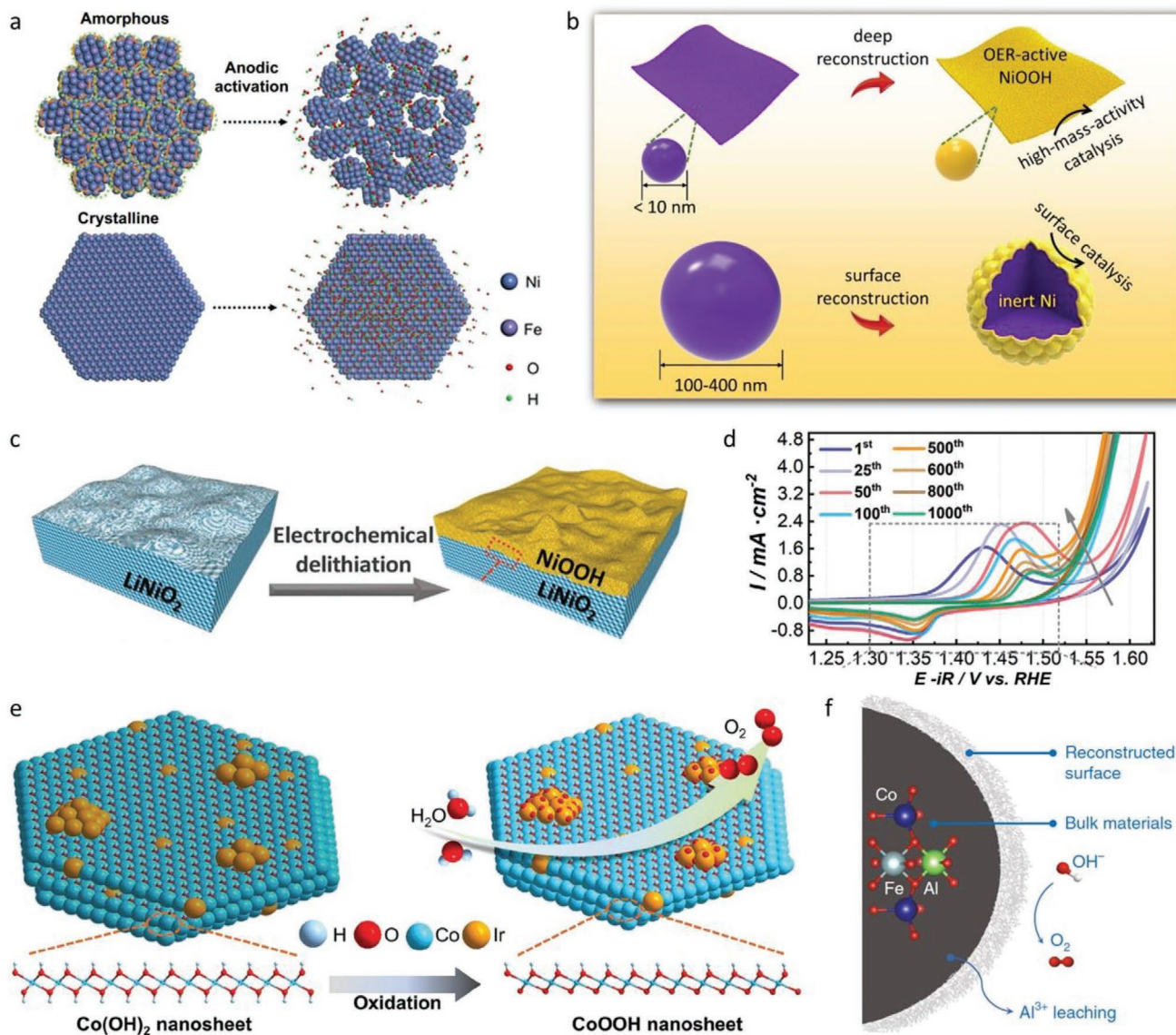
Figure 8. a) Schematic illustration for the electrochemical activation of the amorphous and crystalline catalysts. Reproduced with permission.[175] Copyright 2020, American Chemical Society. b) Schematic diagram of reconstruction results for the sub-10 nm nanoparticle-assembled Ni nanosheet and bulk Ni particle. Reproduced with permission.[29] Copyright 2019, American Chemical Society. c) Schematic diagram of electrochemical delithiation of $LiNiO_2$ precatalyst, forming delithiated-$LiNiO_2$/NiOOH heterojunction. d) CV cycles at 10 mV s^{-1} in O_2-saturated 1 M KOH (99.999%) of $LiNiO_2$ precatalyst during electrochemical delithiation. c,d) Reproduced with permission.[28] Copyright 2020, Wiley-VCH. e) Mechanism diagram of OER on the CoIr-based catalyst surface and the transformation of α-Co(OH)$_2$ to β-CoOOH phase. Reproduced with permission.[176] Copyright 2018, Wiley-VCH. f) Schematic diagram of Al^{3+} leaching along with surface reconstruction of iron-substituted $CoAl_2O_4$. Reproduced with permission.[40] Copyright 2019, Springer Nature.

shown in Figure 9b, the leaching of phosphorus species was complete according to the XPS results, further confirming the above-mentioned complete reconstruction phenomenon. Xie et al. found that the degree of surface reconstruction for La_2NiMnO_6 deepens with the increase of CV numbers during its electrochemical cycles.[56] The thickness of the reconstruction layer increases from 0 to 5–8 nm, which means that the electro-oxidation time is one of the factors that affect the reconstruction degree. Insufficient testing time will probably make an inaccurate catalytic structure. For instance, the core–shell $Co_3C@CoO_x$ structure was obtained in a short test time but it

transformed into amorphous CoO_x after a long enough oxidation test.[38] This phenomenon has been reported in other-type precatalysts.[41] Therefore, when considering the stable catalytic states of catalysts, it is vital to analyze structure after a long enough period of testing.

Operation Temperature: Operating temperature during catalysis affects the real active components of the catalyst. For example, Zhang et al. confirmed temperature-regulated reversible transformation of spinel-to-oxyhydroxide active species for OER.[179] At 25 °C, the $NiCo_2O_4$ served as OER-active species, but it evolved to Ni(Co)OOH when carried out at 45 °C.
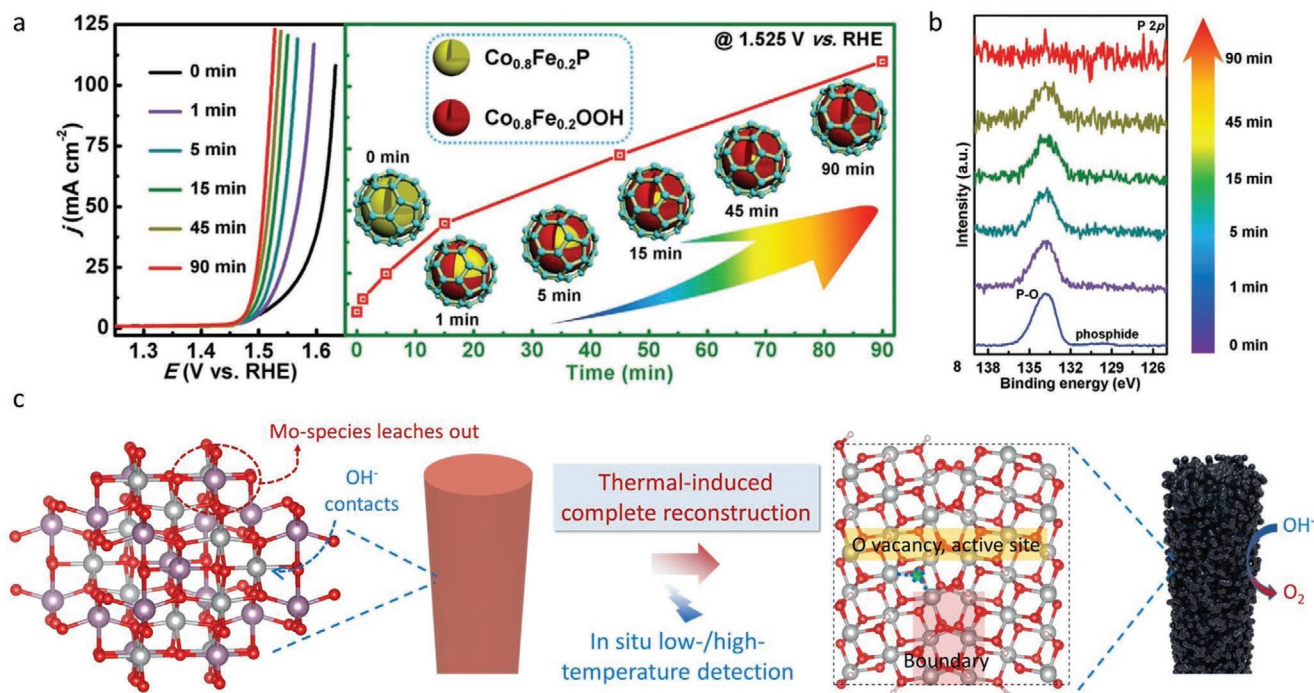
**ADVANCED
SCIENCE NEWS**

www.advancedsciencenews.com

**ADVANCED
MATERIALS**

www.advmat.de

Figure 9. a) LSV curves of $Co_{0.8}Fe_{0.2}P@C$ after different electrochemical oxidation time and corresponding current densities @1.525 V versus RHE. Inset: schematic illustration for the structural reconstruction of $Co_{0.8}Fe_{0.2}P@C$. b) P 2p XPS spectra of $Co_{0.8}Fe_{0.2}P@C$ after different treatment time. a,b) Reproduced with permission.[178] Copyright 2020, Wiley-VCH. c) Schematic diagram for the thermal-induced complete reconstruction on $NiMoO_4$ nanowire precatalyst, forming NiOOH nanoparticle-interconnected structure with abundant vacancies and boundaries. Reproduced with permission.[24] Copyright 2020, Wiley-VCH.

It can be noticed that the OER mechanism analysis and performance evaluation of the catalyst are mostly conducted at room temperature, while the industrial temperature of water electrolysis is 50–80 °C.[180] The precatalysts with surface reconstruction are mainly restricted by mass transfer process, and it can be accelerated at industrial high temperatures and thus deepened reconstruction process. Based on this principle, we put forward a thermal-induced complete reconstruction strategy (Figure 9c).[24] The leaching of Mo species and deep penetration of solution were promoted at high temperatures. Therefore, the precatalysts with surface reconstruction at room temperature can be completely reconstructed at high temperature of 51.9 °C. These results show the influence of temperature on the reconstruction degree. Very recently, Masa et al. probed the chemical stability of Ni_yP precatalyst in 1 M KOH at 80 °C, its complete reconstruction phenomenon was also observed after prolonged aging time.[48] In many previous reports, the metal phosphide precatalysts commonly occur limited reconstruction degree at ambient temperature during OER.[17,37,58,111,181] It could be attributed to the sluggish P-leaching process and the formed dense reconstruction layer, which terminate the reconstruction process. At high temperature, the diffusion kinetics are accelerated and the solution could achieve deepened penetration. Therefore, the high temperature operation can serve as an efficient strategy to deepen the reconstruction degree till complete. In addition, Zhong et al. also evaluated the OER stability of sulfur-treated Fe-based MOFs at 50 °C.[182] Differently, the MOF structure was confirmed to be remained after 100 h operation. Even so,

only low-resolution TEM images were provided to support this conclusion, which could only display simple morphology information, and the component and microstructure information were lacking. With the recognition of catalyst reconstruction, the actual operating conditions should be considered when designing catalysts for industrial applications. However, investigating the properties of precatalysts and their reconstruction chemistry under industrial parameters is still in its infancy.

Solution Concentration: This is related to the pH of solution, which has been reported to have a significant effect on the activity of the catalyst, such as catalyst behavior, activity.[183–186] Strasser et al. studied in detail the effect of solution pH on Ni–Fe (oxy)hydroxide oxygen evolution catalyst.[183] They found that an earlier onset of the redox process in higher pH of solution. The higher pH of solution could effectively provide the local buffer capacity and prevent a drop in local pH, which could support the higher catalytic activity in higher pH of solution. Koper et al. demonstrated pH-sensitivity of NiOOH catalyst, which also showed better activity in higher pH of alkali.[184] Besides, the pH of solution could also affect the reconstruction degree, which is related to the component stability of the catalyst. For example, Han et al. developed Co–Fe PBA material, and could provide stable alkaline OER catalysis when pH was lower than 13.[174] If the pH of alkali is higher than 13, the (oxy)hydroxide derivative could be generated from PBA because it is unstable and would decompose at this condition. Therefore, if the electrochemical oxidation of this material is carried out at high concentration alkali, the reconstruction process could be promoted. In addition, similar to

testing temperature, most of the currently reported OER catalysts were evaluated in the low-concentration alkali (0.1–1 M KOH), different from the industrial 20–30 wt% KOH in water electrolysis applications. This gap may lead to different reconstruction results. For example, the complete reconstruction of anhydrous $NiMoO_4$ precatalyst under industrial conditions (20–30 wt% KOH) was observed, but the reconstruction was limited on the thin-layer surface when tested in 1 M KOH.[25] Hence, this observed phenomenon suggests that understanding the intrinsic catalytic mechanisms under realistic conditions is thus meaningful and necessary, especially for reconstruction-involved precatalysts.

In summary, the extreme test conditions, including long-term stability test, high temperature and high-concentration alkali solution, could lead to different reconstruction results when compared with that under conventional one. Therefore, considering catalytic mechanism and performance evaluation under the realistic operation conditions is of great significance to the development of catalyst industry.

4. Complete Reconstruction for Novel Material Synthesis and Other Electrocatalysis

4.1. Novel Material Synthesis

This mainly refers to precatalysts involved in acid/alkaline etching-assisted reconstruction. Actually, both chemical etching and electrochemical treatments (i.e., applying voltage bias) can achieve material evolution. Chemical etching has been applied to prepare various (semi-)hollow structure.[187,188] If etching and electrochemistry are combined, new structural materials are supposed to be fabricated. For example, Li et al. highlighted the important role of electrochemistry in the evolution of $RuIrZnO_x$ precatalyst.[152] They carried out electrochemical CV treatments within the oxidized potential range of OER catalysis, during which the $RuIrZnO_x$ hollow nanoboxes evolved into $RuIrO_x$ netcages (**Figure 10**a). The obtained $RuIrO_x$ was featured by highly porous and mech-like structure (Figure 10b). This structure is very unusual and rarely reported, and is distinctly
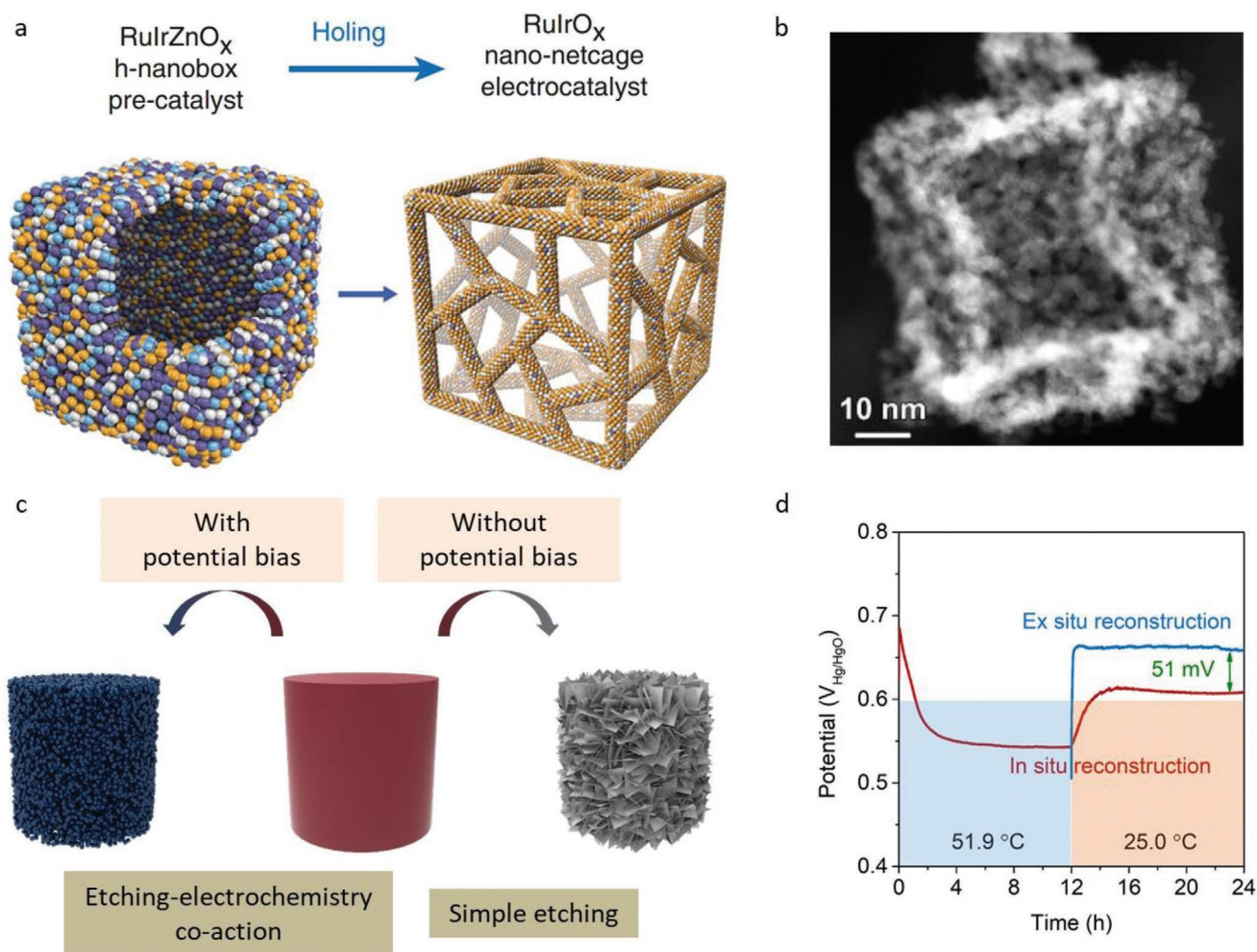
Figure 10. a) Schematic illustration from $RuIrZnO_x$ hollow nanoboxes to $RuIrO_x$ nanonetcage via electrochemical in situ etching. b) HAADF-STEM image of $RuIrO_x$ nanonetcage after in situ electrochemical etching. a,b) Reproduced with permission.[152] Copyright 2019, Springer Nature. c) Schematic diagram showing the effect of applied voltage bias on the reconstruction results of precatalysts. d) Chronopotentiometric results of $NiMoO_4$ precatalyst at 10 mA cm^{-2} in 1 M KOH. For in situ reconstruction, it was first measured at 51.9 °C and then at 25.0 °C. For ex situ reconstruction, it was first soaked in 1 M KOH at 51.9 °C and then electrochemically measured at 25.0 °C. Reproduced with permission.[24] Copyright 2020, Wiley-VCH.

**ADVANCED
SCIENCE NEWS**
www.advancedsciencenews.com

**ADVANCED
MATERIALS**
www.advmat.de

different from the architectures of nanoboxes and nanoframes. However, if the RuIrZnO$_x$ was immersed in an acidic or alkaline solution, only etching reaction took place and it resulted in smooth surface rather than porous one. In addition to new microstructure, the etching-electrochemistry also results in differences in the composition of the reconstructed catalysts. During the CV tests of RuIrZnO$_x$, the etching reaction existed simultaneously. The etching-electrochemistry co-action could thoroughly remove the Zn component of RuIrZnO$_x$, but simple etching treatment could not. The etching-electrochemistry engineering for new structural materials is also highlighted in our recent work.[24] We discovered different etching results of NiMoO$_4$ precatalyst with or without voltage bias (Figure 10c). With applied potential bias, the NiMoO$_4$ nanowires could transform into ultrasmall nanoparticle-interconnected (oxy)hydroxide nanowire structure (this process was called in situ reconstruction). If the potential bias was not applied, the nanosheet-assembled hydroxide nanowires were obtained and this process (this process was called ex situ reconstruction). More importantly, the catalyst after in situ reconstruction possessed obviously decreased overpotentials when compared to that of ex situ one (Figure 10d). In summary, in situ reconstruction via etching-electrochemistry engineering is a new pathway for fabricating new structural materials with unique phase-/microstructure, which have potential applications in diverse fields such as catalysis and batteries.

Moreover, as mentioned above, the reconstruction involves in situ deposition processes in which the components of the reconstructed species are derived from precatalysts. If these components come from test solution, such a "complete reconstruction"-like catalyst could also be obtained. For example, Chatti et al. skillfully electrodeposited oxides on fluorine-doped tin oxide electrode using aqueous H$_2$SO$_4$ which contained dissolved cobalt, lead, and iron.[161] During electrooxidation of acidic water, the highly disordered CoFePbO$_x$ layer was in situ generated, which served as highly stable OER catalyst in acid and could be operated at temperatures up to 80 °C. This work suggests that catalysts in situ prepared under harsh conditions are likely to exhibit excellent catalytic stability under these conditions.

4.2. Hydrogen Evolution Reaction

HER is the two-electron half-reaction of water electrolysis, which converts the intermitter electrical power into hydrogen energy. Very recently, the reconstruction phenomenon of HER catalysts was also discovered.[68,82,189,190] For example, Gao et al. studied the surface reconstruction of Mo$_2$C–MoO$_x$ and achieved enhanced HER in 1 M HClO$_4$.[189] As illustrated in **Figure 11**a, the authors obtained Mo$_2$C–MoO$_x$ via oxygen plasma, and identified its structural alteration of surface oxides from Mo (VI) to Mo (IV) which was clearly confirmed via in situ Raman spectra. The phenomenon that the newly generated species promote HER also existed in W$_2$C–WO$_x$. Another representative example was reported by Zheng group,[190] observing the complete convert from Ni-thiolate coordination polymer to metallic Ni with a small amount of surface sulfide (Figure 11b,c). Ni^0 served as the real catalytic species and the sulfide species could facilitate water dissociation by forming sulfide-hydrated cation networks. This reconstruction-induced activation phenomenon could be reflected during electrocatalytic testing, as the overpotential decreased with increasing cycling number (Figure 11d). Driess et al. uncovered that the surface reconstruction led to lattice vacancies and defects due to the loss of Li or Na in cobalt borophosphates during HER.[82] Interestingly, two components within heterostructured structure can electrochemically react during catalysis. Liu et al. discovered the formation of phosphides derived from CoFeO@ black phosphorus (BP) during HER catalysis (Figure 11e).[191] This phenomenon was due to the applied reduced potential, the metastability of amorphous cobalt iron oxide and its strong affinity with BP. The amorphous CoFe oxide with rich oxygen vacancies drives OER catalysis without forming CoFe–P component, but the strong affinity between BP and oxide guarantees long-term catalytic stability due to the suppressed dissolution of oxide into solution. Hence, these works inspire us to pay attention to the reconstruction phenomenon in HER catalysis. Besides, Noda et al. developed surface amorphized nickel hydroxy sulfide catalyst for high-efficient alkaline HER recently.[192] Interestingly, they first carried out the anodic potential cycling of NiS for anodic hydroxylation, which could also amorphized the surface. This electrochemical operation not only modified the chemical surface, but also enhanced charge transfer and HER kinetics. Therefore, the effect of reconstructed species on catalysts in other electrocatalysis is also worth studying, such as activity and stability.

4.3. CO$_2$ Reduction

Electrochemical conversion of carbon dioxide reduction reaction (CO$_2$RR) into fuels and chemical feedstocks such as carbon monoxide, formate, alcohols and hydrocarbon using renewable sources of electricity offers an effective pathway to settle energy crisis and close carbon loop.[198–200] Depending on the adsorption capacity of electrocatalysts to reaction intermediates and the number of electrons transferred, CO$_2$ can be reduced to different products, including CO,[201,202] formate,[203,204] methane,[205] methanol,[206] ethylene,[207,208] ethanol,[209] and so on. Generally, specific electrocatalysts are capable of specific product selectivity. Electrocatalysts such as Au,[210] Ag,[211] and single sites materials[212] bond *CO weakly and release CO as a major product, while Bi,[213] Sn,[214] and Pd-based[215] materials are more preferred for formate production. The multicarbon product (C2, C3) such as ethanol, ethylene and propyl alcohol release more easily on Cu-based materials which bind *CO strongly enough for realizing C–C coupling and the further reduction of *CO.[216–218] Due to the very negative potential to activate and reduce CO$_2$, the valence state of metal compounds cannot be maintained and the real catalytic role should be the metal. The transformation from compounds to elements, that is, the detachment of nonmetallic elements or the precipitation of metallic elements would lead to the reconstruction of the electrocatalysts, resulting in a change in morphology and surface coordination structure.[216] By reason of overall reduction, the reconstructed catalysts have not only surface defects but also bulk defects, and the resulted active sites bear a lower coordination number which have great influences on the adsorption behavior.
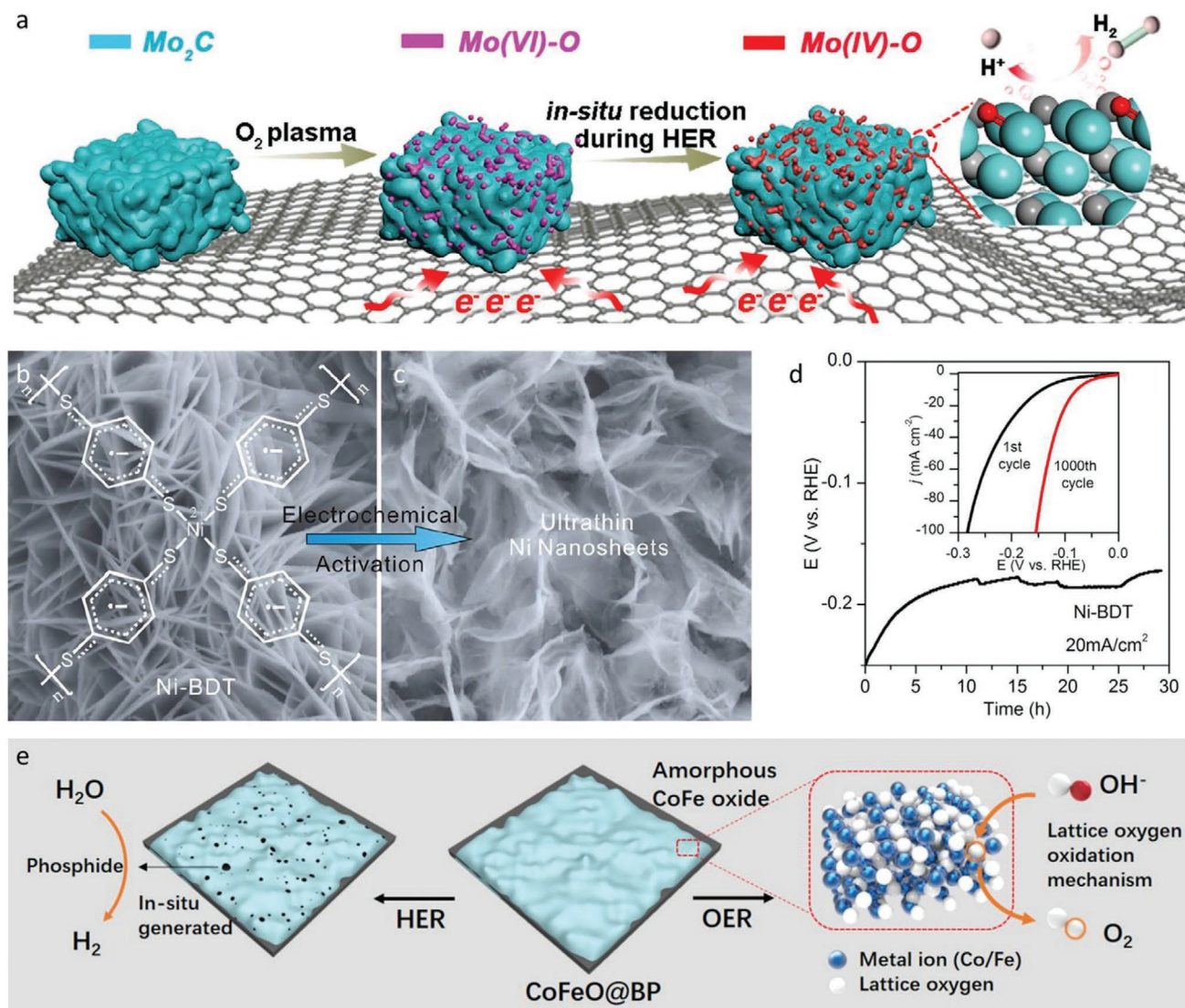
Figure 11. a) Illustration for the in situ reconstruction of $Mo_2C–MoO_x$ during HER catalysis. Reproduced with permission.[189] Copyright 2020, Wiley-VCH. b,c) SEM images of Ni-BDT (a coordination polymer using 1,4-benzenedithiol (BDT) as the ligand) and its derived Ni nanosheets via electrochemical activation, respectively. d) Chronopotentiometry at 20 mA cm^{-2} of Ni-BDT. The inset is the LSV curves of Ni-BDT at the 1st and 1000th cycles. b–d) Reproduced with permission.[190] Copyright 2017, Elsevier. e) Catalytic mechanism of amorphous CoFeO@BP catalyst for HER and OER. Reproduced with permission.[191] Copyright 2018, Elsevier.

Copper-based materials are the most typical and widely studied electrocatalysts in CO_2RR, and the only common electrocatalysts which can reduce CO_2 to multicarbon products. Multicarbon products are usually obtained by coupling two *CO intermediates and further reduction. To achieve C–C coupling, two adjacent active sites must be provided and the electrocatalysts with single sites like metalloporphyrin, metal phthalocyanine, and carbon-support single atoms only possess C1 product selectivity. Whereas, Cu^{2+} is not stable under negative potential and would be reduced to Cu^0, resulting in the structural transformation from single sites to clusters or nanoparticles (**Figure 12**a).[193] Wang et al. found that the copper(II) phthalocyanine (CuPc), copper(II) benzene-1,3,5-tricarboxylate (btc) MOF (HKUST-1), and copper(II) 1,4,8,11-tetraazacyclotetradecane chloride ([Cu(cyclam)]Cl$_2$) underwent a reconstruction from molecular to cluster under working conditions. It is worth noting that the metallic Cu cluster derived from CuPc with a size of ≈2 nm converted back to the original CuPc molecular on the retreat of negative potential, while HKUST-1 and [Cu(cyclam)]Cl$_2$ displayed an irreversibly transformation to form larger Cu nanoparticles and dendrites. Because of the strong interaction between Cu^{2+} and phthalocyanine molecular, as well as the much smaller cluster sizes, the release phthalocyanine molecular could be retained in the adjacency of Cu cluster, leading to more low-coordination surface sites which favor the CH_4 product. Moreover, Kim et al. reported that the Cu nanoparticles supported on the carbon paper agglomerated into ensembles under working conditions (Figure 12b–d), which controlled by the initial arrangements of Cu nanoparticles.[194] With high initial loading density, the consequent catalysts showed the enhanced C2,3 selectivity and C–C
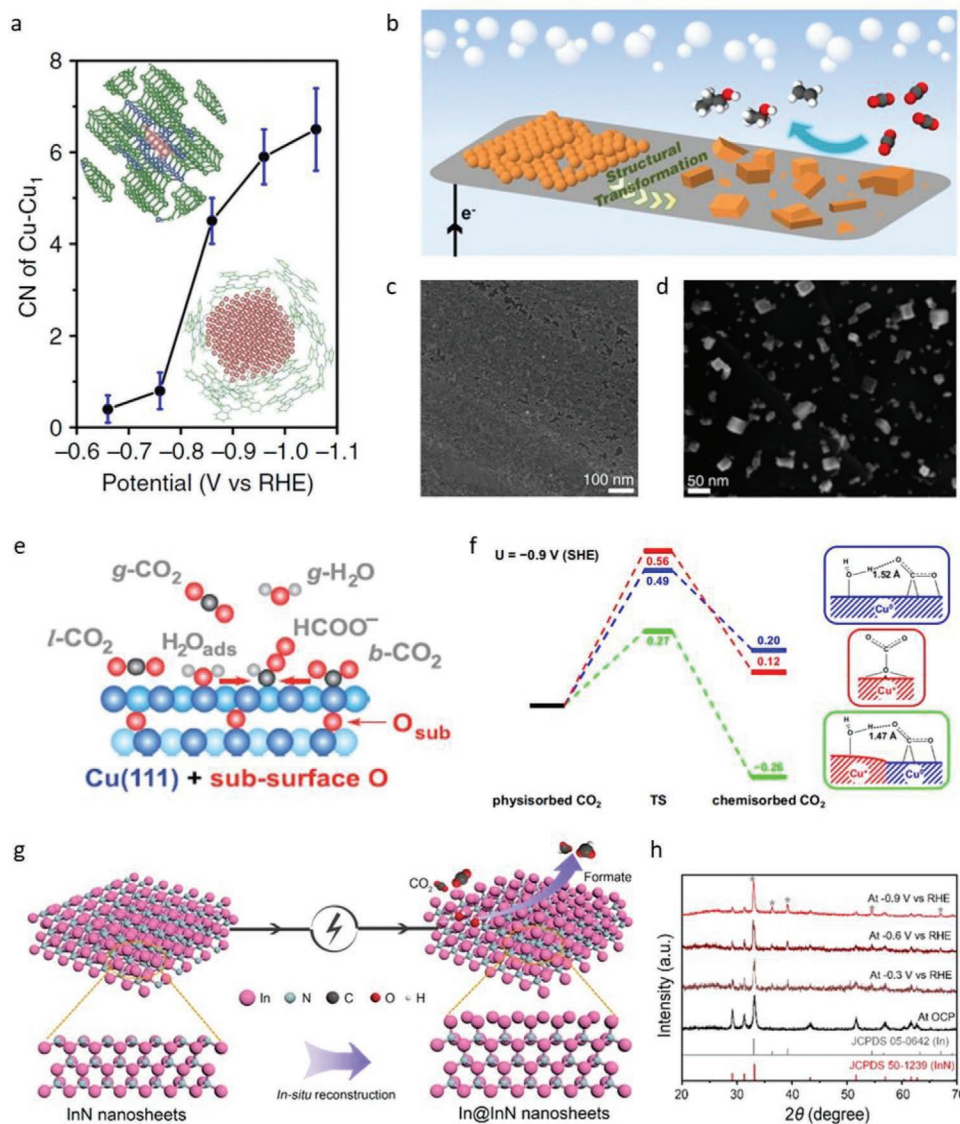
Figure 12. a) First-shell Cu–Cu CNs of the CuPc catalyst at different potentials. Reproduced with permission.[193] Copyright 2018, Springer Nature. b) Schematic illustrating the transformation process of Cu nanoparticles ensembles to an active catalyst for C2–C3 product formation. c) SEM images of Cu nanoparticles loaded on carbon-paper support at ×22.5 loading. d) SEM image of ×22.5 loaded carbon-paper support electrode after 7 min of electrolysis at −0.81 V versus RHE. b–d) Reproduced with permission.[194] Copyright 2017, the National Academy of Sciences. e) The cooperative interaction of codosed CO_2 and H_2O on Cu (111) composed of 0.08 ML of subsurface oxide. Reproduced with permission.[195] Copyright 2017, the National Academy of Sciences. f) Free energy profiles (at $U = -0.9$ V) for CO_2 activation on the MM (blue), FOM (red), and MEOM (green) models. Reproduced with permission.[196] Copyright 2017, the National Academy of Sciences. g) Schematic illustration of reconstruction of InN nanosheets during CO_2 electroreduction. h) XRD patterns of InN catalyst at different overpotentials. g,h) Reproduced with permission.[197] Copyright 2020, American Chemical Society.

coupling ability because of increasing adjacent Cu sites. On the contrary, as the loading density of Cu nanoparticles decreased, C1 product became the main product.

Copper based compounds such as oxide and sulfide will also be reduced to Cu^0 and undergo structural reconstruction under CO2RR working potential, as summarized in **Table 3**. In the reduction process, the Cu^{2+} was first reduced to Cu^+, and then further reduced to Cu^0, and the valence transition process has a great influence on surface composition, electronic structure, and morphology structure. Favato et al. found that the presence of a subsurface oxide layer below Cu surface atoms enhanced

the physical and chemical adsorption capacity for Cu sites to CO_2 using ambient pressure X-ray photoelectron spectroscopy (APXPS).[195] Furthermore, the chemisorbed CO_2 molecules were more easily to be protonated to form *$HCOO^-$ (Figure 12e). Xiao et al. reported similar phenomenon and they found that when Cu^+ and $Cu°$ coexisted, the kinetics and thermodynamics of CO_2 adsorption/activation and CO coupling were significantly improved, which enhanced the efficiency and selectivity of C2 products (Figure 12f).[196] Luna et al. recently showed that as the working potential gradually reduced, Cu^{2+} in sol–gel $Cu_2(OH)_3Cl$ was rapidly reduced to Cu^+, and took a long time to reduce to

**ADVANCED
SCIENCE NEWS**

www.advancedsciencenews.com

**ADVANCED
MATERIALS**

www.advmat.de

Table 3. Summary for the types of reconstruction-involved nonprecious metal-based precatalysts in CO_2RR, reconstructed species and their applied characterizations.

Types	Precatalysts	Electrolytes (temperatures)	Reconstructed species	Applied characterizations	Ref.
Cu-based	Wet oxidized Cu	0.05 M $KHCO_3$	Reconstructed Cu	TEM, Ex situ XAS, XRD, Raman	[219]
	$Cu_2(OH)_3Cl$	0.1 M $KHCO_3$	Dendrites Cu	SEM, XRD, in situ XAS	[216]
	Cu foil	0.25 M $KHCO_3$	Cu nanocube	SEM	[217]
	$V–Cu_2S$	0.1 M $KHCO_3$	$Cu_2S–Cu–V$	TEM, XPS, XAS	[220]
Molecular metal	Cu Dimer Distorted HKUST-1	1 M KOH	Cu cluster	In situ XAFS	[221]
	$[Cu(cyclam)]Cl_2$	0.5 M $KHCO_3$	Cu cluster	In situ XAFS, XRD; SEM	[193]
	CuPc	0.5 M $KHCO_3$	Cu cluster	In situ XAFS, XRD, SEM	
Others	SnS/Au	0.1 M $KHCO_3$	Sn(S)/Au	In situ XAFS	[214]
	BiOI	0.5 M $KHCO_3$	Bi nanosheets	TEM	[204]
	Bismuth oxide nanotubes	0.5 M $KHCO_3$	Defective metallic Bi	TEM, operando XAS	[213]
	FeAg NPs	0.1 M $KHCO_3$	Core–shell FeAg NPs	Operando (nuclear resonant inelastic X-ray scattering) NRIXS, XAFS	[222]
	$CeO_2/BiOCl$	0.5 M $KHCO_3$	CeO_x/Bi	Operando Raman, TEM	[223]
	Pd nanosheet	0.1 M PBS	Crumpled sheet-like structure Pd	TEM	[224]

Cu^0, which meant that the catalyst was in a state of coexistence of Cu^+ and $Cu°$ for a long time.[216] In addition, coming from the simultaneous dissolution of Cu^{2+}, O^{2-}, Cl^-, and redeposition of Cu^0, the surface structure of electrocatalysts evolved from smoothness to roundness at –0.7 V versus RHE and formed dendrites at –1.4 V versus RHE. Benefited from the co-existence of Cu^- and Cu^0, and more adjacent active sites, chemisorbed CO_2 was more stable and the C–C coupling could be promoted, thus inhibiting the methane selectivity and greatly improving the ethylene selectivity. However, as the reaction progresses, the oxidation state of the Cu sites is eventually reduced to Cu^0. Scott et al. demonstrated that there was no subsurface oxide layer for Cu_2O under CO reduction reaction using in situ grazing incidence XRD (GIXRD).[225] At present, there is no suitable theoretical explanation for maintaining the selectivity of the catalyst after a long-time reaction, which needs to be further explored through more experimental characterization.

Very recently, InN was also confirmed and could reconstruct to form the In-rich surface during CO_2 electroreduction into formate (Figure 12g).[197] In situ XRD patterns at open circuit potential and different applied potentials were also applied and suggested the formation of metallic In at high voltage bias (Figure 12h). This reconstruction resulted in the redistribution of surface charge and thus enhanced CO_2 electroreduction performance. Apart from above-mentioned electrocatalysts, such as Sn-based,[214] Bi-based[204,213] materials, have also experienced obvious reconstructed processes under working potential. Introduced by the changes in morphology, the reconstructed catalysts capable of defect sites and high active sites like ladder sites and cuspidal sites, which have low coordination numbers and high CO_2 adsorption and activation capabilities. It is hard to directly observe the reconstruction in CO_2RR because of the dynamic and high-speed process, so that more spectral and electron microscopy characterization with high spatial and temporal resolution are needed for further exploration.

5. Advanced Characterizations

5.1. Dynamic Reconstruction Uncovered by In Situ Technologies

During OER processes, the atomic/electronic structures of active sites in catalysts may change. If these changes are irreversible, it may cause the phase/microstructure reconstruction at macrolevel. Although the phase/microstructure evolution of precatalysts before and after catalytic reaction could be characterized via a series of ex situ characterization techniques, it is difficult to capture the key information of intermediates as well as obtain profound understandings of reconstruction mechanism. Therefore, developing advanced in situ characterization technologies and achieving real-time detection of catalyst surface states and atomic/electronic structure evolution are meaningful. It makes great significance for understanding the catalytic reaction mechanism and reconstruction electrochemistry, which is conducive to designing top-performance catalysts. Currently, there have been some relevant summaries on in situ characterizations for catalysis.[13–14] Even though, this part will complementally summarize the recent progress focused on in situ characterizations that are most frequently used for reconstruction-involved precatalysts.

In situ Raman can realize the nondestructive testing for the molecular microstructure information on the electrode surface/interface during liquid phase electrochemical operation.[13] It is one of the most commonly used methods to study catalytic reconstruction mechanism and identify active species. For example, we used in situ Raman to study the reconstruction process of hydrated nickel molybdate precatalyst (**Figure 13**a).[25] At applied oxidized potentials, the peaks for MoO_4 vibrations and Mo–O–Ni stretching disappeared first, and then the new peaks assigned to nickel (oxy)hydroxide emerged, which suggested the formation of real catalytic species. Hence, in situ Raman can provide the dynamic reconstruction information of chemical bond changes, the reconstructed species as well as its
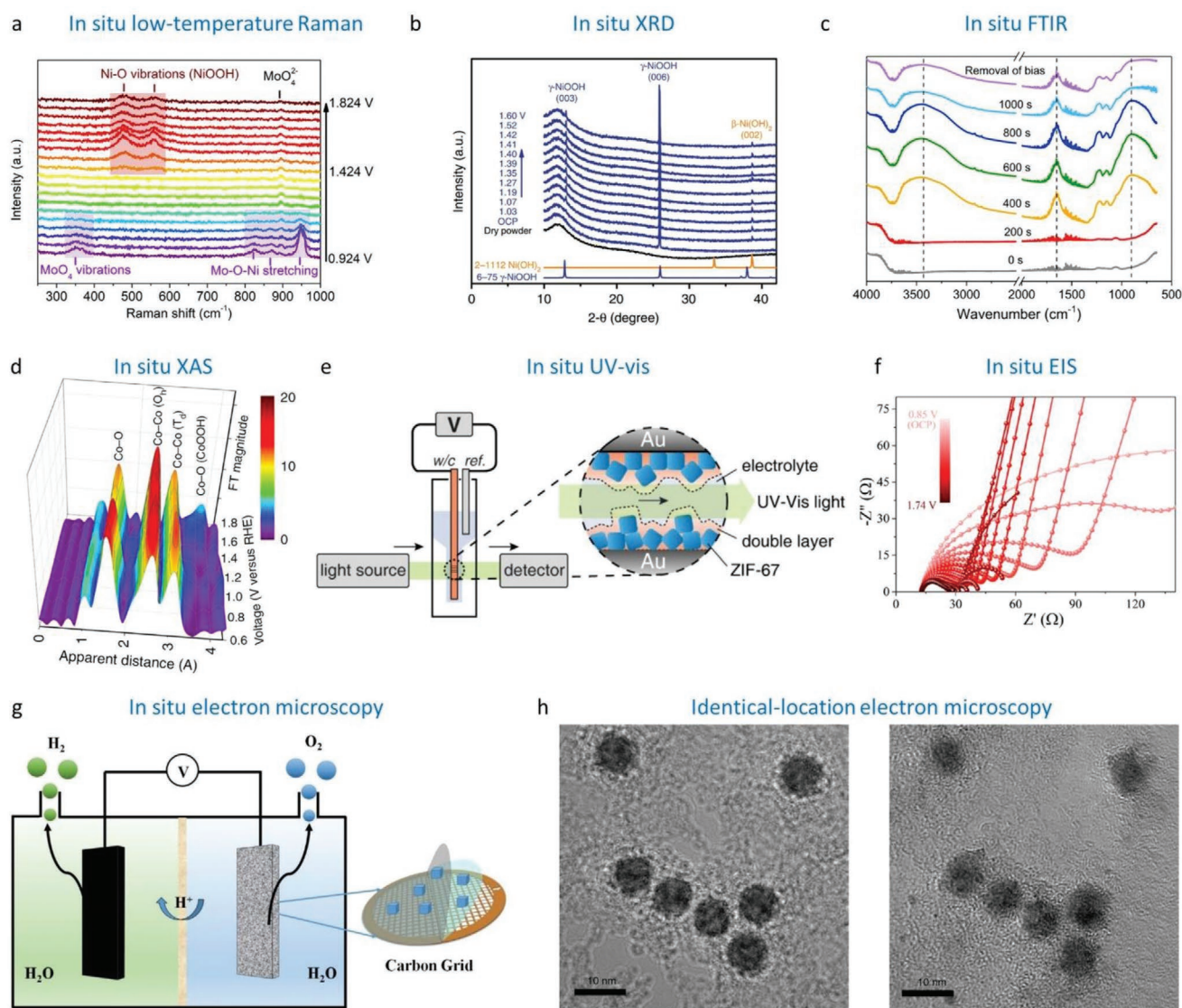
Figure 13. a) Potential-dependent in situ Raman spectra of NiMoO$_4$·xH$_2$O with the interval voltage of 50 mV in 1 M KOH at 25 °C. Reproduced with permission.[25] Copyright 2020, Elsevier. b) Operando XRD patterns collected on Ni(OH)$_2$/NF electrode at different potentials. Reproduced with permission.[226] Copyright 2018, Springer Nature. c) In situ FTIR spectra of CoS$_x$ anode with 1 mA anodic current in 1 M KOH. Reproduced with permission.[67] Copyright 2018, American Chemical Society. d) Voltage-dependence Fourier transform EXAFS spectra of Co$_3$O$_4$@CoO anode in 0.5 M KOH. Reproduced with permission.[95] Copyright 2015, Springer Nature. e) Simplified cell configuration and sampling of the electrode surface during in situ UV–vis experiment. Reproduced with permission.[36] Copyright 2019, American Chemical Society. f) Nyquist plots for Co$_3$O$_4$ catalyst with oxygen vacancy at different applied potentials versus RHE in 0.1 M KOH. Reproduced with permission.[97] Copyright 2020, American Chemical Society. g) Schematic diagram to illustrate the operation of the in situ TEM observation for OER process. Reproduced with permission.[67] Copyright 2018, American Chemical Society. h) Identical-location HRTEM images of nanoparticles before (left) and after (right) electrochemical oxidation. Reproduced with permission.[47] Copyright 2018, Springer Nature.

formation conditions. Nevertheless, the OER-associated in situ Raman in the reported works was commonly operated under normal temperature conditions.[100,226–228] Considering that the industrial water electrolysis is operated at high temperature of 50–80 °C, we recently carried out in situ high-temperature Raman testing, and studied the differences in reconstruction results at different temperatures. Different from that at room temperature, the nickel molybdate precatalyst could be fast self-collapse and completely reconstructed under the condition

of high-temperature OER as the Raman peaks referred to the nickel molybdate appeared. This indicates that the in situ low-/high-temperature Raman is a powerful tool to study the temperature-reconstruction correlation.

In situ XRD is a method to monitor the phase transformation and structural evolution in real time, and is widely applied in batteries. Due to the catalytic reaction mainly occurs on the catalyst surface and the change of body phase is generally nonobvious, thus this technology is rarely used in investigating

**ADVANCED
SCIENCE NEWS**

www.advancedsciencenews.com

**ADVANCED
MATERIALS**

www.advmat.de

structure evolution in catalysis. Recently, Chen et al. uncovered the phase evolution of amorphous $Ni(OH)_2$ and $NiCeO_xH_y$ materials during OER via in situ XRD technique.[226] Taking $Ni(OH)_2$ as an example (Figure 13b), it showed the considerable crystallinity after shortly aging in 1 M KOH. Then, the main phase of γ-NiOOH existed at oxidized potentials. Although in situ XRD technology can provide phase evolution information, it is difficult to obtain reconstruction-related diffraction information in the case of precatalysts with high crystallinity, the low reconstruction degree or the amorphous structure of the reconstruction species. Consequently, this technology is more suitable for chemical reconstruction analysis on the deeply reconstructed catalysts. This could be reflected by a recent typical example about complete reconstruction. Zhang et al. studied core–shell carbon wrapped iron nitride ($Fe_2N@C$) nanoparticles for efficient hydrogenation of CO_2 to C_{2+} hydrocarbons.[229] The time-dependent crystal phase reconstruction was confirmed via in situ XRD measurements. During CO_2 hydrogenation, the diffraction peaks for Fe_2N were vanished and there was a complete phase change from Fe_2N to $Fe_{2.5}C$, and the formed one was recognized as the veritable active species. It should be noted that the reconstruction of internal Fe_2N also occurred despite the presence of carbon coating. This would be attributed to the thin and porous carbon layer, and the existence of void between the carbon shell and Fe_2N core. The presence of carbon has no significant effect on the in situ XRD test. Summarily, in situ XRD is a powerful tool to study the chemical reconstruction with obvious phase changes.

In situ Fourier-transform infrared spectroscopy (FTIR) can be used to phase evolution detection during the reconstruction process because of its high-resolution identification on newly formed species. For example, Yu et al. utilized this technique proved the enhanced H_2O adsorption, the formation of hydroxides, and irreversible phase transformation of CoS_x catalysts during OER (Figure 13c).[67] Recently, Zhang et al. implemented in situ diffuse reflectance infrared Fourier transform spectroscopy (DRIFTS) to uncover the phase reconstruction mechanism during CO_2 hydrogenation of Fe_2N precatalyst.[229] The in situ formed carbonyl iron intermediate was detected, which was responsible for the conversion mechanism from iron nitrides to iron carbides. This intermediate was not detectable by in situ XRD, which suggests the superiority of in situ FTIR in the detection of reconstructed intermediates.

In situ XAS can accurately detect the dynamic change process of atomic scale structure under operation conditions, and serves as one of the most powerful tools in electronic structure characterization of catalyst. Figure 13d displayed the Fourier transform extended X-ray absorption fine structure spectra of $Co_3O_4@CoO$ at different potentials, which confirmed the formation of surface cobalt (oxy)hydroxide at high oxidation potentials.[95] In recent years, this technique is widely used to uncover the reconstruction and catalytic mechanism during OER catalysis.[40,230]

In situ UV–vis can collect the dynamic structure information via the interaction between ultraviolet visible light and the electrode surface species during electrochemical testing. For example, Lee et al. used this in situ technique to unveil the dramatic and irreversible structure evolution of ZIF-67 at various applied potentials, and the schematic diagram for the

simplified cell configurations and sampling processes during catalytic testing was displayed (Figure 13e).[36] The structure destruction of ZIF-67 and the newly formed high-valence Co species were revealed. In addition, when the new species were generated during electrochemical oxidation, such as the $Ni^{2+} \rightarrow Ni^{3+}$ process at high oxidation potentials for nickel-based catalysts, the optical transitions occurred.[186]

In situ EIS can be applied in reconstruction researches for the real-time detection of the catalytic reaction kinetics and electrode-electrolyte interface properties. For example, Wang et al. utilized in situ EIS and based on the Laviron equation to uncover the roles of oxygen vacancy, which could facilitate the preoxidation reconstruction of low-valence Co at low overpotentials (Figure 13f).[97] In addition, this in situ technology can obtain the impedance changes in the reconstruction process and the relationship between microstructure evolution and performance.[99] This characterization is relatively simple and easy to operate, and is expected to attract more attention in the reconstruction research.

In situ electron microscopy can directly visualize the transformation of precatalysts during the reconstruction process, which includes the changes in microstructure, exposed crystal planes, chemical components. Figure 13g displays the schematic diagram for in situ TEM observation, which includes adding catalyst ink on the carbon grid clamped for OER and performing TEM at the same time.[67] Based on this technology, Yu et al. captured the dynamic reconstruction process of CoS_x during alkali OER. Combined with corresponding selected area electron diffraction (SAED) patterns, the phase evolution of amorphous $CoS_x \rightarrow Co(OH)_2 \rightarrow$ low-crystalline CoOOH was confirmed. Liu et al. observed the newly formed Co_2P after HER catalysis based on CoFeO-black phosphorus composite.[191] Nevertheless, because of the rigor of the experimental operation, this method is rarely reported in the reconstruction research, but it deserves our attention.

Identical-location electron microscopy is a kind of quasi-in situ electron microscopy characterization method that could visualize structures at the nanoscale. It provides the microstructure information of catalysts located on the carbon grid in the same position. For example, Chorkendorff et al. observed the morphological and crystallinity information of granular catalysts before and after electrocatalytic reaction (Figure 13h).[47] Therefore, this methodology is very effective to analyze the morphology and phase evolution at different reconstruction stages, which is of great significance for revealing the structure–performance relationship.[231]

X-ray photoelectron spectroscopy is a sensitive surface analytical tool, and its quasi-operando operation was also utilized for reconstruction research reported by Wang group.[97] Using this method, the Co^{2+}/Co^{3+} ratio evolution of cobalt oxides at different potentials was provided, suggesting its oxidation phenomenon during OER. Summarily, these above-mentioned (quasi-) in situ techniques are heavily anticipated to monitor the electrocatalysis process in recent years, especially for the reconstruction-involved catalysis. Though these still exist some technical problems or expensive instrument concerns, the development of advanced in situ techniques will promote the comprehensive understanding of catalytic mechanism in a dynamic way.
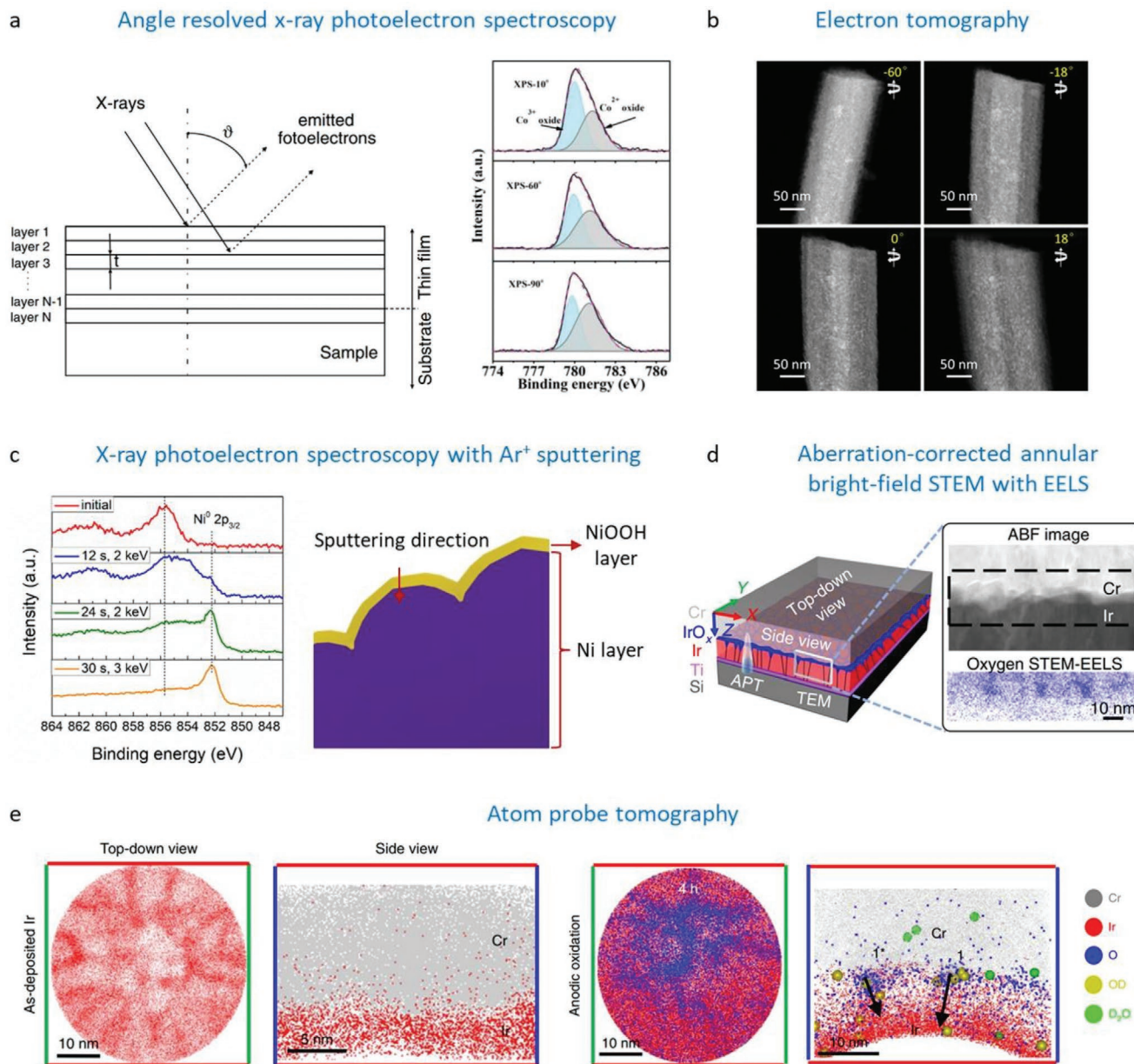
ADVANCED
SCIENCE NEWS
www.advancedsciencenews.com

ADVANCED
MATERIALS
www.advmat.de

Figure 14. a) The model for calculations in ARXPS measurements (left). The peak intensities are calculated for a set of emission angles, while the angle between X-rays and detected electrons is kept constant. Reproduced with permission.[232] Copyright 2010, Wiley-VCH. ARXPS spectra of Co 2p3/2 for CoₓP-E at a take-off angle of 10°, 60°, and 90° (with respect to the surface normal), respectively (right). Reproduced with permission.[37] Copyright 2020, Wiley-VCH. b) Representative HAADF-STEM images captured from multiangle electron tomography video of single NiOOH nanowire. Reproduced with permission.[25] Copyright 2020, Elsevier. c) High-resolution depth-sputtering Ni 2p XPS spectra of Ni@NiOOH and its schematic diagram for sputtering. Reproduced with permission.[29] Copyright 2019, American Chemical Society. d) Schematic of sample and surface morphology of Ir after anodic oxidation, as well as its ABF image and STEM-EELS mapping of O K edge. e) Top-down view and side view of APT reconstructions of as-deposited Ir initially and anodic oxidation for 4 h, respectively. d,e) Reproduced with permission.[233] Copyright 2018, Springer Nature.

5.2. Advanced Technologies Used to Characterize the Completely Reconstructed Catalysts

For the structural and component characterizations of catalysts after reconstruction (hereinafter denoted as reconstruction catalysts), the limited information could be obtained using conventional characterizations, such as XRD, SEM, TEM, and Raman techniques. In this section, we will introduce four infrequently reported techniques for multiangle/level characterizations and their applications in reconstruction researches.

Angle resolved X-ray photoelectron spectroscopy (ARXPS) is a kind of nondestructive analysis technique, which collects electrons by changing the emission angle and detects electrons at different depths (**Figure 14**a, left).[232] It can provide electronic structure information of thin film, and serves as an effective method for understanding interface chemistry. For example,

**ADVANCED
SCIENCE NEWS**

www.advancedsciencenews.com

**ADVANCED
MATERIALS**

www.advmat.de

Wang et al. studied the surface composition of Co_xP after anodic oxidation treatment (Co_xP-E) via such a technique (Figure 14a, right).[37] When take-off angles of electrons decreased from 90° to 10°, the Co^{3+}/Co^{2+} ratio values increased from 0.453 to 1.392. This suggested that the Co^{3+} species were mainly distributed on the surface. The similar results were also obtained in terms of Co_xN precatalysts after OER reconstruction. Therefore, this method can be applied to detect component information within 1–10 nm surface of the reconstruction-involved precatalysts.

Multiangle electron tomography is an imaging technique to acquire 3D spatial information with nanometer scale resolution from 2D electronic projection at a series of tilted angles. For example, the hydrated nickel molybdate precatalyst can be completely reconstructed to nickel (oxy)hydroxide, and its multiangle stereoscopic structure characteristics were obtained via this technique. As shown in Figure 14b, the representative high-angle annular dark-field STEM (HAADF-STEM) images were provided from electron tomography video conducted at consecutive rotational angles from -60° to 48°.[25] On one hand, the high uniformity of ultrasmall nanoparticles and undiscovered apparent particle agglomeration was proved. On the other hand, it revealed the multilevel nanowire structure with irregular cross section and porous structure. In addition, the combination of electron tomography and element distribution analyses will provide more detailed component distribution of 3D structure.[234] Therefore, this combined technique will be an effective way to reveal the distribution information of the reconstructed species and original one in surface reconstruction catalysts.

X-ray photoelectron spectroscopy with Ar^+ sputtering can acquire the chemical state changes with the depth of sample surface. For example, our group found the formation of core–shell Ni@NiOOH particles derived from the oxidation reconstruction of Ni particles, and its core–shell structure was confirmed via XPS-Ar^+ sputtering method.[29] As displayed in Figure 14c, the Ni^0 peak was undetected from the Ni 2p XPS spectrum of the initial sample; After Ar^+ sputtering, the peak for Ni^0 was more and more obvious, and the high-valence Ni XPS peak gradually diminished or even disappeared. Therefore, the XPS-Ar^+ sputtering technique can be applied to analyze the chemical component as the change of sputtering depth in surface reconstruction catalysts.

Aberration-corrected annular bright-field (ABF) STEM with electron energy-loss spectroscopy (EELS) is a kind of nanoscale spatial resolution analysis technology. Mayrhofer et al. used this technology to provide the nanoscale microstructure information of oxide film (Figure 14d).[233] Hence, it can detailedly analyze the surface component and nanoscale spatial distribution of surface reconstruction catalysts.

Atom probe tomography (APT) is an analysis technology to provide 3D reconstruction information of chemical species on the atomic scale. Mayrhofer et al. carried out such a high-end near-atomic-scale characterization to obtain the 3D distribution maps of single atom on the surface oxides under anodic oxidation condition (Figure 14e).[233] The absence of oxygen on the initial Ir surface could be observed from side view. Then after the anodic polarization proceeds for 4 h, the oxide layer with several nanometer thickness was uneven coverage on the surface. This technology was also used to prove the uniform distribution of dopant atoms.[235]

In summary, considering the surface atomic layer determines the catalytic mechanism of catalyst and reaction kinetics, therefore, it is significant to investigate surface state change of surface reconstruction catalyst at high resolution, which is also an important development direction in the future.

6. Conclusions and Outlook

This review systemically summarized the recent progresses of complete reconstruction in electrocatalysis applications, and fundamental insights into complete reconstruction and reconstructed materials. We first expound the fundamental understandings of complete reconstruction, including reasons why reconstruction happens and several classifications of reconstruction results based on reconstruction degree. The characteristics and advantages of completely reconstructed catalysts and their design principles are discussed and highlighted. Because the alkaline OER catalysis is one of the hottest researches nowadays, we take it as an example and introduce mechanisms, and mainly conclude the types of reconstruction-involved OER precatalysts (i.e., metals/alloys, oxides/hydroxides, phosphorus/boron-containing compounds, dichalcogenides, carbides/nitrides, MOFs, PBAs, hydrates, and others), as well as summarize the precatalysts applied in acidic/neutral OER catalysis; meanwhile, several reasons why the limited reconstruction exists are analyzed, and the strategies for deepened reconstruction till complete are summarized, which includes self-instability, structural modulation, and extreme testing conditions. Complete reconstruction is expected to be applied in novel material synthesis and other electrocatalysis (such as HER and CO_2 reduction), and several representative examples are provided. Finally, several (quasi-) in situ characterization techniques are introduced to reveal dynamic reconstruction process and real catalytic species. For the structure identification of reconstructed catalysts, some infrequently reported techniques for multiangle/level characterizations are also presented. With the development of in situ techniques in recent years, some progress has been made in understanding the reconstruction phenomenon and the intrinsic mechanism of materials in energy conversion. Even though, in-depth understanding of reconstruction chemistry, controllable reconstruction engineering, design synthesis of completely reconstructed catalysts and their applications still require further exploration and discrimination. As for the future development of reconstruction chemistry, there are several opportunities and challenges need to be considered.

1) *In terms of reconstruction recognition.* Although there are more and more researches on catalyst reconstruction in recent years, a series of basic scientific problems are still in its infancy. a) It is divided on this issue whether the reconstruction occurs on one catalyst or not. For example, Ma did not find the oxidation-induced reconstruction phenomenon of $Co_3(PO_4)_2$ applied in neutral OER,[168] which was different from the observations by Cao group.[119] b) For reconstruction-involved catalysis mechanism analyses, there are inconsistencies and debates whether the established models for density functional theory calculations are based on precatalysts or

reconstructed species. For example, Xu et al. uncovered the generation of (oxy)hydroxides via reconstruction based on Co–Ni metaphosphates, and the mechanism analyses were based on metaphosphate structure.[59] Differently, Zhang et al. found that $Na_xCoFe(CN)_6$ could evolve into CoOOH, and the OER catalytic mechanism was analyzed on CoOOH models.[80] c) For reconstruction-involved catalysts, some works stated that the constructed species were not the real active species. For example, Kim et al. demonstrated a small amount of Fe–Co oxides or (oxy)hydroxides formed on the $Fe_3Co(PO_4)_4$ catalysts during OER.[122] However, the Fe-sites of $Fe_3Co(PO_4)_4$ were considered as active sites because the theoretical overpotential of 240 mV was in excellent agreement with the experimental results. In this case, how to inhibit the reconstruction is the key point for the remained catalytic activity. d) For one catalyst, it is still unclear about the certainty in reconstructed species, whether the residue doping elements or formed species exist in the reconstructed catalysts, and whether the residues affect OER activity. Hu et al. observed the ≈10 nm thick NiO_x layer formed on the surface of Ni_2P after OER testing.[17] The P species existed in the NiO_x layer and were attributed to the residual P_2O_5. However, Chen et al. obtained the core–shell Ni_2P/NiOOH structure.[58] The P species were attributed to phosphates, and the detailed explanation was not provided in terms of its impact on OER activity. e) Which is better, partial or complete reconstruction? Because the reconstructed species provide the real catalytic sites, higher catalytic current can be generated for the completely reconstructed catalysts. This could be confirmed via chronopotentiometry results with gradually decreased overpotentials, in which the reconstruction degree gradually deepened to complete.[25] It was reported that the partially reconstructed catalysts had better mechanical stability.[26] In spite of this, our obtained completely reconstructed catalysts could guarantee at least thousands of hours of stable catalysis, and thus this issue requires more experimental proof and mechanism analysis. In addition, catalyst conductivity should not be ignored as it is vital for fast catalysis. For precatalysts with metallic character, such as phosphides and nitrides, the remaining original one in the core could provide rapid electron conduction and the reconstructed species in the shell offer efficient catalytic sites.[41,58,143] This surface reconstruction model may be better than that of completely reconstructed one. Moreover, very recently, Masa et al. studied the chemical stability of Ni_yP in 1 M KOH at 80 °C.[48] However, the completely reconstructed one did not display the best OER activity because of the loss of P species. Under such a harsh condition, the complete reconstruction from Ni_yP to oxide/(oxy)hydroxide was inevitable. Therefore, this raises a challenge on how to avoid/reduce the loss of P to remain high activity of reconstructed catalyst. f) Origins of reconstruction. At present, only a few papers have analyzed the causes of limited reconstruction, and its research will be helpful in revealing the reconstruction processes. g) For one catalyst, its electrocatalytic stability (i.e., stable catalytic reaction) should be closely associated with the chemical stability (i.e., catalytic components and sites), which does not get enough attention it deserves. h) The relationship between reconstruction process and pH of solution is also expected to

be explored, which is helpful to understand reconstruction mechanisms and the reasons for choosing test solution. i) Investigations on the origin of reconstruction, the intermediate during reconstruction, and the final reconstructed species is highly required to get depth insights into reconstruction mechanisms. For a typical example, Zhang et al. provided the depth understanding of reconstruction mechanism of nitride catalyst during CO_2 hydrogenation via various characterizations.[229] The in situ formed carbonyl iron was detected and recognized as the key intermediate for the conversion from nitride to carbide. To sum up, it is urgent to further explore the scientific issues including the reconstruction chemistry of precatalysts, the recognition of the fine structure for reconstructed species, the relationship between catalyst structure and catalytic activity, as well as the identification of real active sites. These will promote a profound understanding of the intrinsic catalytic mechanism for OER precatalysts.

2) *Optimal conditions for the reconstruction of precatalysts.* In fact, before the performance evaluation of catalyst, the activation process such as CV cycles are generally carried out. For example, in Yan's work, "working electrodes were scanned for several potential cycles until the signals were stabilized, and then the CV data were collected."[94] This activation process can not only promote the electrolyte with good contact with catalyst, but also can make the catalyst surface to achieve stable state. Therefore, the CV test could be a way to achieve the reconstruction of precatalysts. However, a few rounds of CV test may not be able to get intrinsic catalytic activity. For example, Mullins et al. studied the transformation of Co_3C OER precatalyst, and its potential reached a stable value after 150-cycle CV.[38] Therefore, the detailed CV cycles to reach a steady state are uncertain and related to the type and property of precatalysts. The chronopotentiometric measurement is another "activation" method. For example, in our previous work, we also carried out chronopotentiometric measurement before activity evaluation.[24–25] When the chronopotentiometric curve is stable, the catalyst can be considered to be stable. Similar to chronopotentiometric one, chronoamperometric test could also be a method. These raise the curiousness on how different activation treatments affect the reconstruction and which is the optimal one. In our opinion, the CV method differs from the other two, because it is a continuous redox process, while the other two are continuously applied with an oxidation or reduction voltage. This may lead to a difference in the microstructure and composition of the reconstructed catalyst.

3) *Activity comparison between precatalysts and corresponding reconstructed species.* In Section 2.1, there are some discussion about the activity comparison. Even though, this requires more experimental evidences and theoretical supports, and deserves attention and research. For example, if the catalytic activity of precatalyst is higher than that of its reconstructed species, some strategies are needed to adopt to suppress the occurrence of reconstruction. Therefore, identifying the intrinsic activity of precatalyst is also meaningful. In this case, how to inhibit the reconstruction to remain the original high-activity of precatalysts is a challenge.

4) *Reconstruction mechanism under realistic conditions.* Taking the researches of alkaline water electrolysis as an example, the test parameters (generally at room temperature, 0.1–1 M

KOH, durability of less than 100 h) in most reports have a certain gap with the industrial one (at 50–80 °C, 20–30 wt% KOH, at least 1000 h). In this case, the reconstruction results of catalysts may be different, such as reconstruction degree, evolved species, and microstructure. For example, different from that in 1 M KOH, the complete reconstruction of anhydrous molybdate precatalyst under industrial conditions (20–30 wt% KOH) was observed.[25] Therefore, understanding the intrinsic reconstruction mechanisms under realistic conditions is thus meaningful and necessary, and here it is vital to utilize in situ characterization techniques to capture real-time reconstruction processes.

5) *Synthesis of new structural materials via reconstruction engineering.* In the past several years, the reconstruction in other catalysis and battery fields is proposed and implemented. The reconstructed materials can possess unique structure/component which could not be synthesized by traditional methods. By simple conventional chemical etching reaction[187] or electrochemical deposition reaction,[135] the obtained materials display bulk or large size structure with high crystallinity. For example, after soaking in sodium hydroxide solution, the sheet formed on the surface of nickel hexacyanoferrate nanocubes, and such a result might be attributed that the etched area extended preferably along each face of nanocubes.[187] For the proposed reconstruction engineering in this review, it is essentially a combination of "chemistry+electrochemistry," which can serve as a novel pathway to synthesize materials with unique component/microstructure. For example, we fabricated ultrasmall (oxy)hydroxide nanoparticle-interconnected structure with low crystallinity which was utilized the complete reconstruction of hydrated molybdate OER precatalysts.[25] This unique structure has not been reported and could solve the aggregation problem in traditional granular catalysts. This also raises the curiousness why such a unique structure forms, and thus the relationship between reconstruction and derived microstructure needs to be further explored.

6) *Complete reconstruction for energy storage applications.* Reconstruction concepts applied in capacitors and batteries have also been reported in recent years. Our group found the activation phenomenon of α-Fe_2O_3 during supercapacitor performance evaluation.[236] After electrochemical cyclings in alkali, the α-Fe_2O_3 with high-crystalline structure was completely reconstructed to low-crystalline FeOOH. This activation process guaranteed the obtained FeOOH nanoparticles with high capacity performance, and the top-performance packaged device was fabricated when coupled with $NiMoO_4$ electrode. Besides, Zhi et al. discovered the phase transition of V-based MXene cathode during Zn-storage, which resulted in the unusual capacity enhancement after cycling.[237] These works demonstrated the positive effects of electrochemical reconstruction in energy storage performance. Therefore, the application of completely reconstructed materials in the field of energy storage deserves our attention.

Despite the certain recognition of reconstruction chemistry has been achieved, it is required to further research on underlying reconstruction mechanism, engineering in complete reconstruction, and reconstruction–performance correlation. The systematic summary of complete reconstruction in this review will on one hand, aim at broadcasting the real contributors during catalysis to acquire intrinsic catalytic mechanism and rational design of top-performance catalysts; on the other hand, highlight advantages and synthesis strategies of completely reconstructed catalysts, and open up new pathways for applying complete reconstruction materials in other fields such as energy storage.

Conflict of Interest

The authors declare no conflict of interest.

[1] S. Park, Y. Y. Shao, J. Liu, Y. Wang, *Energy Environ. Sci.* **2012**, *5*, 9331.

[2] K. Zeng, D. K. Zhang, *Prog. Energy Combust. Sci.* **2010**, *36*, 307.

[3] Y. M. Lee, J. Suntivich, K. J. May, E. E. Perry, Y. Shao-Horn, *J. Phys. Chem. Lett.* **2012**, *3*, 399.

[4] A. Buttler, H. Spliethoff, *Renew. Sustainable Energy Rev.* **2018**, *82*, 2440.

[5] M. Ni, M. Leung, K. Sumathy, D. Leung, *Int. J. Hydrogen Energy* **2006**, *31*, 1401.

[6] X. Y. Lu, J. Pan, E. Lovell, T. H. Tan, Y. H. Ng, R. Amal, *Energy Environ. Sci.* **2018**, *11*, 1898.

[7] X. Liu, K. Ni, C. J. Niu, R. T. Guo, W. Xi, Z. Y. Wang, J. S. Meng, J. T. Li, Y. W. Zhu, P. J. Wu, Q. Li, J. Luo, X. J. Wu, L. Q. Mai, *ACS Catal.* **2019**, *9*, 2275.

[8] J. Zhang, T. Wang, P. Liu, Z. Q. Liao, S. H. Liu, X. D. Zhuang, M. W. Chen, E. Zschech, X. L. Feng, *Nat. Commun.* **2017**, *8*, 15437.

[9] L. Han, S. J. Dong, E. K. Wang, *Adv. Mater.* **2016**, *28*, 9266.

[10] R. Gao, D. P. Yan, *Adv. Energy Mater.* **2019**, *10*, 1900954.

[11] H. M. Sun, Z. H. Yan, F. M. Liu, W. C. Xu, F. Y. Cheng, J. Chen, *Adv. Mater.* **2020**, *32*, 1806326.

[12] N. H. Chou, P. N. Ross, A. T. Bell, T. D. Tilley, *ChemSusChem* **2011**, *4*, 1566.

[13] K. Y. Zhu, X. F. Zhu, W. S. Yang, *Angew. Chem., Int. Ed.* **2019**, *58*, 1252.

[14] X. N. Li, H.-Y. Wang, H. B. Yang, W. Z. Cai, S. Liu, B. Liu, *Small Methods* **2018**, *2*, 1700395.

[15] S. Jin, *ACS Energy Lett.* **2017**, *2*, 1937.

[16] B. R. Wygant, K. Kawashima, C. B. Mullins, *ACS Energy Lett.* **2018**, *3*, 2956.

[17] L.-A. Stern, L. G. Feng, F. Song, X. L. Hu, *Energy Environ. Sci.* **2015**, *8*, 2347.

**ADVANCED
SCIENCE NEWS**

www.advancedsciencenews.com

**ADVANCED
MATERIALS**

www.advmat.de

[18] Y. Y. Li, X. C. Du, J. W. Huang, C. Y. Wu, Y. H. Sun, G. F. Zou, C. T. Yang, J. Xiong, *Small* **2019**, *15*, 1901980.

[19] H. L. Jiang, Q. He, Y. K. Zhang, L. Song, *Acc. Chem. Res.* **2018**, *51*, 2968.

[20] N. C. S. Selvam, L. J. Du, B. Y. Xia, P. J. Yoo, B. You, *Adv. Funct. Mater.* **2020**, 2008190, https://doi.org/10.1002/adfm.202008190.

[21] A. Sivanantham, P. Ganesan, A. Vinu, S. Shanmugam, *ACS Catal.* **2019**, *10*, 463.

[22] D. A. Kuznetsov, B. H. Han, Y. Yu, R. R. Rao, J. Hwang, Y. Román-Leshkov, Y. Shao-Horn, *Joule* **2018**, *2*, 225.

[23] J. Z. Liu, Q. Hu, Y. Wang, Z. Yang, X. Y. Fan, L.-M. Liu, L. Guo, *Proc. Natl. Acad. Sci. USA* **2020**, *117*, 21906.

[24] X. Liu, R. T. Guo, K. Ni, F. J. Xia, C. J. Niu, B. Wen, J. S. Meng, P. J. Wu, J. S. Wu, X. J. Wu, L. Q. Mai, *Adv. Mater.* **2020**, *32*, 2001136.

[25] X. Liu, J. S. Meng, K. Ni, R. T. Guo, F. J. Xia, J. J. Xie, X. Li, B. Wen, P. J. Wu, M. Li, J. S. Wu, X. J. Wu, L. Q. Mai, D. Y. Zhao, *Cell Rep. Phys. Sci.* **2020**, *4*, 100241.

[26] B. W. Zhang, K. Jiang, H. T. Wang, S. Hu, *Nano Lett.* **2019**, *19*, 530.

[27] Q. C. Xu, H. Jiang, X. Z. Duan, Z. Jiang, Y. J. Hu, S. W. Boettcher, W. Y. Zhang, S. J. Guo, C. Z. Li, *Nano Lett.* **2021**, *21*, 492.

[28] X. Ren, C. Wei, Y. M. Sun, X. Z. Liu, F. Q. Meng, X. X. Meng, S. N. Sun, S. B. Xi, Y. H. Du, Z. F. Bi, G. Y. Shang, A. C. Fisher, L. Gu, Z. C. J. Xu, *Adv. Mater.* **2020**, *32*, 2001292.

[29] X. Liu, K. Ni, B. Wen, R. T. Guo, C. J. Niu, J. S. Meng, Q. Li, P. J. Wu, Y. W. Zhu, X. J. Wu, L. Q. Mai, *ACS Energy Lett.* **2019**, *4*, 2585.

[30] N. Ortiz Peña, D. Ihiawakrim, M. Han, B. Lassalle-Kaiser, S. Carenco, C. Sanchez, C. Laberty-Robert, D. Portehault, O. Ersen, *ACS Nano* **2019**, *13*, 11372.

[31] B. L. Wang, K. N. Zhao, Z. Yu, C. L. Sun, Z. Wang, N. N. Feng, L. Q. Mai, Y. G. Wang, Y. Y. Xia, *Energy Environ. Sci.* **2020**, *13*, 2200.

[32] J. Masa, I. Sinev, H. Mistry, E. Ventosa, M. de la Mata, J. Arbiol, M. Muhler, B. R. Cuenya, W. Schuhmann, *Adv. Energy Mater.* **2017**, *7*, 1700381.

[33] H. L. Jiang, Q. He, X. Y. Li, X. Z. Su, Y. K. Zhang, S. M. Chen, S. Zhang, G. Z. Zhang, J. Jiang, Y. Luo, P. M. Ajayan, L. Song, *Adv. Mater.* **2019**, *31*, 1805127.

[34] Z. Y. Wang, J. T. Li, X. C. Tian, X. P. Wang, Y. Yu, K. A. Owusu, L. He, L. Q. Mai, *ACS Appl. Mater. Interfaces* **2016**, *8*, 19386.

[35] F. Podjaski, D. Weber, S. Y. Zhang, L. Diehl, R. Eger, V. Duppel, E. Alarcón-Lladó, G. Richter, F. Haase, A. F. i Morral, C. Scheu, B. V. Lotsch, *Nat. Catal.* **2019**, *3*, 55.

[36] W. R. Zheng, M. J. Liu, L. Y. S. Lee, *ACS Catal.* **2019**, *10*, 81.

[37] Y. H. Lyu, J. Y. Zheng, Z. H. Xiao, S. Y. Zhao, S. P. Jiang, S. Y. Wang, *Small* **2020**, *16*, 1906867.

[38] J.-H. Kim, K. Kawashima, B. R. Wygant, O. Mabayoje, Y. Liu, J. H. Wang, C. B. Mullins, *ACS Appl. Energy Mater.* **2018**, *1*, 5145.

[39] S. Zhang, S. Q. Gu, Y. Wang, C. Liang, Y. Yu, L. Han, S. Zheng, N. Zhang, X. S. Liu, J. Zhou, J. Li, *ACS Catal.* **2019**, *9*, 7389.

[40] T. Z. Wu, S. N. Sun, J. J. Song, S. B. Xi, Y. H. Du, B. Chen, W. A. Sasangka, H. B. Liao, C. L. Gan, G. G. Scherer, L. Zeng, H. J. Wang, H. Li, A. Grimaud, Z. C. J. Xu, *Nat. Catal.* **2019**, *2*, 763.

[41] P. Z. Chen, K. Xu, Z. W. Fang, Y. Tong, J. C. Wu, X. L. Lu, X. Peng, H. Ding, C. Z. Wu, Y. Xie, *Angew. Chem., Int. Ed.* **2015**, *54*, 14710.

[42] Y. Wang, Y. L. Zhu, S. L. Zhao, S. X. She, F. F. Zhang, Y. Chen, T. Williams, T. Gengenbach, L. H. Zu, H. Y. Mao, W. Zhou, Z. P. Shao, H. T. Wang, J. Tang, D. Y. Zhao, C. Selomulya, *Matter* **2020**, *3*, 2124.

[43] H. Li, P. Wen, Q. Li, C. C. Dun, J. H. Xing, C. Lu, S. Adhikari, L. Jiang, D. L. Carroll, S. M. Geyer, *Adv. Energy Mater.* **2017**, *7*, 1700513.

[44] Y. B. Chen, H. Y. Li, J. X. Wang, Y. H. Du, S. B. Xi, Y. M. Sun, M. Sherburne, J. W. Ager III, A. C. Fisher, Z. C. J. Xu, *Nat. Commun.* **2019**, *10*, 572.

[45] T. T. Zheng, C. Y. Shang, Z. H. He, X. Y. Wang, C. Cao, H. L. Li, R. Si, B. C. Pan, S. M. Zhou, J. Zeng, *Angew. Chem., Int. Ed.* **2019**, *58*, 14764.

[46] T. Y. Wang, G. Nam, Y. Jin, X. Y. Wang, P. J. Ren, M. G. Kim, J. S. Liang, X. D. Wen, H. Jang, J. T. Han, Y. H. Huang, Q. Li, J. Cho, *Adv. Mater.* **2018**, *30*, 1800757.

[47] C. Roy, B. Sebok, S. B. Scott, E. M. Fiordaliso, J. E. Sørensen, A. Bodin, D. B. Trimarco, C. D. Damsgaard, P. C. K. Vesborg, O. Hansen, I. E. L. Stephens, J. Kibsgaard, I. Chorkendorff, *Nat. Catal.* **2018**, *1*, 820.

[48] P. Wilde, S. Dieckhöfer, T. Quast, W. K. Xiang, A. Bhatt, Y.-T. Chen, S. Seisel, S. Barwe, C. Andronescu, T. Li, W. Schuhmann, J. Masa, *ACS Appl. Energy Mater.* **2020**, *3*, 2304.

[49] Y. M. Sun, H. B. Liao, J. R. Wang, B. Chen, S. N. Sun, S. J. H. Ong, S. B. Xi, C. Z. Diao, Y. H. Du, J.-O. Wang, M. B. H. Breese, S. Z. Li, H. Zhang, Z. C. J. Xu, *Nat. Catal.* **2020**, *3*, 554.

[50] B. You, Y. J. Sun, *Acc. Chem. Res.* **2018**, *51*, 1571.

[51] I. C. Man, H. Y. Su, F. Calle-Vallejo, H. A. Hansen, J. I. Martínez, N. G. Inoglu, J. Kitchin, T. F. Jaramillo, J. K. Nørskov, J. Rossmeisl, *ChemCatChem* **2011**, *3*, 1159.

[52] W. J. Dai, T. Lu, Y. Pan, *J. Power Sources* **2019**, *430*, 104.

[53] L. Yu, H. Q. Zhou, J. Y. Sun, F. Qin, F. Yu, J. M. Bao, Y. Yu, S. Chen, Z. F. Ren, *Energy Environ. Sci.* **2017**, *10*, 1820.

[54] H. Khani, N. S. Grundish, D. O. Wipf, J. B. Goodenough, *Adv. Energy Mater.* **2019**, *10*, 1903215.

[55] H. Sun, Y. B. Lian, C. Yang, L. K. Xiong, P. W. Qi, Q. Q. Mu, X. H. Zhao, J. Guo, Z. Deng, Y. Peng, *Energy Environ. Sci.* **2018**, *11*, 2363.

[56] Y. Tong, J. C. Wu, P. Z. Chen, H. F. Liu, W. S. Chu, C. Z. Wu, Y. Xie, *J. Am. Chem. Soc.* **2018**, *140*, 11165.

[57] J. F. Zhang, J. Y. Liu, L. F. Xi, Y. F. Yu, N. Chen, S. H. Sun, W. C. Wang, K. M. Lange, B. Zhang, *J. Am. Chem. Soc.* **2018**, *140*, 3876.

[58] H. M. Sun, X. B. Xu, Z. H. Yan, X. Chen, F. Y. Cheng, P. S. Weiss, J. Chen, *Chem. Mater.* **2017**, *29*, 8539.

[59] Y. Z. Li, Z. Wang, J. Hu, S. W. Li, Y. C. Du, X. J. Han, P. Xu, *Adv. Funct. Mater.* **2020**, *30*, 1910498.

[60] Y. B. Li, C. Zhao, *Chem. Mater.* **2016**, *28*, 5659.

[61] J. W. Huang, Y. H. Sun, Y. D. Zhang, G. F. Zou, C. Y. Yan, S. Cong, T. Y. Lei, X. Dai, J. Guo, R. F. Lu, Y. R. Li, J. Xiong, *Adv. Mater.* **2018**, *30*, 1705045.

[62] F. F. Guo, Y. Y. Wu, H. Chen, Y. P. Liu, L. Yang, X. Ai, X. X. Zou, *Energy Environ. Sci.* **2019**, *12*, 684.

[63] J. Masa, P. Weide, D. Peeters, I. Sinev, W. Xia, Z. Y. Sun, C. Somsen, M. Muhler, W. Schuhmann, *Adv. Energy Mater.* **2016**, *6*, 1502313.

[64] H. Ren, X. L. Sun, C. F. Du, J. Zhao, D. B. Liu, W. Fang, S. Kumar, R. Chua, S. Z. Meng, P. Kidkhunthod, L. Song, S. Q. Li, S. Madhavi, Q. Y. Yan, *ACS Nano* **2019**, *13*, 12969.

[65] K. Xu, H. Ding, H. F. Lv, S. Tao, P. Z. Chen, X. J. Wu, W. S. Chu, C. Z. Wu, Y. Xie, *ACS Catal.* **2016**, *7*, 310.

[66] M. Zhou, Q. H. Weng, X. Y. Zhang, X. Wang, Y. M. Xue, X. H. Zeng, Y. Bando, D. Golberg, *J. Mater. Chem. A* **2017**, *5*, 4335.

[67] K. Fan, H. Y. Zou, Y. Lu, H. Chen, F. S. Li, J. X. Liu, L. C. Sun, L. P. Tong, M. F. Toney, M. L. Sui, J. G. Yu, *ACS Nano* **2018**, *12*, 12369.

[68] X. X. Zou, Y. Y. Wu, Y. P. Liu, D. P. Liu, W. Li, L. Gu, H. Liu, P. W. Wang, L. Sun, Y. Zhang, *Chem* **2018**, *4*, 1139.

[69] Q. Z. Xiong, Y. Wang, P.-F. Liu, L.-R. Zheng, G. Z. Wang, H.-G. Yang, P.-K. Wong, H. M. Zhang, H. J. Zhao, *Adv. Mater.* **2018**, *30*, 1801450.

[70] K. Xu, H. Ding, H. F. Lv, P. Z. Chen, X. L. Lu, H. Cheng, T. P. Zhou, S. Liu, X. J. Wu, C. Z. Wu, Y. Xie, *Adv. Mater.* **2016**, *28*, 3326.

[71] L. Yu, Q. Zhu, S. W. Song, B. McElhenny, D. Z. Wang, C. Z. Wu, Z. J. Qin, J. M. Bao, Y. Yu, S. Chen, Z. F. Ren, *Nat. Commun.* **2019**, *10*, 5106.

[72] Y. Q. Zhang, B. Ouyang, J. Xu, G. C. Jia, S. Chen, R. S. Rawat, H. J. Fan, *Angew. Chem., Int. Ed.* **2016**, *55*, 8670.

[73] Q. Z. Qian, Y. P. Li, Y. Liu, L. Yu, G. Q. Zhang, *Adv. Mater.* **2019**, *31*, 1901139.

[74] Z. Q. Xue, K. Liu, Q. L. Liu, Y. L. Li, M. R. Li, C.-Y. Su, N. Ogiwara, H. Kobayashi, H. Kitagawa, M. Liu, G. Q. Li, *Nat. Commun.* **2019**, *10*, 5048.

[75] K. Rui, G. Q. Zhao, Y. P. Chen, Y. Lin, Q. Zhou, J. Y. Chen, J. X. Zhu, W. P. Sun, W. Huang, S. X. Dou, *Adv. Funct. Mater.* **2018**, *28*, 1801554.

[76] Z.-Q. Huang, B. Wang, D.-S. Pan, L.-L. Zhou, Z.-H. Guo, J.-L. Song, *ChemSusChem* **2020**, *13*, 2564.

[77] Z.-Y. Yu, Y. Duan, J.-D. Liu, Y. Chen, X.-K. Liu, W. Liu, T. Ma, Y. Li, X.-S. Zheng, T. Yao, M.-R. Gao, J. F. Zhu, B.-J. Ye, S.-H. Yu, *Nat. Commun.* **2019**, *10*, 2799.

[78] X. Z. Su, Y. Wang, J. Zhou, S. Q. Gu, J. Li, S. Zhang, *J. Am. Chem. Soc.* **2018**, *140*, 11286.

[79] W. Ahn, M. G. Park, D. U. Lee, M. H. Seo, G. Jiang, Z. P. Cano, F. M. Hassan, Z. W. Chen, *Adv. Funct. Mater.* **2018**, *28*, 1802129.

[80] J. Zhou, Y. Wang, X. Z. Su, S. Q. Gu, R. D. Liu, Y. B. Huang, S. Yan, J. Li, S. Zhang, *Energy Environ. Sci.* **2019**, *12*, 739.

[81] W. X. Zhang, H. Song, Y. Cheng, C. Liu, C. H. Wang, M. A. N. Khan, H. Zhang, J. Z. Liu, C. Z. Yu, L. J. Wang, J. S. Li, *Adv. Sci.* **2019**, *6*, 1801901.

[82] P. W. Menezes, A. Indra, I. Zaharieva, C. Walter, S. Loos, S. Hoffmann, R. Schlögl, H. Dau, M. Driess, *Energy Environ. Sci.* **2019**, *12*, 988.

[83] T. Wang, H. Chen, Z. Z. Yang, J. Y. Liang, S. Dai, *J. Am. Chem. Soc.* **2020**, *142*, 4550.

[84] B. Song, K. Li, Y. Yin, T. Wu, L. N. Dang, M. Cabán-Acevedo, J. C. Han, T. L. Gao, X. J. Wang, Z. H. Zhang, J. R. Schmidt, P. Xu, S. Jin, *ACS Catal.* **2017**, *7*, 8549.

[85] Y. M. Shi, Y. Yu, Y. Liang, Y. H. Du, B. Zhang, *Angew. Chem., Int. Ed.* **2019**, *58*, 3769.

[86] S. N. Zhao, J. F. Huang, Y. Y. Liu, J. H. Shen, H. Wang, X. L. Yang, Y. H. Zhu, C. Z. Li, *J. Mater. Chem. A* **2017**, *5*, 4207.

[87] X. Liu, K. Ni, B. Wen, C. J. Niu, J. S. Meng, R. T. Guo, Q. Li, J. T. Li, Y. W. Zhu, X. J. Wu, D. Y. Zhao, L. Q. Mai, *J. Mater. Chem. A* **2018**, *6*, 17874.

[88] J. Deng, P. J. Ren, D. H. Deng, X. H. Bao, *Angew. Chem., Int. Ed.* **2015**, *54*, 2100.

[89] C. H. Wang, H. C. Yang, Y. J. Zhang, Q. B. Wang, *Angew. Chem., Int. Ed.* **2019**, *58*, 6099.

[90] X. J. Cui, P. J. Ren, D. H. Deng, J. Deng, X. H. Bao, *Energy Environ. Sci.* **2016**, *9*, 123.

[91] J. Masa, W. Schuhmann, *ChemCatChem* **2019**, *11*, 5842.

[92] H. P. Wang, J. Wang, Y. C. Pi, Q. Shao, Y. M. Tan, X. Q. Huang, *Angew. Chem., Int. Ed.* **2019**, *58*, 2316.

[93] E. Fabbri, M. Nachtegaal, T. Binninger, X. Cheng, B. -J. Kim, J. Durst, F. Bozza, T. Graule, R. Schaublin, L. Wiles, M. Pertoso, N. Danilovic, K. E. Ayers, T. J. Schmidt, *Nat. Mater.* **2017**, *16*, 925.

[94] B. C. Weng, F. H. Xu, C. L. Wang, W. W. Meng, C. R. Grice, Y. F. Yan, *Energy Environ. Sci.* **2017**, *10*, 121.

[95] C.-W. Tung, Y.-Y. Hsu, Y.-P. Shen, Y. X. Zheng, T.-S. Chan, H.-S. Sheu, Y.-C. Cheng, H. M. Chen, *Nat. Commun.* **2015**, *6*, 8106.

[96] A. Bergmann, E. Martinez-Moreno, D. Teschner, P. Chernev, M. Gliech, J. F. de Araujo, T. Reier, H. Dau, P. Strasser, *Nat. Commun.* **2015**, *6*, 8625.

[97] Z. H. Xiao, Y.-C. Huang, C.-L. Dong, C. Xie, Z. J. Liu, S. Q. Du, W. Chen, D. F. Yan, L. Tao, Z. W. Shu, G. H. Zhang, H. G. Duan, Y. Y. Wang, Y. Q. Zou, R. Chen, S. Y. Wang, *J. Am. Chem. Soc.* **2020**, *142*, 12087.

[98] S. N. Sun, Y. M. Sun, Y. Zhou, S. B. Xi, X. Ren, B. C. Huang, H. B. Liao, L. P. Wang, Y. H. Du, Z. C. J. Xu, *Angew. Chem., Int. Ed.* **2019**, *58*, 6042.

[99] H.-Y. Wang, S.-F. Hung, H. -Y. Chen, T.-S. Chan, H. M. Chen, B. Liu, *J. Am. Chem. Soc.* **2016**, *138*, 36.

[100] Y. Duan, Z.-Y. Yu, S.-J. Hu, X.-S. Zheng, C.-T. Zhang, H.-H. Ding, B.-C. Hu, Q.-Q. Fu, Z.-L. Yu, X. Zheng, J.-F. Zhu, M.-R. Gao, S.-H. Yu, *Angew. Chem., Int. Ed.* **2019**, *58*, 15772.

[101] S. W. Lee, C. Carlton, M. Risch, Y. Surendranath, S. Chen, S. Furutsuki, A. Yamada, D. G. Nocera, Y. Shao-Horn, *J. Am. Chem. Soc.* **2012**, *134*, 16959.

[102] K. Y. Zhu, T. Wu, Y. Zhu, X. N. Li, M. R. Li, R. F. Lu, J. H. Wang, X. F. Zhu, W. S. Yang, *ACS Energy Lett.* **2017**, *2*, 1654.

[103] X. M. Xu, W. Wang, W. Zhou, Z. P. Shao, *Small Methods* **2018**, *2*, 1800071.

[104] B.-J. Kim, E. Fabbri, D. F. Abbott, X. Cheng, A. H. Clark, M. Nachtegaal, M. Borlaf, I. E. Castelli, T. Graule, T. J. Schmidt, *J. Am. Chem. Soc.* **2019**, *141*, 5231.

[105] C. H. Zhao, N. Li, R. Z. Zhang, Z. Q. Zhu, J. H. Lin, K. F. Zhang, C. J. Zhao, *ACS Appl. Mater. Interfaces* **2019**, *11*, 47858.

[106] Y. L. Zhu, H. A. Tahini, Z. W. Hu, Z.-G. Chen, W. Zhou, A. C. Komarek, Q. Lin, H.-J. Lin, C.-T. Chen, Y. J. Zhong, M. T. Fernandez-Diaz, S. C. Smith, H. T. Wang, M. L. Liu, Z. P. Shao, *Adv. Mater.* **2020**, *32*, 1905025.

[107] Z. Y. Lu, W. W. Xu, W. Zhu, Q. Yang, X. D. Lei, J. F. Liu, Y. P. Li, X. M. Sun, X. Duan, *Chem. Commun.* **2014**, *50*, 6479.

[108] D. Friebel, M. W. Louie, M. Bajdich, K. E. Sanwald, Y. Cai, A. M. Wise, M.-J. Cheng, D. Sokaras, T.-C. Weng, R. Alonso-Mori, R. C. Davis, J. R. Bargar, J. K. Nørskov, A. Nilsson, A. T. Bell, *J. Am. Chem. Soc.* **2015**, *137*, 1305.

[109] J. S. Kim, B. Kim, H. Kim, K. Kang, *Adv. Energy Mater.* **2018**, *8*, 1702774.

[110] L. Lv, Z. X. Yang, K. Chen, C. D. Wang, Y. J. Xiong, *Adv. Energy Mater.* **2019**, *9*, 1803060.

[111] X. -Y. Yu, Y. Feng, B. Y. Guan, X. W. Lou, U. Paik, *Energy Environ. Sci.* **2016**, *9*, 1246.

[112] W. Li, D. H. Xiong, X. F. Gao, L. F. Liu, *Chem. Commun.* **2019**, *55*, 8744.

[113] L. S. Peng, S. S. A. Shah, Z. D. Wei, *Chin. J. Catal.* **2018**, *39*, 1575.

[114] Y. Li, Z. H. Dong, L. F. Jiao, *Adv. Energy Mater.* **2019**, *10*, 1902104.

[115] F. Yu, H. Q. Zhou, Y. F. Huang, J. Y. Sun, F. Qin, J. M. Bao, W. A. GoddardIII, S. Chen, Z. F. Ren, *Nat. Commun.* **2018**, *9*, 2551.

[116] W. W. Zou, C. L. Sun, K. N. Zhao, J. T. Li, X. L. Pan, D. X. Ye, Y. P. Xie, W. W. Xu, H. B. Zhao, L. Zhang, J. J. Zhang, *Electrochim. Acta* **2020**, *345*, 136114,.

[117] Y. Y. Jiang, Y. Z. Lu, J. Y. Lin, X. Wang, Z. X. Shen, *Small Methods* **2018**, *2*, 1700369.

[118] H. Zhao, Z.-Y. Yuan, *ChemCatChem* **2020**, *12*, 3797.

[119] J. Qi, Y.-P. Lin, D. D. Chen, T. H. Zhou, W. Zhang, R. Cao, *Angew. Chem., Int. Ed.* **2020**, *59*, 8917.

[120] K. Jin, J. Park, J. Lee, K. D. Yang, G. K. Pradhan, U. Sim, D. Jeong, H. L. Jang, S. Park, D. Kim, N.-E. Sung, S. H. Kim, S. Han, K. T. Nam, *J. Am. Chem. Soc.* **2014**, *136*, 7435.

[121] C. C. Lv, S. C. Xu, Q. P. Yang, Z. P. Huang, C. Zhang, *J. Mater. Chem. A* **2019**, *7*, 12457.

[122] S. Sultan, M. Ha, D. Y. Kim, J. N. Tiwari, C. W. Myung, A. Meena, T. J. Shin, K. H. Chae, K. S. Kim, *Nat. Commun.* **2019**, *10*, 5195.

[123] Y. Gershinsky, D. Zitoun, *ACS Catal.* **2018**, *8*, 8715.

[124] P. L. Zhang, M. Wang, Y. Yang, T. Y. Yao, H. X. Han, L. C. Sun, *Nano Energy* **2016**, *19*, 98.

[125] X. Ai, X. Zou, H. Chen, Y. T. Su, X. L. Feng, Q. J. Li, Y. P. Liu, Y. Zhang, X. X. Zou, *Angew. Chem., Int. Ed.* **2020**, *59*, 3961.

[126] W.-J. Jiang, S. Niu, T. Tang, Q.-H. Zhang, X.-Z. Liu, Y. Zhang, Y.-Y. Chen, J.-H. Li, L. Gu, L.-J. Wan, J.-S. Hu, *Angew. Chem., Int. Ed.* **2017**, *56*, 6572.

[127] P. Z. Chen, K. Xu, T. P. Zhou, Y. Tong, J. C. Wu, H. Cheng, X. L. Lu, H. Ding, C. Z. Wu, Y. Xie, *Angew. Chem., Int. Ed.* **2016**, *55*, 2488.

[128] W. N. Zhao, T. Xu, T. Li, Y. K. Wang, H. Liu, J. Z. Feng, S. J. Ding, Z. T. Li, M. B. Wu, *Small* **2018**, *14*, 1802829.

[129] J. Jiang, S. Lu, W.-K. Wang, G.-X. Huang, B.-C. Huang, F. Zhang, Y.-J. Zhang, H.-Q. Yu, *Nano Energy* **2018**, *43*, 300.

[130] G.-F. Chen, T. Y. Ma, Z.-Q. Liu, N. Li, Y.-Z. Su, K. Davey, S.-Z. Qiao, *Adv. Funct. Mater.* **2016**, *26*, 3314.

[131] R. Gao, H. Zhang, D. P. Yan, *Nano Energy* **2017**, *31*, 90.

**ADVANCED
SCIENCE NEWS**

www.advancedsciencenews.com

**ADVANCED
MATERIALS**

www.advmat.de

[132] Y. Xiao, T. Hu, X. Zhao, F. X. Hu, H. B. Yang, C. M. Li, *Nano Energy* **2020**, *75*, 104949.

[133] O. Mabayoje, A. Shoola, B. R. Wygant, C. B. Mullins, *ACS Energy Lett.* **2016**, *1*, 195.

[134] Y. P. Zhu, H.-C. Chen, C.-S. Hsu, T.-S. Lin, C.-J. Chang, S.-C. Chang, L.-D. Tsai, H. M. Chen, *ACS Energy Lett.* **2019**, *4*, 987.

[135] W. Chen, H. T. Wang, Y. Z. Li, Y. Y. Liu, J. Sun, S. Lee, J.-S. Lee, Y. Cui, *ACS Cent. Sci.* **2015**, *1*, 244.

[136] W. Chen, Y. Y. Liu, Y. Z. Li, J. Sun, Y. C. Qiu, C. Liu, G. M. Zhou, Y. Cui, *Nano Lett.* **2016**, *16*, 7588.

[137] C. Tang, N. Y. Cheng, Z. H. Pu, W. Xing, X. P. Sun, *Angew. Chem., Int. Ed.* **2015**, *54*, 9351.

[138] J. N. Xing, Y. Li, S. W. Guo, T. Jin, H. X. Li, Y. J. Wang, L. F. Jiao, *Electrochim. Acta* **2019**, *298*, 305.

[139] M. Shalom, D. Ressnig, X. F. Yang, G. Clavel, T. P. Fellinger, M. Antonietti, *J. Mater. Chem. A* **2015**, *3*, 8171.

[140] C. L. Zhu, Z. X. Yin, W. H. Lai, Y. Sun, L. N. Liu, X. T. Zhang, Y. J. Chen, S.-L. Chou, *Adv. Energy Mater.* **2018**, *8*, 1802327.

[141] F. Z. Song, W. Li, J. Q. Yang, G. Q. Han, P. L. Liao, Y. J. Sun, *Nat. Commun.* **2018**, *9*, 4531.

[142] Y. Wang, Y. Sun, F. Yan, C. L. Zhu, P. Gao, X. T. Zhang, Y. J. Chen, *J. Mater. Chem. A* **2018**, *6*, 8479.

[143] K. Xu, P. Z. Chen, X. L. Li, Y. Tong, H. Ding, X. J. Wu, W. S. Chu, Z. M. Peng, C. Z. Wu, Y. Xie, *J. Am. Chem. Soc.* **2015**, *137*, 4119.

[144] C. Walter, P. W. Menezes, S. Orthmann, J. Schuch, P. Connor, B. Kaiser, M. Lerch, M. Driess, *Angew. Chem., Int. Ed.* **2018**, *57*, 698.

[145] S. Yuan, L. Feng, K. C. Wang, J. D. Pang, M. Bosch, C. Lollar, Y. J. Sun, J. S. Qin, X. Y. Yang, P. Zhang, Q. Wang, L. F. Zou, Y. M. Zhang, L. L. Zhang, Y. Fang, J. L. Li, H.-C. Zhou, *Adv. Mater.* **2018**, *30*, 1704303.

[146] J. S. Meng, X. Liu, C. J. Niu, Q. Pang, J. T. Li, F. Liu, Z. A. Liu, L. Q. Mai, *Chem. Soc. Rev.* **2020**, *49*, 3142.

[147] H. B. Aiyappa, J. Masa, C. Andronescu, M. Muhler, R. A. Fischer, W. Schuhmann, *Small Methods* **2019**, *3*, 1800415.

[148] X.-F. Lu, P.-Q. Liao, J.-W. Wang, J.-X. Wu, X.-W. Chen, C.-T. He, J.-P. Zhang, G.-R. Li, X.-M. Chen, *J. Am. Chem. Soc.* **2016**, *138*, 8336.

[149] X.-L. Wang, L.-Z. Dong, M. Qiao, Y.-J. Tang, J. Liu, Y. F. Li, S.-L. Li, J.-X. Su, Y.-Q. Lan, *Angew. Chem., Int. Ed.* **2018**, *57*, 9660.

[150] W.-J. Li, C. Han, G. Cheng, S.-L. Chou, H.-K. Liu, S.-X. Dou, *Small* **2019**, *15*, 1900470.

[151] Y. W. Li, J. T. Hu, K. Yang, B. Cao, Z. B. Li, L. Y. Yang, F. Pan, *Mater. Today Energy* **2019**, *14*, 100332.

[152] Z. W. Zhuang, Y. Wang, C. -Q. Xu, S. J. Liu, C. Chen, Q. Peng, Z. B. Zhuang, H. Xiao, Y. Pan, S. Lu, R. Yu, W.-C. Cheong, X. Cao, K. L. Wu, K. A. Sun, Y. Wang, D. S. Wang, J. Li, Y. D. Li, *Nat. Commun.* **2019**, *10*, 4875.

[153] J. J. Gao, C.-Q. Xu, S. -F. Hung, W. Liu, W. Z. Cai, Z. P. Zeng, C. M. Jia, H. M. Chen, H. Xiao, J. Li, Y. Q. Huang, B. Liu, *J. Am. Chem. Soc.* **2019**, *141*, 3014.

[154] H. N. Nong, T. Reier, H.-S. Oh, M. Gliech, P. Paciok, T. H. T. Vu, D. Teschner, M. Heggen, V. Petkov, R. Schlögl, T. Jones, P. Strasser, *Nat. Catal.* **2018**, *1*, 841.

[155] R. H. Zhang, N. Dubouis, M. B. Osman, W. Yin, M. T. Sougrati, D. A. D. Corte, D. Giaume, A. Grimaud, *Angew. Chem., Int. Ed.* **2019**, *58*, 4571.

[156] A. Grimaud, A. Demortière, M. Saubanère, W. Dachraoui, M. Duchamp, M.-L. Doublet, J.-M. Tarascon, *Nat. Energy* **2016**, *2*, 16189.

[157] Z. Y. Jin, J. Lv, H. L. Jia, W. H. Liu, H. L. Li, Z. H. Chen, X. Lin, G. Q. Xie, X. J. Liu, S. H. Sun, H.-J. Qiu, *Small* **2019**, *15*, 1904180.

[158] G. Wu, X. S. Zheng, P. X. Cui, H. Y. Jiang, X. Q. Wang, Y. T. Qu, W. X. Chen, Y. Lin, H. Li, X. Han, Y. M. Hu, P. G. Liu, Q. H. Zhang, J. J. Ge, Y. C. Yao, R. B. Sun, Y. Wu, L. Gu, X. Hong, Y. D. Li, *Nat. Commun.* **2019**, *10*, 4855.

[159] X. Liang, L. Shi, Y. P. Liu, H. Chen, R. Si, W. S. Yan, Q. Zhang, G.-D. Li, L. Yang, X. X. Zou, *Angew. Chem., Int. Ed.* **2019**, *58*, 7631.

[160] M. Blasco-Ahicart, J. Soriano-Lopez, J. J. Carbo, J. M. Poblet, J. R. Galan-Mascaros, *Nat. Chem.* **2018**, *10*, 24.

[161] M. Chatti, J. L. Gardiner, M. Fournier, B. Johannessen, T. Williams, T. R. Gengenbach, N. Pai, C. Nguyen, D. R. MacFarlane, R. K. Hocking, A. N. Simonov, *Nat. Catal.* **2019**, *2*, 457.

[162] Z. M. Chan, D. A. Kitchaev, J. N. Weker, C. Schnedermann, K. Lim, G. Ceder, W. Tumas, M. F. Toney, D. G. Nocera, *Proc. Natl. Acad. Sci. USA* **2018**, *115*, E5261.

[163] R. Kötz, H. Neff, S. Stucki, *J. Electrochem. Soc.* **1984**, *131*, 72.

[164] L. C. Seitz, C. F. Dickens, K. Nishio, Y. Hikita, J. Montoya, A. Doyle, C. Kirk, A. Vojvodic, H. Y. Hwang, J. K. Nørskov, T. F. Jaramillo, *Science* **2016**, *353*, 1011.

[165] Z. Y. Lu, K. Jiang, G. X. Chen, H. T. Wang, Y. Cui, *Adv. Mater.* **2018**, *30*, 1800978.

[166] S. Anantharaj, V. Aravindan, *Adv. Energy Mater.* **2019**, *10*, 1902666.

[167] X. Ren, R. X. Ge, Y. Zhang, D. N. Liu, D. Wu, X. Sun, B. Du, Q. Wei, *J. Mater. Chem. A* **2017**, *5*, 7291.

[168] Y. Shao, X. Xiao, Y.-P. Zhu, T.-Y. Ma, *Angew. Chem., Int. Ed.* **2019**, *58*, 14599.

[169] K. Xu, H. Cheng, L. Q. Liu, H. F. Lv, X. J. Wu, C. Z. Wu, Y. Xie, *N.Lett.* **2017**, *17*, 578.

[170] S. Pintado, S. Goberna-Ferrón, E. C. Escudero-Adán, J. R. Galán-Mascarós, *J. Am. Chem. Soc.* **2013**, *135*, 13270.

[171] Q. He, Y. Wan, H. Jiang, Z. Pan, C. Wu, M. Wang, X. Wu, B. Ye, P. M. Ajayan, L. Song, *ACS Energy Lett.* **2018**, *3*, 1373.

[172] Z. Y. Lu, H. T. Wang, D. S. Kong, K. Yan, P.-C. Hsu, G. Y. Zheng, H. B. Yao, Z. Liang, X. M. Sun, Y. Cui, *Nat. Commun.* **2014**, *5*, 4345.

[173] Z. H. Zou, T. T. Wang, X. H. Zhao, W.-J. Jiang, H. R. Pan, D. Q. Gao, C. L. Xu, *ACS Catal.* **2019**, *9*, 7356.

[174] L. J. Han, P. Y. Tang, Á. Reyes-Carmona, B. Rodríguez-García, M. Torréns, J. R. Morante, J. Arbiol, J. R. Galan-Mascaros, *J. Am. Chem. Soc.* **2016**, *138*, 16037.

[175] W. Z. Cai, R. Chen, H. B. Yang, H. B. Tao, H.-Y. Wang, J. J. Gao, W. Liu, S. Liu, S-F. Hung, B. Liu, *Nano Lett.* **2020**, *20*, 4278.

[176] Y. K. Zhang, C. Q. Wu, H. L. Jiang, Y. X. Lin, H. J. Liu, Q. He, S. M. Chen, T. Duan, L. Song, *Adv. Mater.* **2018**, *30*, 1707522.

[177] Y. Y. Wu, Y. P. Liu, G.-D. Li, X. Zou, X. R. Lian, D. J. Wang, L. Sun, T. Asefa, X. X. Zou, *Nano Energy* **2017**, *35*, 161.

[178] X. T. Han, C. Yu, Y. Y. Niu, Z. Wang, Y. B. Kang, Y. W. Ren, H. Wang, H. S. Park, J. S. Qiu, *Small Methods* **2020**, *4*, 2000546.

[179] T. L. Zhou, C. H. Wang, Y. M. Shi, Y. Liang, Y. F. Yu, B. Zhang, *J. Mater. Chem. A* **2020**, *8*, 1631.

[180] Q. R. Shi, C. Z. Zhu, D. Du, Y. H. Lin, *Chem. Soc. Rev.* **2019**, *48*, 3181.

[181] A. Dutta, N. Pradhan, *J. Phys. Chem. Lett.* **2017**, *8*, 144.

[182] K. Feng, D. Zhang, F. F. Liu, H. Li, J. B. Xu, Y. J. Xia, Y. Y. Li, H. P. Lin, S. A. Wang, M. W. Shao, Z. H. Kang, J. Zhong, *Adv. Energy Mater.* **2020**, *10*, 2000184.

[183] M. Görlin, J. Ferreira de Araujo, H. Schmies, D. Bernsmeier, S. Dresp, M. Gliech, Z. Jusys, P. Chernev, R. Kraehnert, H. Dau, P. Strasser, *J. Am. Chem. Soc.* **2017**, *139*, 2070.

[184] O. Diaz-Morales, D. Ferrus-Suspedra, M. T. M. Koper, *Chem. Sci.* **2016**, *7*, 2639.

[185] J. B. Gerken, J. G. McAlpin, J. Y. C. Chen, M. L. Rigsby, W. H. Casey, R. D. Britt, S. S. Stahl, *J. Am. Chem. Soc.* **2011**, *133*, 14431.

[186] B. J. Trzesniewski, O. Diaz-Morales, D. A. Vermaas, A. Longo, W. Bras, M. T. Koper, W. A. Smith, *J. Am. Chem. Soc.* **2015**, *137*, 15112.

[187] W. H. Ren, M. S. Qin, Z. X. Zhu, M. Y. Yan, Q. Li, L. Zhang, D. N. Liu, L. Q. Mai, *Nano Lett.* **2017**, *17*, 4713.

[188] X. Liu, C. J. Niu, J. S. Meng, X. M. Xu, X. P. Wang, B. Wen, R. T. Guo, L. Q. Mai, *J. Mater. Chem. A* **2016**, *4*, 14095.

[189] L. Q. He, W. B. Zhang, Q. J. Mo, W. J. Huang, L. C. Yang, Q. S. Gao, *Angew. Chem., Int. Ed.* **2020**, *59*, 3544.

[190] C. Y. Hu, Q. Y. Ma, S-F. Hung, Z.-N. Chen, D. H. Ou, B. Ren, H. M. Chen, G. Fu, N. F. Zheng, *Chem* **2017**, *3*, 122.

2007344 (32 of 34)

[191] X. Y. Li, L. P. Xiao, L. Zhou, Q. C. Xu, J. Weng, J. Xu, B. Liu, *Angew. Chem., Int. Ed.* **2020**, *59*, 21106.

[192] S. Anantharaj, H. Sugime, S. Noda, *Chem. Eng. J.* **2020**, *8*, 127275.

[193] Z. Weng, Y. S. Wu, M. Y. Wang, J. B. Jiang, K. Yang, S. J. Huo, X.-F. Wang, Q. Ma, G. W. Brudvig, V. S. Batista, Y. Y. Liang, Z. X. Feng, H. L. Wang, *Nat. Commun.* **2018**, *9*, 415.

[194] D. Kim, C. S. Kley, Y. F. Li, P. D. Yang, *Proc. Natl. Acad. Sci. USA* **2017**, *114*, 10560.

[195] M. Favaro, H. Xiao, T. Cheng, W. A. GoddardIII, J. Yano, E. J. Crumlin, *Proc. Natl. Acad. Sci. USA* **2017**, *114*, 6706.

[196] H. Xiao, W. A. GoddardIII, T. Cheng, Y. Y. Liu, *Proc. Natl. Acad. Sci. USA* **2017**, *114*, E7045.

[197] A. Zhang, Y. X. Liang, H. P. Li, B. Y. Zhang, Z. H. Liu, Q. X. Chang, H. Zhang, C.-F. Zhu, Z. G. Geng, W. G. Zhu, J. Zeng, *Nano Lett.* **2020**, *20*, 8229.

[198] Z. W. Seh, J. Kibsgaard, C. F. Dickens, I. Chorkendorff, J. K. Nørskov, T. F. Jaramillo, *Science* **2017**, *355*, eaad4998.

[199] P. De Luna, C. Hahn, D. Higgins, S. A. Jaffer, T. F. Jaramillo, E. H. Sargent, *Science* **2019**, *364*, eaav3506.

[200] O. S. Bushuyev, P. De Luna, C. T. Dinh, L. Tao, G. Saur, J. van de Lagemaat, S. O. Kelley, E. H. Sargent, *Joule* **2018**, *2*, 825.

[201] S. X. Ren, D. Joulié, D. Salvatore, K. Torbensen, M. Wang, M. Robert, C. P. Berlinguette, *Science* **2019**, *365*, 367.

[202] J. Gu, C.-S. Hsu, L. C. Bai, H. M. Chen, X. L. Hu, *Science* **2019**, *364*, 1091.

[203] C. Xia, P. Zhu, Q. Jiang, Y. Pan, W. T. Liang, E. Stavitski, H. N. Alshareef, H. T. Wang, *Nat. Energy* **2019**, *4*, 776.

[204] N. Han, Y. Wang, H. Yang, J. Deng, J. H. Wu, Y. F. Li, Y. G. Li, *Nat. Commun.* **2018**, *9*, 1320.

[205] H. C. Zhang, X. X. Chang, J. G. G. Chen, W. A. GoddardIII, B. J. Xu, M.-J. Cheng, Q. Lu, *Nat. Commun.* **2019**, *10*, 3340.

[206] Y. S. Wu, Z. Jiang, X. Lu, Y. Y. Liang, H. L. Wang, *Nature* **2019**, *575*, 639.

[207] W. R. Leow, Y. W. Lum, A. Ozden, Y. H. Wang, D.-H. Nam, B. Chen, J. Wicks, T.-T. Zhuang, F. W. Li, D. Sinton, W. H. Sargent, *Science* **2020**, *368*, 1228.

[208] C.-T. Dinh, T. Burdyny, M. G. Kibria, A. Seifitokaldani, C. M. Gabardo, F. P. García de Arquer, A. Kiani, J. P. Edwards, P. D. Luna, O. S. Bushuyev, C. Q. Zou, R. Quintero-Bermudez, Y. J. Pang, D. Sinton, E. H. Sargent, *Science* **2018**, *360*, 783.

[209] X. Wang, Z. Y. Wang, F. P. García de Arquer, C.-T. Dinh, A. Ozden, Y. G. C. Li, D.-H. Nam, J. Li, Y.-S. Liu, J. Wicks, Z. T. Chen, M. F. Chi, B. Chen, Y. Wang, J. Tam, J. Y. Howe, A. Proppe, P. Todorović, F. W. Li, T.-T. Zhuang, C. M. Gabardo, A. R. Kirmani, C. McCallum, S.-F. Hung, Y. Lum, M. C. Luo, Y. M. Min, A. Xu, C. P. O'Brien, B. Stephen, B. Sun, A. H. Ip, L. J. Richter, S. O. Kelley, D. Sinton, E. H. Sargent, *Nat. Energy* **2020**, *5*, 478.

[210] Y. H. Chen, C. W. Li, M. W. Kanan, *J. Am. Chem. Soc.* **2012**, *134*, 19969.

[211] D. Bohra, I. Ledezma-Yanez, G. N. Li, W. de Jong, E. A. Pidko, W. A. Smith, *Angew. Chem., Int. Ed.* **2019**, *58*, 1345.

[212] H. B. Yang, S.-F. Hung, S. Liu, K. D. Yuan, S. Miao, L. P. Zhang, X. Huang, H.-Y. Wang, W. Z. Cai, R. Chen, J. J. Gao, X. F. Yang, W. Chen, Y. Q. Huang, H. M. Chen, C. M. Li, T. Zhang, B. Liu, *Nat. Energy* **2018**, *3*, 140.

[213] Q. F. Gong, P. Ding, M. Q. Xu, X. R. Zhu, M. Y. Wang, J. Deng, Q. Ma, N. Han, Y. Zhu, J. Lu, Z. X. Feng, Y. F. Li, W. Zhou, Y. G. Li, *Nat. Commun.* **2019**, *10*, 2807.

[214] X. L. Zheng, P. De Luna, F. P. García de Arquer, B. Zhang, N. Becknell, M. B. Ross, Y. F. Li, M. N. Banis, Y. Z. Li, M. Liu, O. Voznyy, C. T. Dinh, T. T. Zhuang, P. Stadler, Y. Cui, X. W. Du, P. D. Yang, E. H. Sargent, *Joule* **2017**, *1*, 794.

[215] Y. Zhou, R. Zhou, X. R. Zhu, N. Han, B. Song, T. C. Liu, G. Z. Hu, Y. F. Li, J. Lu, Y. G. Li, *Adv. Mater.* **2020**, *32*, 2000992.

[216] P. De Luna, R. Quintero-Bermudez, C.-T. Dinh, M. B. Ross, O. S. Bushuyev, P. Todorović, T. Regier, S. O. Kelley, P. D. Yang, E. H. Sargent, *Nat. Catal.* **2018**, *1*, 103.

[217] K. Jiang, R. B. Sandberg, A. J. Akey, X. Y. Liu, D. C. Bell, J. K. Nørskov, K. R. Chan, H. T. Wang, *Nat. Catal.* **2018**, *1*, 111.

[218] B. An, Z. Li, Y. Song, J. Z. Zhang, L. Z. Zeng, C. Wang, W. B. Lin, *Nat. Catal.* **2019**, *2*, 709.

[219] M. G. Kibria, C.-T. Dinh, A. Seifitokaldani, P. De Luna, T. Burdyny, R. Quintero-Bermudez, M. B. Ross, O. S. Bushuyev, F. P. Garcia de Arquer, P. D. Yang, D. Sinton, E. H. Sargent, *Adv. Mater.* **2018**, *30*, 1804867.

[220] T.-T. Zhuang, Z.-Q. Liang, A. Seifitokaldani, Y. Li, P. De Luna, T. Burdyny, F. L. Che, F. Meng, Y. M. Min, R. Quintero-Bermudez, C. T. Dinh, Y. J. Pang, M. Zhong, B. Zhang, J. Li, P.-N. Chen, X.-L. Zheng, H. Y. Liang, W.-N. Ge, B.-J. Ye, D. Sinton, S.-H. Yu, E. H. Sargent, *Nat. Catal.* **2018**, *1*, 421.

[221] D.-H. Nam, O. S. Bushuyev, J. Li, P. De Luna, A. Seifitokaldani, C.-T. Dinh, F. P. Garcia de Arquer, Y. H. Wang, Z. Q. Liang, A. H. Proppe, C. S. Tan, P. Todorovic, O. Shekhah, C. M. Gabardo, J. W. Jo, J. Choi, M.-J. Choi, S.-W. Baek, J. Kim, D. Sinton, S. O. Kelley, M. Eddaoudi, E. H. Sargent, *J. Am. Chem. Soc.* **2018**, *140*, 11378.

[222] S. Kunze, P. Grosse, M. Bernal Lopez, I. Sinev, I. Zegkinoglou, H. Mistry, J. Timoshenko, M. Y. Hu, J. Y. Zhao, E. E. Alp, S. W. Chee, B. Roldan Cuenya, *Angew. Chem., Int. Ed.* **2020**, *59*, 22667.

[223] R. C. Pang, P. F. Tian, H. L. Jiang, M. H. Zhu, X. Z. Su, Y. Wang, X. L. Yang, Y. H. Zhu, L. Song, C. Z. Li, *Nat. Sci. Rev.* **2020**, https://doi.org/10.1093/nsr/nwaa187.

[224] Y. Zhao, X. Tan, W. F. Yang, C. Jia, X. J. Chen, W. H. Ren, S. C. Smith, C. Zhao, *Angew. Chem., Int. Ed.* **2020**, *59*, 21493.

[225] S. B. Scott, T. V. Hogg, A. T. Landers, T. Maagaard, E. Bertheussen, J. C. Lin, R. C. Davis, J. W. Beeman, D. Higgins, W. S. Drisdell, C. Hahn, A. Mehta, B. Seger, T. F. Jaramillo, I. Chorkendorff, *ACS Energy Lett.* **2019**, *4*, 803.

[226] Z. H. Yan, H. M. Sun, X. Chen, H. H. Liu, Y. R. Zhao, H. X. Li, W. Xie, F. Y. Cheng, J. Chen, *Nat. Commun.* **2018**, *9*, 2373.

[227] J. Jiang, F. F. Sun, S. Zhou, W. Hu, H. Zhang, J. C. Dong, Z. Jiang, J. J. Zhao, J. F. Li, W. S. Yan, M. Wang, *Nat. Commun.* **2018**, *9*, 2885.

[228] J. W. Huang, Y. Y. Li, Y. D. Zhang, G. F. Rao, C. Y. Wu, Y. Hu, X. F. Wang, R. F. Lu, Y. R. Li, J. Xiong, *Angew. Chem., Int. Ed.* **2019**, *58*, 17458.

[229] B. H. Zhao, M. Y. Sun, F. P. Chen, Y. M. Shi, Y. F. Yu, X. G. Li, B. Zhang, *Angew. Chem., Int. Ed.* **2020**, https://doi.org/10.1002/anie.202015017.

[230] M. Kim, B. Lee, H. Ju, S. W. Lee, J. Kim, *Adv. Mater.* **2019**, *31*, 1901977.

[231] J. C. Meier, C. Galeano, I. Katsounaros, A. A. Topalov, A. Kostka, F. Schüth, K. J. J. Mayrhofer, *ACS Catal.* **2012**, *2*, 832.

[232] J. Polčák, J. Čechal, P. Bábor, M. Urbánek, S. Průša, T. Šikola, *Surf. Interface Anal.* **2010**, *42*, 649.

[233] T. Li, O. Kasian, S. Cherevko, S. Zhang, S. Geiger, C. Scheu, P. Felfer, D. Raabe, B. Gault, K. J. J. Mayrhofer, *Nat. Catal.* **2018**, *1*, 300.

[234] J. W. Hou, C. W. Ashling, S. M. Collins, A. Krajnc, C. Zhou, L. Longley, D. N. Johnstone, P. A. Chater, S. C. Li, M. V. Coulet, P. L. Llewellyn, F. -X. Coudert, D. A. Keen, P. A. Midgley, G. Mali, V. Chen, T. D. Bennett, *Nat. Commun.* **2019**, *10*, 2580.

[235] C. Lee, K. Shin, C. Jung, P. -P. Choi, G. Henkelman, H. M. Lee, *ACS Catal.* **2019**, *10*, 562.

[236] K. A. Owusu, L. B. Qu, J. T. Li, Z. Y. Wang, K. N. Zhao, C. Yang, K. M. Hercule, C. Lin, C. W. Shi, Q. L. Wei, L. Zhou, L. Q. Mai, *Nat. Commun.* **2017**, *8*, 14264.

[237] X. L. Li, M. Li, Q. Yang, H. F. Li, H. L. Xu, Z. F. Chai, K. Chen, Z. X. Liu, Z. J. Tang, L. T. Ma, Z. D. Huang, B. B. Dong, X. W. Yin, Q. Huang, C. Y. Zhi, *ACS Nano* **2020**, *14*, 541.

Liqiang Mai is chair professor of materials science and engineering at Wuhan University of Technology (WUT). He received his Ph.D. degree from WUT in 2004. He carried out his postdoctoral research at Georgia Institute of Technology in 2006–2007. He worked as advanced research scholar at Harvard University in 2008–2011 and University of California, Berkeley in 2017. He is Fellow of the Royal Society of Chemistry and his current research interests focus on new nanomaterials for electrochemical energy storage and micro/nano energy devices.

Xiong Liu obtained his Bachelor's degree from Wuhan University of Technology in 2016. He is now a Ph.D. candidate with Prof. Dongyuan Zhao and Prof. Liqiang Mai. His research interests focus on the controllable structure design for energy storage/conversion and reconstruction chemistry in electrocatalysis.